POLITECNICO DI MILANO

School of Industrial and Information Engineering

Department of Chemistry, Materials and Chemical Engineering

"G. Natta"

Master degree in Materials Engineering and Nanotechnology

SYNTHESIS OF INDIUM PHOSPHIDE FOR THIN FILM SOLAR CELLS

Supervisor: **Ing. Luca MAGAGNIN**

Assistant Supervisor: **Prof. Roya MABOUDIAN**

Andrea Vittorio ORIANI

Matr. 765661

Academic Year 2011-2012

Acknowledgements

I wish to thank, first and foremost, my supervisor Ing. Luca Magagnin for the precious time and the priceless advices he was able to give me in every situation, despite the hundreds of tasks filling up his days.

I'm grateful to Prof. Roya Maboudian and Dr. Carlo Carraro for hosting me and give me the opportunity of working in one of the most prestigious universities in the World; walking on the floor where plutonium was discovered is not something usual.

I'd like to express my gratitude to Anahit and Peter with whom I shared all the efforts, all the disappointment and, fortunately, also the satisfaction coming from this project.

A thank is due to all the guys in the *Maboudian lab* for the convivial moments spent together, particular gratitude goes to Albert for his patient and constant help and to John for caring about my safety in the lab.

Going back to *Polimi* I'd like to acknowledge the valuable contribution of Simona in the effort of complexing the egocentric indium. Gratitude is due also to Dario, Mattia and Fabio for the technical help and sample characterization.

I'd like to thank all the professors that in the last five years gave me the bases to become, hopefully, a good engineer.

Last but not least the most heartfelt thanks goes to my family and friends, for their presence and for their influence that contributed and still contributes to form my person; finally I thank my grandaunt that taught me something I couldn't learn neither in Politecnico nor in Berkeley: Milanese dialect.

Index

Index of Figures

Abstract

Research was articulated in several branches; initially direct indium phosphide deposition in aqueous solutions was investigated, this was performed on different substrates starting from inorganic indium and phosphorus precursors. InP could not be obtained with this process but oxidized forms of phosphorus were deposited together with indium.

Consequently indium and red phosphorous composite deposition was studied due to negative results from direct deposition. This was performed on Molybdenum substrates, starting from a suspension of red phosphorus in aqueous baths containing In^{3+}. Just partial reaction of In with P_{red} was possible after annealing, leading to compositional inhomogeneity in the deposit.

Pure indium deposition followed by phosphorous incorporation was then considered, studies were performed both on the pure indium plating step and on the following incorporation technique. Two different processes were used and studied: phosphorization of the In layer in phosphine gas and dropcasting of red phosphorous on indium followed by thermal treatment. Phosphorization led to good quality InP as confirmed from compositional analysis and optical characterization (PL and TRPL): photoluminescence peak was found to be at the theoretical value for InP, 920nm, and exciton lifetime resulted to be 2,3ns from time resolved photoluminescence. The dropcasting process is promising but still needs some improvements since partial conversion of In to InP was obtained.

For the solutions used during deposition, cyclic voltammetry was performed in parallel with plating, in order to characterize precursors and determine the effect of additions to the solution.

The script is organized into different parts: in the first part (chapter 1) is reported an overview on solar photovoltaic, electrodeposition and the state of the art about InP. In the second part (chapter 2) experimental procedure is defined and results are reported (chapter 3), finally discussion of experimental results is performed (chapter 4).

Sommario

La ricerca è stata articolata in diversi settori, inizialmente è stata studiata la deposizione diretta di indio fosfuro in soluzione acquosa, questa è stata effettuata su diversi substrati a partire da precursori inorganici di indio e fosforo. Diversi tipi di soluzione sono stati utilizzati, ispirati vuoi ai processi di deposizione di Ni-P, vuoi ad articoli presenti in letteratura riguardanti l'elettrodeposizione di InP. Sali inorganici sono stati utilizzati come precursori dell'indio (indio cloruro e indio solfato) e svariati precursori del fosforo sono stati considerati, tra i quali acido fosforoso e fosforico, sodio ipofosfito e ammonio esafluorofosfato. L'aggiunta di complessanti per l'indio e di alcol è stata investigata.

Non e stato possibile ottenere fosfuro di indio con questo processo, ma forme ossidate di fosforo sono state depositate insieme all'indio.

Conseguentemente la deposizione del composito composto da indio e fosforo rosso è stata studiata, a causa dei risultati negativi della deposizione diretta. Questa è stata effettuata su substrati di molibdeno, a partire da una sospensione di fosforo rosso in bagni acquosi contenenti In^{3+}. Solo una parziale reazione dell'In con in fosforo è stata possibile dopo ricottura, questo ha portato a disomogeneità composizionali nel deposito che hanno reso questo processo non accettabile. Passaggio fondamentale prima di effettuare qualsiasi processo a temperatura superiore ai 156°C, punto di fusione dell'In, è la deposizione di un *capping layer,* che impedisca il flusso dell'indio fuso sulla superficie del substrato.

La deposizione di indio puro seguita da incorporazione di fosforo è stata quindi considerata, sono stati condotti studi sia sul processo di placcatura dell'indio puro, che sulle successive tecniche di incorporazione. Due processi diversi sono stati usati e studiati: fosforizzazione dello strato di indio con gas fosfina e *dropcasting* di fosforo rosso sull'indio, seguito da trattamento termico. La fosforizzazione ha portato a InP di buona qualità come confermato da analisi composizionale e caratterizzazione ottica (PL e TRPL): il picco di fotoluminescenza è risultato al valore teorico per l'InP, ossia 920nm, e la vita dell'eccitone è risultata essere di 2,3ns da TRPL. Il processo di *dropcasting* è promettente, ma necessita ancora di alcuni miglioramenti in quanto soltanto conversione parziale di In a InP è stata ottenuta. Diverse architetture sono state studiate per il *dropcasting*, derivanti dai risultati ottenuti durante la sperimentazione. In particolare si sono gradualmente aggiunti *capping layers* in modo da aumentare in confinamento dell'indio, in questo modo si è

ridotta l'interazione tra In e P durante ricottura. Per questo motivo ulteriori studi sono necessari.

Per le soluzioni usate durante la deposizione, è stata eseguita voltammetria ciclica in parallelo con la placcatura, al fine di caratterizzare precursori e determinare l'effetto di aggiunte alla soluzione.

Lo scritto è organizzato in diverse parti: nella prima parte (capitolo 1) è riportata una panoramica sul solare fotovoltaico, sull'elettrodeposizione e sullo stato dell'arte circa il fosfuro di indio. Nella seconda parte (capitolo 2) viene definita la procedura sperimentale e sono riportati i risultati (capitolo 3), infine viene affrontata la discussione dei risultati sperimentali (capitolo 4).

Introduction

In these years and even more in the close future energy production will be considered one of the most important scientific and technological challenges. Problems are both related to production itself and to the potentially negative effects that an increase in energy consumption can have on environment, mainly in terms of pollution. For this reason, to face the growing energy demand due to emerging countries like India and China, it's necessary to partially replace fossil fuels with new and less polluting sources of energy, possibly distributed more homogeneously on the Earth surface. In this prospect the main limit of renewables are higher costs and the intrinsic discontinuity of production with respect to traditional sources of energy.

Since an engineer, as a member of community, must be aware of the world around him, this thesis work is included in the growing set of research programs conducted with the aim of supplying a valid alternative to traditional, fossil fuel based, sources of energy. Solar photovoltaic is considered one of the possible alternatives and its market is growing from year to year, for this reason this research program is focused on the development of a new production process for InP as active layer in photovoltaic devices. This III-V semiconductor was used in the 90's by NASA for aerospace applications because of its high radiation resistance and its semiconducting properties that made it optimal for energy generation in space. This material was subsequently abandoned, and never considered for terrestrial applications because of its high production costs, the aim of this research is to propose a new production technology that allows a reduction in costs and therefore a return to the utilization of this semiconductor for the production of low cost photovoltaic cells.

Indium phosphide is a suitable material for thin film photovoltaic application because of its optical and semiconducting properties: it is a direct bandgap material, this implies an high light absorption and thus a thin layer of InP (about 1 micron) can absorb 95% of the light absorbed by the bulk material. For comparison are necessary more than 100 microns of Si to absorb the same fraction of light. Moreover it has a low surface recombination rate, if compared with the most popular III-V semiconductor GaAs, InP surface recombination velocity can be three orders of magnitude slower. Finally its bandgap is 1.35eV, this allows

light absorption in most of the solar spectrum i.e., for every photon with wavelength lower than 920nm.

III–V semiconductor solar cells have demonstrated the highest power conversion efficiencies to date. However, the cost of III-V solar cells has historically been too high to be practical outside of specialty applications. This stems from the cost of raw materials, need for a lattice-matched substrate for single-crystal growth, and complex epitaxial growth processes. Traditional production process is based on MOCVD, in the '90s InP was epitaxially grown in the form of monocrystal on expensive InP wafers, then heteroepitaxy was employed to reduce problems related to the InP substrate (e.g., high cost, fragility, high mass density and low thermal conductivity). Research on this semiconductor resumed in the last years and the most recent and cost effective production process is based on MOCVD on metallic substrates, this gives good quality polycrystalline InP. Even if this new procedure leads to a reduction in costs it's still based on a vapour phase process, this implies low raw material utilization, high temperature and controlled reaction chambers.

Indium is a rare metal and it's availability is reduced, it has been estimated that world reserves of indium are 2600 tonnes and it's consumption is growing from year to year. It is particularly used (more than 80%) in the form of ITO for LCD displays. Consequently, due to the increase of consumer goods using this technology, the amount of waste LCD panels is growing more and more. The positive aspect of this situation is the possibility of recovering In from dismissed LCD panels, several techniques and methods have been proposed allowing to recover up to 86% of the In contained in LCD panels [1][2][3][4].

In this thesis we are proposing to produce InP via electrochemical deposition, this technique presents advantages in terms of material utilization, deposition parameters (room pressure and low temperature) and versatility in the prospect of large scale production, for example it could possible to deposit on thin metal foil to obtain flexible solar cells.

Chapter 1

Solar photovoltaic and electrodeposition

Thanks to its properties and its availability, among renewables, solar seems to be one of the most promising alternatives. With solar energy we mean thermal or electric energy produced by directly exploiting the energy irradiated by sun on the Earth's crust. Solar is thus one of the renewable sources of energy that we are going to use in the future to satisfy the growing need for energy. Anyway at the moment solar is considered too expensive to be a real alternative to fossil fuels, even because it's not a 24 hour source of energy and depends on climate and seasonality. The aim of this research is indeed to propose a deposition process for InP that could reduce production costs to make a real alternative to fossil fuels out of solar photovoltaic.

In this chapter an overview is presented both on solar photovoltaic, to contextualize and give an idea of the final application of this research work, and on electrodeposition, to provide general information on the technique proposed to produce Indium Phosphide.

1.1 PHOTOVOLTAIC PRINCIPLES

1.1.1 Solar radiation

The spectrum of solar radiation is close to that of a black body with a temperature of about 5,800 K. The Sun emits across most of the electromagnetic spectrum. Although the Sun produces Gamma rays as a result of the nuclear fusion process, these high energy photons are converted to lower energy photons before they reach the Sun's surface and are emitted out into space.

As a result, the Sun doesn't give off any gamma rays. The Sun does, however, emit X-rays, ultraviolet, visible light, infrared and even radio waves.

The 99% of the solar spectrum has wavelength between 0.15μm and 4μm (*Fig.1*) and it can be broken down into three bands depending on the value of λ:

• Ultraviolet (0.01μm < λ ≤ 0.38μm) is a highly energetic radiation, but it covers a small percentage of the solar spectrum, is almost entirely intercepted by oxygen and ozone in the upper atmosphere .

• Visible (0.38μm < λ ≤ 0.7μm): radiation is visible to the human eye, representing all colors, from violet to red, and about 46% of total solar radiation.

• Infrared (0.7μm < λ ≤ 300μm): is a radiation in the form of heat, and it's an important part of the solar spectrum since it represents about 46% of the whole radiation.

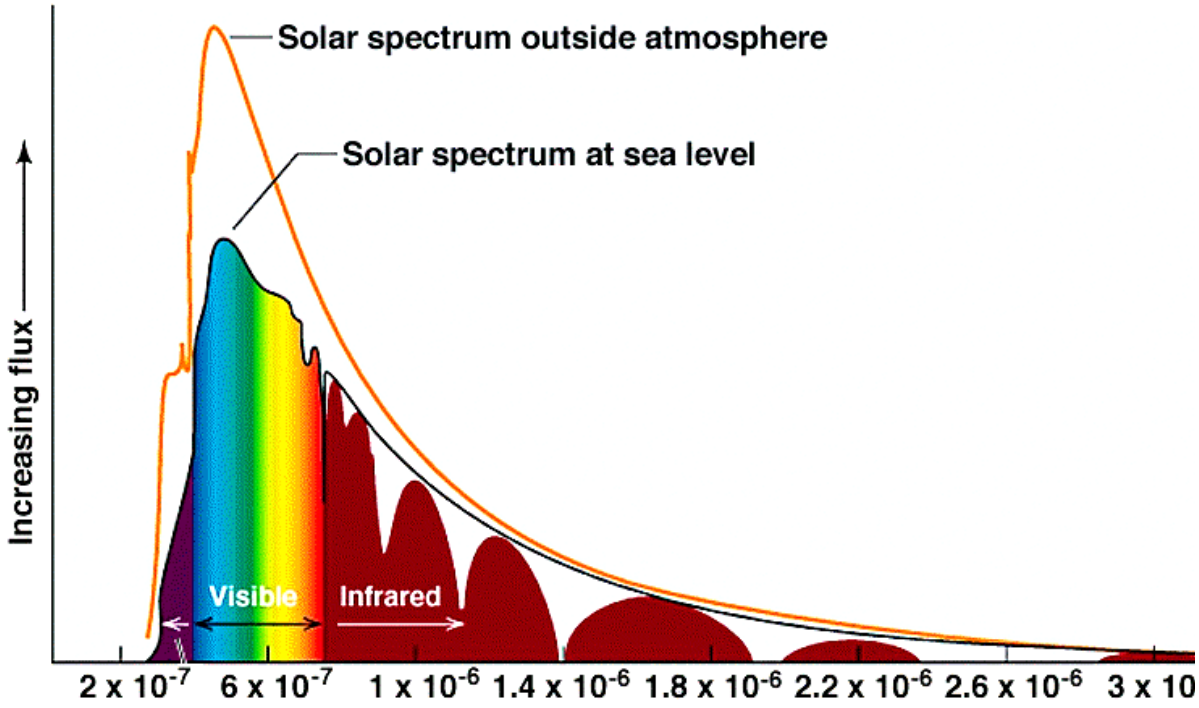

Figure 1: Solar spectrum

The intensity of solar radiation outside atmosphere is higher than that at the sea level and varies with the distance between Earth and Sun. Sunlight reaches the outer atmosphere with higher intensity during January/December and lower during June/July. This could look strange but actually seasonal variations are not determined by Earth-Sun distance, but rather by the misalignment between the earth's axis and the ecliptic (plane where lies the orbit of Earth around the Sun), i.e. the angle of incidence of sunlight on Earth.

The amount of incoming solar electromagnetic radiation per unit area that would be incident on a plane perpendicular to the rays, at a distance of one astronomical unit, AU

(roughly the mean distance from the Sun to the Earth), is called solar constant. The "solar constant" includes the whole solar radiation, not just visible light. Its average value was thought to be approximately 1.366kW/m², varying slightly with solar activity, but recent recalibrations of the relevant satellite observations indicate that a value closer to 1.361kW/m² is more realistic [5].

The solar radiation does not reach for the entire earth's surface, in part it's absorbed in the atmosphere by the elements that compose it, in part reflected into space and in part it's diffused into the atmosphere itself (scattering).

The phenomenon of scattering consists in the reflection and diffusion of photons composing the solar radiation, these processes are due to impact of the electromagnetic waves with molecules in air (Rayleigh scattering), or with water vapour and with the dust particles (Mie scattering).

The decrease of the effective incident radiation on the soil is strongly influenced by the amount of atmosphere crossed. To take account of these factors was defined the Air Mass One (AM1) as the thickness of standard atmosphere crossed in the direction perpendicular to the Earth's surface, the measure is related to sea level. It is defined instead Air Mass Zero (AM0) the extra-atmospheric condition. The maximum intensity of incident solar radiation at sea level under conditions of clear sky, perpendicular rays (noon), is always less than the value of the solar constant, and is roughly equivalent to 1000W/m^2; it's necessary to remember that this value is highly dependent on weather conditions.

The solar radiation that impacts the Earth can be divided into: direct, diffuse and reflected: the first reaches the ground with a defined angle of incidence, the second acts with multiple angles and the third is related to the reflection of sunrays in the surrounding environment.

World primary energy consumption for 2012 [6] was about 16.3TW, if we consider solar constant and total terrestrial section ($1.29 \cdot 10^{14} m^2$) sun supplies about 176,000 TW, about 30% of that is reflected to sidereal space thus 120,000TW are available to provide the 16.3TW required to sustain human activity. Sun is therefore able to supply enough energy, provided that conversion of solar energy to electricity is technologically and economically compatible with the socio-economical development of our planet. One of the most important factor in this case is transformation efficiency, i.e., the fraction of incident radiation converted into electricity [7]. This value determines the surface to be devoted to solar plants. The actual average solar radiation, taking into account latitude and daylight

trough the year, is 200W/m^2 therefore are necessary $\frac{5\cdot10^{-3}}{\eta}$ m^2/W where η is conversions efficiency. Considering a 10% efficiency to supply the world energy demand is necessary a surface of solar panels equivalent to a square with side of 900Km (about 0.2% of Earth surface) this value can half if we consider a 20% efficiency. It looks clear that solar energy utilization is not limited by surface availability, but rather by the presence of technologies able to convert irradiation in electricity with costs similar to current energetic sources. This is the reason why more and more research programs are conducted to increase conversion efficiency and reduce production costs.

1.1.2 Cell working principles and parameters

It is first of all important to have a clear idea of the basic principles allowing electricity generation from solar radiation, i.e. the photovoltaic effect, and it's also essential to define the main parameters and characteristics of solar cells.

1.1.2.1 The photovoltaic effect

The photovoltaic effect is the direct conversion of incident light into electricity by a p-n semiconductor junction device. Although the phenomenon was known for almost a century, the landmark achievement generally accepted to have heralded the modern era of PV power generation was the production in 1954 of a 6% efficiency, crystalline silicon solar cell by Chapin et al. [8]. It was rapidly realised that such solar cells were a convenient way of generating power in remote locations.

The p-n junction

A p-n junction is made from a single crystal modified into two separate regions, in this case we speak about homojunction [9]. We talk about heterojunction when *n* side consist of one semiconductor and *p* side of a different semiconductor. In a homojunction acceptor impurity atoms are incorporated into one part to produce the *p* region in which the majority carriers are holes. Donor impurity atoms in the other part produce the *n* region in which the majority carriers are electrons. The interface region may be less than 1μm thick. Away from the junction region on the *p* side there are (-) ionized acceptor impurity atoms and equal concentration of free holes. On the *n* side there are (+) ionized donor atoms and an equal concentration of free electrons, *Fig.2*.

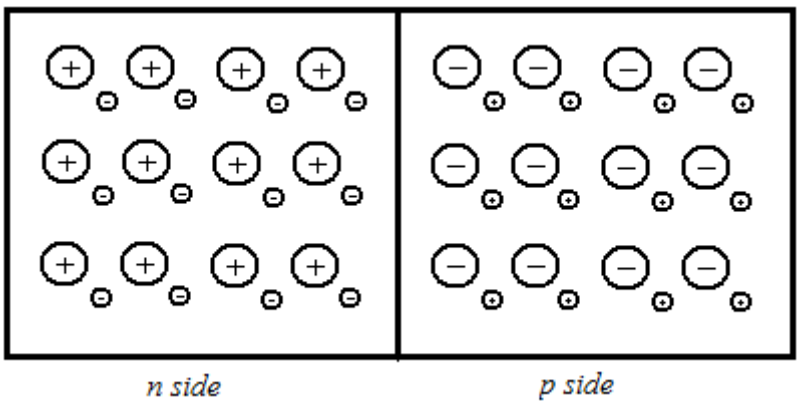

Figure 2: p-n junction

Holes concentrated on the p side would like to diffuse to fill the crystal uniformity. Electrons would like to diffuse from the n side. But diffusion will upset the local electrical neutrality of the system.

A small charge transfer by diffusion leaves behind on the *p* side an excess of (-) ionized acceptors and on the *n* side an excess of (+) ionized donors. This charge double layer creates an electric field (called built in electric field) directed from n to p that inhibits diffusion and thereby maintains the separation of the two carrier types. Because of this double layer the electrostatic potential in the crystal takes a jump in passing through the region of the junction, *Fig.3*.

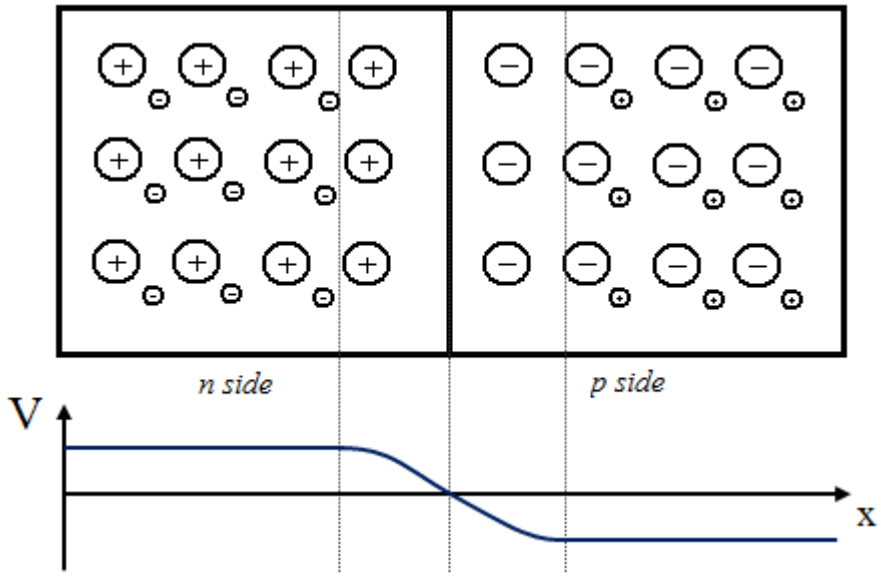

Figure 3: Depletion region and electrostatic potential

In thermal equilibrium the chemical potential of each carrier type is everywhere constant in the crystal, even across the junction. For holes:

$$K_B T \ln p(r) + e\varphi(r) = constant$$

Where p is the hole concentration and φ the electrostatic potential. Thus p is low where φ is high. For electrons:

$$K_B T \ln n(r) - e\varphi(r) = constant$$

And n will be low where φ is low.

The total chemical potential is constant across the crystal. The effect of the concentration gradient exactly cancels the electrostatic potential, and the net particle flow of each carrier type is zero. However, even in thermal equilibrium there is a small flow of electrons form n to p where the electrons end their lives by recombination with holes. The recombination current J_{nr} is balanced by a current J_{ng} of electrons which are generated thermally in the p region and which are pushed by the built-in field to the n region. Thus in zero external applied electric field:

$$J_{nr}(0) + J_{ng}(0) = 0$$

for otherwise electron would accumulate indefinitely on one side of the barrier.

If we consider the band structure in a generic semiconductor, [10] we can point out the presence of two electronic bands involved in the conduction process. There are the valence band that is almost filled with electrons and the almost empty conduction band, which are divided by the bandgap, (for silicon it is 1.2eV). The Fermi energy for the intrinsic, undoped, material is about in the centre of the gap, or forbidden region, between these bands. For p material it lies within the gap, but below the centre; for n material, above the centre, *Fig.4*. At equilibrium the Fermi energy throughout the material must be the same.

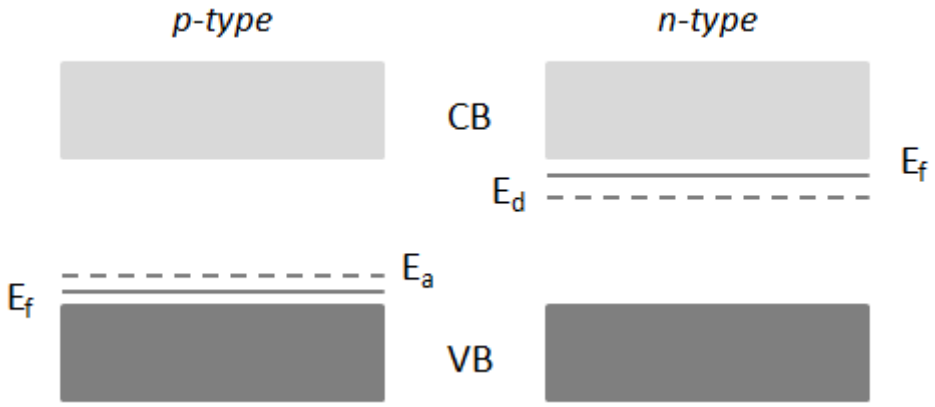

Figure 4: Band structure before charge diffusion

In order to fulfil this requirement in the junction region the aforesaid majority carrier migration occurs, leading to the formation of the double layer and the consequent built-in electric field. The height of this electrostatic barrier is equal to the difference between the

position of the gap in the *n* material and the *p* material, *Fig.5*. The Fermi energy and hence the barrier height vary with temperature and impurity concentration. A hole or unoccupied level in the valence band may diffuse for some distance in *n* material before it combines with an electron.

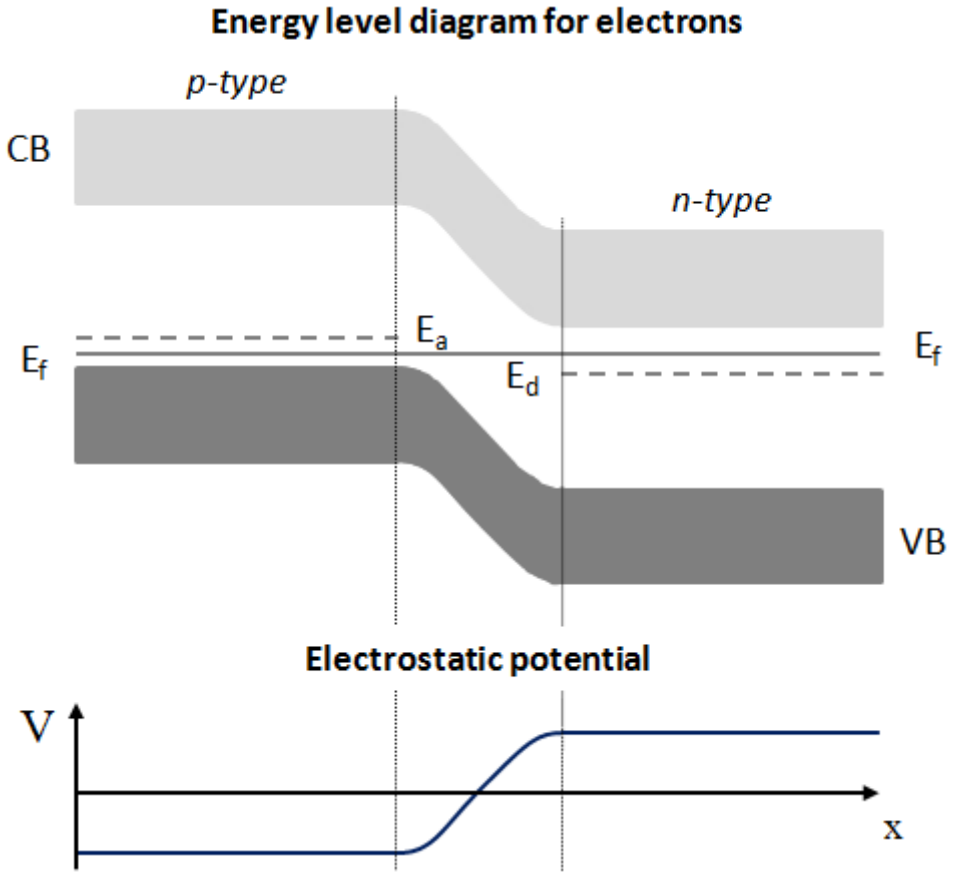

Figure 5: Electronic energy levels and electrostatic potential after charge diffusion

The average distance it travels before combining is called diffusion length for holes in *n* material. An analogous quantity is defined for electrons in *p* material. This is generally mentioned as *minority carrier diffusion length*.

Biasing and illumination of the p-n junction

A p-n junction can act as a rectifier [9]. A large current will flow if we apply a voltage across the junction in one direction, but if the voltage is in the opposite direction only a very small current will flow. If an alternating voltage is applied across the junction the current will flow chiefly in one direction (the junction has rectified the current). For back voltage bias a negative voltage is applied to the *p* region and a positive voltage to the *n* region, thereby increasing the potential difference between the two regions. In this

situation the depletion region is increased with respect to the equilibrium condition. Now practically no electrons can climb the potential energy hill from the low side of the barrier to the high side, *Fig.6*.

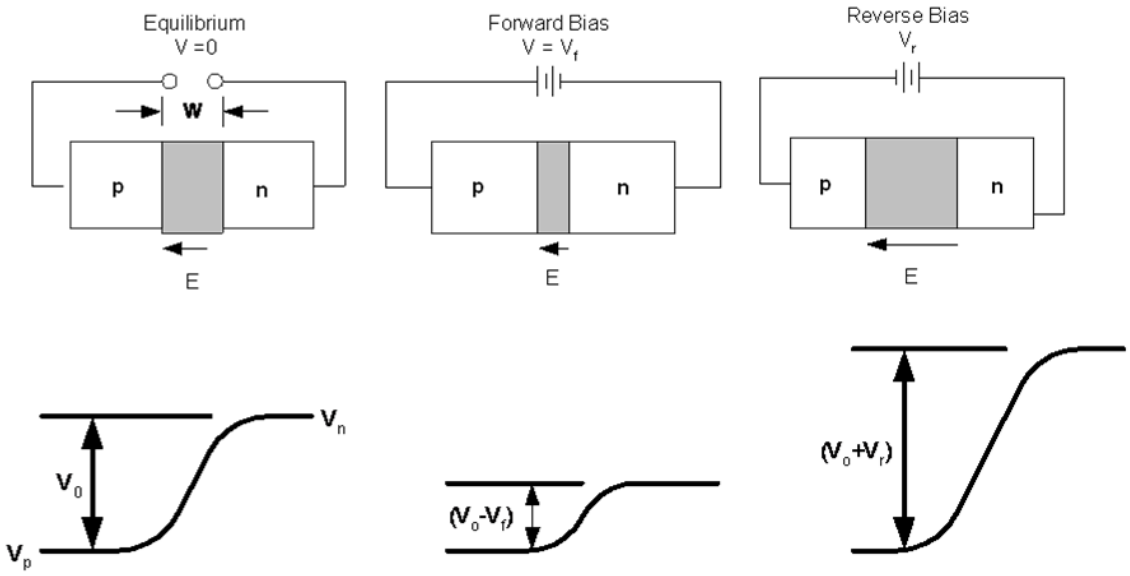

Figure 6: Effect of an external potential difference across the junction

When a forward bias is applied the depletion region is reduced with respect to the equilibrium condition, the recombination current increases because the potential energy barrier is lowered, thereby enabling more electron to flow from *n* to *p* side. The hole current flowing through the junction behaves similarly. The applied voltage lowers the barrier both for holes and electrons, so that large numbers of electrons flow from the *n* region to the *p* region under the same voltage conditions that produce large hole currents in the opposite direction.

If we shine light on a p-n junction each absorbed photon creates an electron and a hole. When these carriers diffuse to the junction, the built-in electric field of the junction separates them at the energy barrier. The separation of the carriers produces a forward voltage across the barrier: forward because the electric field of the photoexcited carriers is opposite to the built-in field in the junction, *Fig.7*.

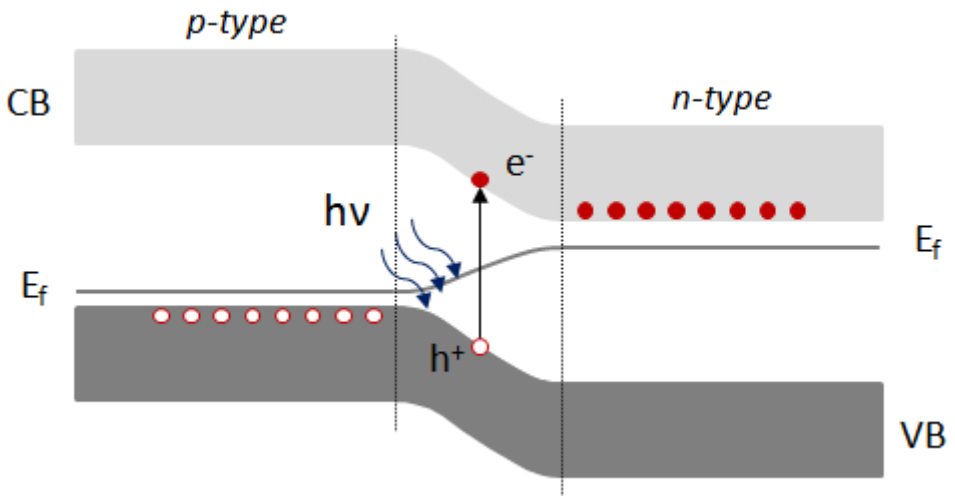

Figure 7: Illumination of the junction

The appearance of a forward voltage across the illuminated junction is called the photovoltaic effect. An illuminated junction can deliver power to an external circuit.

1.1.2.2 Solar cell overview and parameters

A solar cell is a semiconductor device that converts photons from the sun into electricity [11]. *Fig.8* shows the generic structure and operation of a single-junction inorganic solar cell. At the heart of the cell is the light-absorbing semiconductor material which converts photons into carriers (electrons and holes) via the photovoltaic effect.

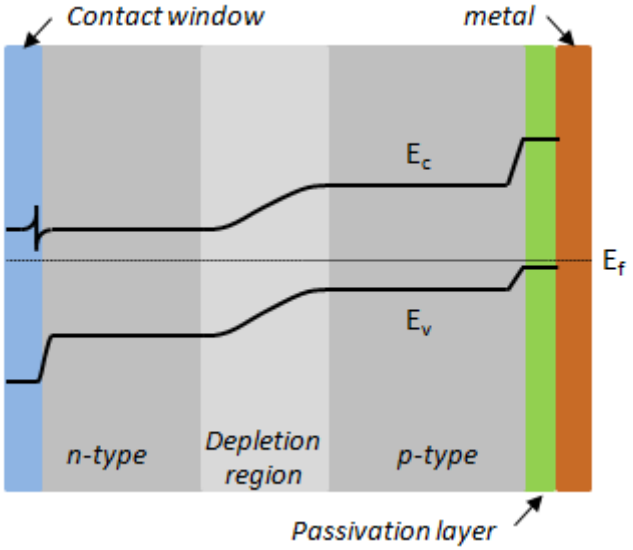

Figure 8: Generic solar cell structure and electronic levels

The different PV cells are normally identified by the composition and properties of the absorbing material. After generation, electrons and holes separate and are collected at the contacts. There are two main modes for charge carrier separation: drift of carriers, driven by the built-in electrostatic field of a p–n junction, and diffusion of carriers from zones of high to low carrier concentration following an electrochemical potential gradient. When drift is important, the structure of the cell can be used to compensate for poor diffusion. When diffusion is used, then improvement in material quality becomes more of the focus. Drift is typical of thin-film inorganic cells which are normally p–n junction devices with relatively high defect densities, while diffusion is more important for high-efficiency single crystal cells and is the driving transport mechanism for dye or organic solar cells. The properties of contacts and window layers are also critical to device performance. At least one contact needs to be both electrically conducting and transparent to photons in the spectral range where the absorber creates carriers. Transparent conductive oxides are the material of choice for this purpose. It is also important to point out that the simple structure and the division into well-defined layers with specific functions shown in *Fig.8* is not adequate to describe many solar cells.
In a number of designs light enters through the substrate, and contacts can be quite complicated, fabricated from several layers and with significant interdiffusion at metallurgical junctions.

In *Fig.9* it's possible to see the typical current-voltage characteristic for a solar cell in dark conditions and under illumination. Power is generated when the cell operates in the fourth quadrant, i.e. when voltage is positive and current is negative.

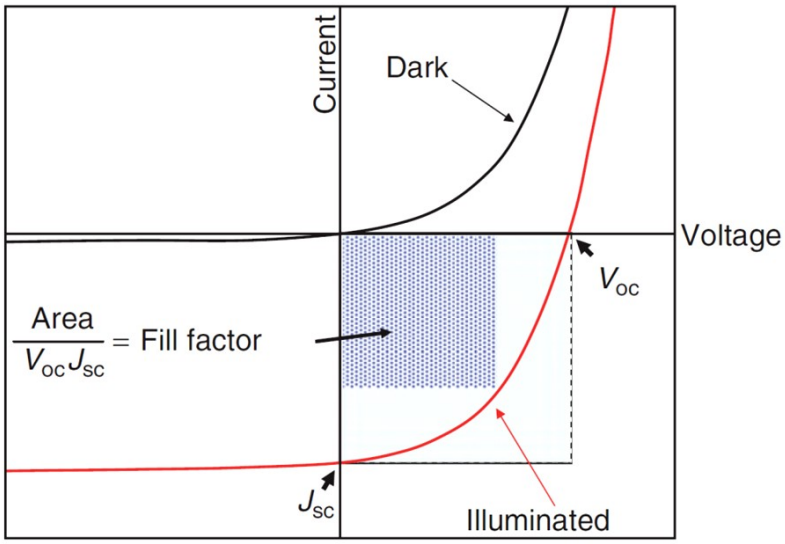

Figure 9: Current-voltage characteristic of a solar cell

By looking at the graph we can perform some considerations. The *I-V* curve under illumination has the same behaviour of a diode (dark conditions) shifted by a certain amount on the *I* axis. For sake of simplicity the curve can be flipped and represented as in *Fig.10* where we can identify three different regimes:

- AB: behaviour similar to an ideal current generator
- CD: behaviour similar to an ideal tension generator
- BC: it's the knee of the curve and the typical working range for the PV generator

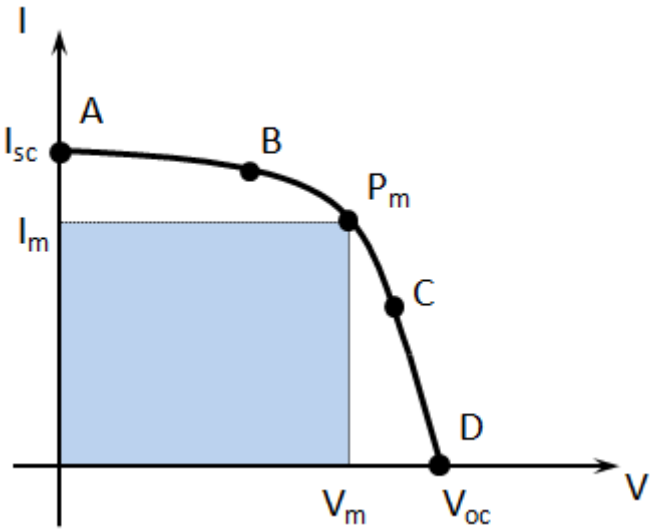

Figure 10: Fourth quadrant of cell characteristic

Analyzing the curve is then possible to determine two important points: the intersection between the curve and the ordinate I_{sc}, representing the short circuit current, i.e. the highest current the generator can supply, and the intersection between the curve and the abscissa V_{oc}, representing the open circuit voltage, i.e. the highest voltage the generator can supply.
If we define g_{opt} as the number of hole-electrons pairs generated by solar radiation per second and unit volume we can write [12]:

$$I_{sc} = g_{opt} eA\left[W + L_n + L_p\right]$$

where $A[W+L_n+L_p]$ is the generation volume (A is the cross-sectional area, W is the depletion region width and L_n and L_p are the minority carrier diffusion lengths in the n and p side, respectively). Bigger the value of I_{sc}, smaller the bandgap of the semiconductor used to absorb light, because a larger portion of the solar spectrum will be absorbed. The generation volume increases with a decrease of doping on each side of the device because W, L_n and L_p all increase with a decrease in doping concentration.
For an ideal solar cell:

$$V_{oc} = [kT/e] \ln[I_{sc}/I_o]$$

Were I_o is the reverse saturation current for an ideal solar cell and:

$$I_o \propto exp\left[-E_g/kT\right]$$

It follows that V_{oc} increases as the bandgap of the semiconductor used to absorb radiation increases.
We can also define the fill factor FF as the ratio between the maximum power generated by the cell and $I_{sc}V_{oc}$, we can think of it as the measure of how rectangular the I-V characteristic is in the fourth quadrant. The fill-factor FF and I_{sc} are found to reduce rapidly with a modest increase in the series resistance of the solar cell. In fact a series resistance of only 5 Ω will reduce the device efficiency to less than 30% of what it would have been for zero series resistance [12]. The series resistance mainly arises from the bulk resistances in the n and *p-type* sides of the device and from the resistances of the contacts to the doped regions. Increasing the doping concentration reduces the bulk resistance of a semiconductor; it also lowers the specific contact resistance of the metal contact to the semiconductor by increasing the probability of quantum mechanical tunnelling through the metal-semiconductor junction.
The solar conversion efficiency η, that represent the fraction of solar radiation converted to electric power, is given by:

$$\eta = \frac{I_{sc} \cdot V_{oc}}{P}$$

For comparison purposes the cell is usually illuminated with a simulated air mass (AM) spectrum, AM0 for space applications and AM1.5 for terrestrial applications. The AM0 spectrum is that incident from the sun just outside the Earth's atmosphere. The AM1.5 spectrum is the global average incident at the surface of the Earth. The power of incident radiation P is 1367 W/m^2 for the AM0 spectrum and 963 W/m^2 for the AM1.5 spectrum.

Two decades ago, Shockley and Queisser (S-Q) estimated the thermodynamic efficiency limit for solar cells with a single absorbing layer, i.e. single junction solar cell [11]. Their approach balanced the radiative transfer between the Sun, modelled as a black body at 6000K, and the solar cell assumed to be a 300K black body which absorbs photons with energy above an energy threshold (the bandgap). They varied the bandgap of the absorber and the solid angle from which the solar cell can collect the Sun's radiation (concentration). As the bandgap of the absorber increases, the open circuit voltage increases, but, because only photons with energy above the bandgap are converted into carriers, short circuit current decreases. This leads to a maximum efficiency as a function of bandgap. For unconcentrated solar irradiance AM1.5, a maximum efficiency limit of 31% at a gap near 1.3eV was found. For full solar concentration, AM0, maximum efficiency was 41% for 1.1eV material [13]. One limiting factor for higher efficiencies is that the excess kinetic energy of hot photogenerated carriers coming from de absorption of supra-bandgap photons is lost as heat through phonon emission, the other limiting factor is that photons with energy lower than bandgap are not absorbed. Considering these losses new theoretical efficiencies as a function of bandgap were calculated [14], *Fig.11*.

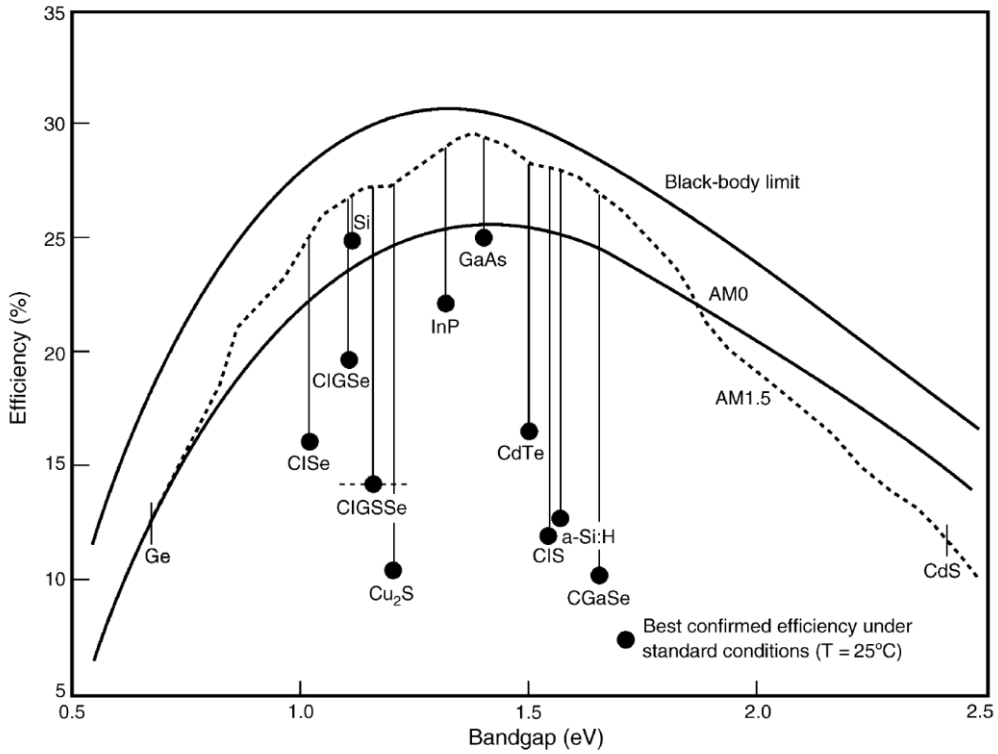

Figure 11: Conversion efficiency limit as a function of bandgap

Note that the maximum conversion efficiency for the AM1.5 spectrum is higher than that for AM0, while the AM0 spectrum has a higher overall power density. This is caused by the fact that the AM1.5 spectrum has a lower power density in parts of the spectrum that are not contributing to the energy conversion process.

1.1.4 Cell materials, properties and technologies

As mentioned before the optimal bandgap for terrestrial power generation is around 1.3eV, for this reason most of the semiconductors used for solar cells have a bandgap in the 1-1.7eV range [12]. The optimal compound semiconductors, under this aspect, are cadmium telluride (CdTe), indium phosphide (InP), gallium arsenide (GaAs), and copper indium disulphide ($CuInS_2$). Also monocrystalline and multicrystalline silicon (Si, E_g=1.12eV), copper indium diselenide ($CuInSe_2$, E_g=1.05eV), and amorphous silicon (aSi:H, E_g=1.7eV) are used even if the bandgap is slightly further away from the optimal value. The silicon based devices are usually homojunctions, i.e. junctions within the same material, whereas many of the compound semiconductor devices are heterojunctions, i.e. junctions between different materials. These usually use an n-type wide bandgap buffer layer, e.g. CdS to form a junction with the p-type absorber layer. This structure is usually preferred because the minority diffusion length of electrons in a p-type semiconductor is much greater than

that of holes in an n-type semiconductor. Here is given a overview of some typical solar cells, classified depending on the nature of the absorbing layer.

1.1.4.1 Silicon

Monocrystalline silicon

Silicon has an indirect energy bandgap of approximately 1.1eV at room temperature. The indirect energy bandgap causes a low optical absorption coefficient, ($\alpha \approx 100cm^{-1}$) and this means that the silicon needs to be at least one hundred micron thick ($>1/\alpha$) to absorb most of the incident light. The electron-hole pairs generated by light should be able to diffuse up to that distance and reach the electric field in the depletion region of the junction to contribute to the photocurrent. Increasing *W* to more than a few microns by lowering the doping concentrations causes an increase in the device series resistance to the point where it severely degrades device efficiency. The ability of the carriers to diffuse to the junction region is measured by the minority carrier diffusion length, *L*. Elementary semiconductor theory shows that:

$$L \propto \sqrt{\mu\tau}$$

where μ is the mobility and τ is the lifetime of minority carriers in the light absorbing region [12]. As both τ and μ are very sensitive to material purity and crystallinity, efficient devices can only be produced if the feedstock is pure enough and the densities of crystal defects minimised. The ‘‘solar grade silicon’’ purity parameters are less stringent than that needed for the microelectronic industry and in fact most PV cells manufactured to date used silicon supplied by the larger microelectronics industry. The rapid expansion of PV sales over the last years is pushing manufactures to purify silicon themselves for PV cells. A cross-sectional view of the conventional silicon solar cell structure that has dominated production in the recent years is given in *Fig.12*. The boron doped *p-type* monocrystalline silicon wafer is sawn from a single crystal ingot grown using the Czochralski method and the *p-n* junction is formed by diffusing phosphorus into the wafer.

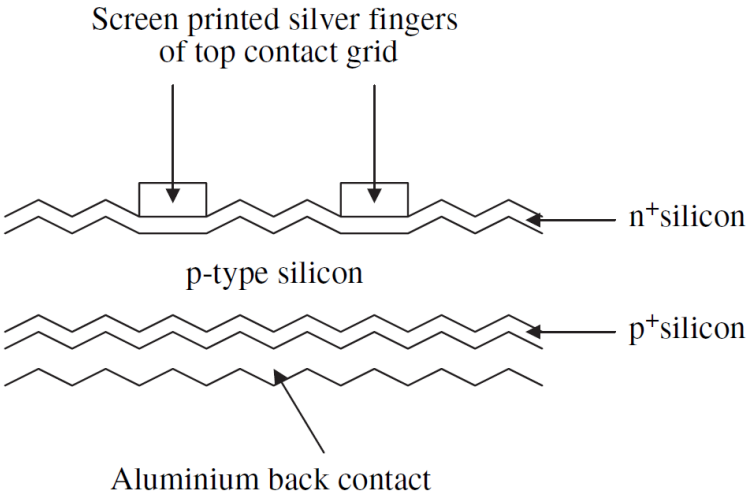

Figure 12: Traditional silicon cell structure

Screen printed silver contact fingers are used on the n-type surface to make both electrical contact and to allow light to be transmitted to the junction region. Aluminium paste is used to make contact at the back *p-type* surface. This is annealed to introduce a p+ doped region at the back of the cell, to lower the contact resistance and to supply a back surface field that reflects minority carriers back towards the junction. The cell surface is textured to minimise reflection and to refract light to high angles of refraction and enhance the path length of light within the silicon. An antireflection coating (usually titanium dioxide) is deposited over the top contact fingers to complete the device.

Green and co-workers from the University of New South Wales (UNSW) noticed that there are high disadvantages in using screen printed contacts [12]. Device efficiency is reduced to about 14% because of high shading losses, high resistivity of the screen printed silver grids compared to pure silver (3 times higher), high contact resistance between the grid and silicon and poor aspect. For this reason solar cells were developed in which the contacts are defined either using photolithography or laser scribing. A typical ‘‘UNSW cell structure’’ is shown in *Fig.13*. In this design the silicon surface has been passivated and grooves for contacting cut using laser scribing. In this buried contact design the contact metals, nickel, copper and then silver, are deposited using electroless methods.

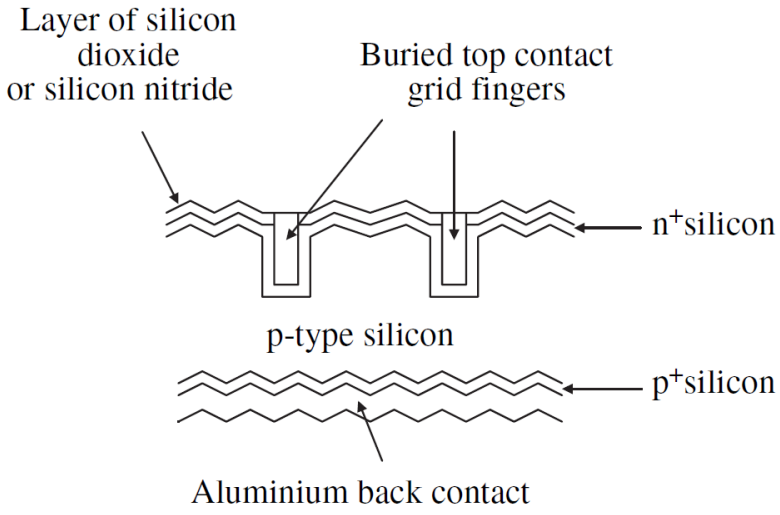

Figure 13: Schematic cross sectional view of a silicon cell with buried front contact

This design allows shallower phosphorus doping at the surface of the device without degrading the open circuit voltage, improving the short wavelength response of the cell. The contact resistance to the grid is also reduced thanks to the higher doping concentration of this n+ region. This type of cell is used in the high efficiency PV modules.

Silicon devices and modules still dominate production and sales. Although the market of silicon solar cells has continued to grow rapidly, the share of monocrystalline silicon products has actually reduced to approximately 38% this is due to increased competition from devices based on the use of multicrystalline silicon. The cells sold usually have efficiencies in the range 15-19%, the more sophisticated designs resulting in the higher efficiency devices.

Multicrystalline silicon

With this technique molten silicon is poured into a mold and then allowed to cool resulting in silicon ingots with large columnar grains (typically 0.3 mm diameter) growing from the bottom of the container upwards [12]. The grains extend through the wafers cut from the solidified block. The incorporation of hydrogen during device processing plays an important role in passivating the grain boundaries in the devices. This is most conveniently introduced by using PECVD (plasma enhanced chemical vapour deposition) to deposit silicon nitride as the top insulating layer, rather than silicon dioxide, as hydrogen is used in this process. Advantages of using multicrystalline growth over the Czochralski method include lower capital costs, higher throughput, less sensitivity to the quality of the silicon feedstock used and higher packing density of cells to make a module because of the square

or rectangular shape of the cells. The best modules made using multicrystalline silicon generally have efficiencies 2-3% lower than those of crystalline silicon and production costs are approximately 80% of that of crystalline silicon cells. The market share of this product is about 45%.

Amorphous silicon

Amorphous silicon thin films are produced using CVD (chemical vapour deposition) with gases containing silane (SiH_4), the most used techniques are PECVD or *hot wire* CVD [15]. The substrates suitable for deposition can be both rigid, e.g. glass, and flexible, e.g. thin metallic sheets and plastics, allowing for continuous production and diversity of use. The material that is used in solar cells is actually hydrogenated amorphous silicon, aSi:H, an alloy of silicon and hydrogen (5-20 %at hydrogen).The hydrogen plays the important role of passivating the dangling bonds resulting from the random arrangement of silicon atoms. The hydrogenated amorphous silicon is found to have a direct energy bandgap of 1.7eV and an optical absorption coefficient $\alpha > 10^5 cm^{-1}$, for photons with energy greater than E_g. This means that only a few microns of material are able to absorb most of the incident radiation, reducing material usage, weight and hence cost.

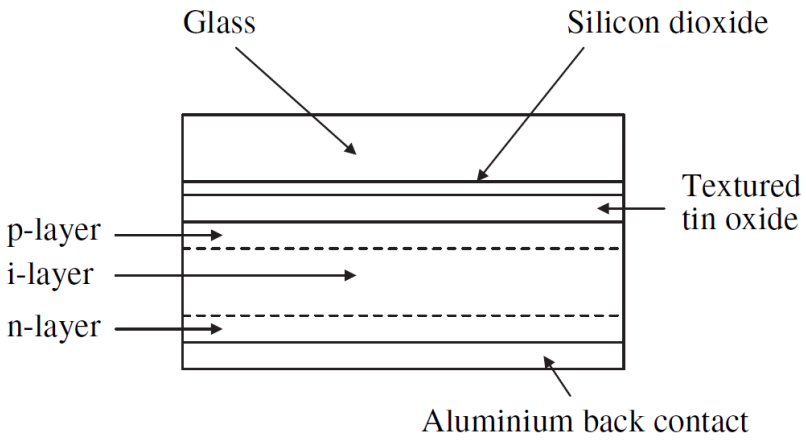

Figure 14: Schematic cross-sectional view of an amorphous silicon single junction solar cell.

Doping though severely degrade mobility and lifetime of minority carriers in this material. This problem can be reduced using a *p-i-n* structure where light absorption, electron-hole pairs generation and migration all occur within the undoped *i-layer*, assisted by the electric field across it. In *Fig.14* a cross-sectional view of a typical *p-i-n* cell structure is shown. The initial cell efficiency can be higher than 12% in laboratory testing, commercial modules when exposed to sunlight over a period of months degrade to an efficiency of

approximately 4-5%. This phenomenon is known as Staebler-Wronski effect [15]. It is, however, possible to increase efficiency and cell stability by using multiple *p-i-n* structures characterized by *i-layers* with different bandgap, to produce ‘‘double junction’’ or ‘‘triple junction’’ structures.

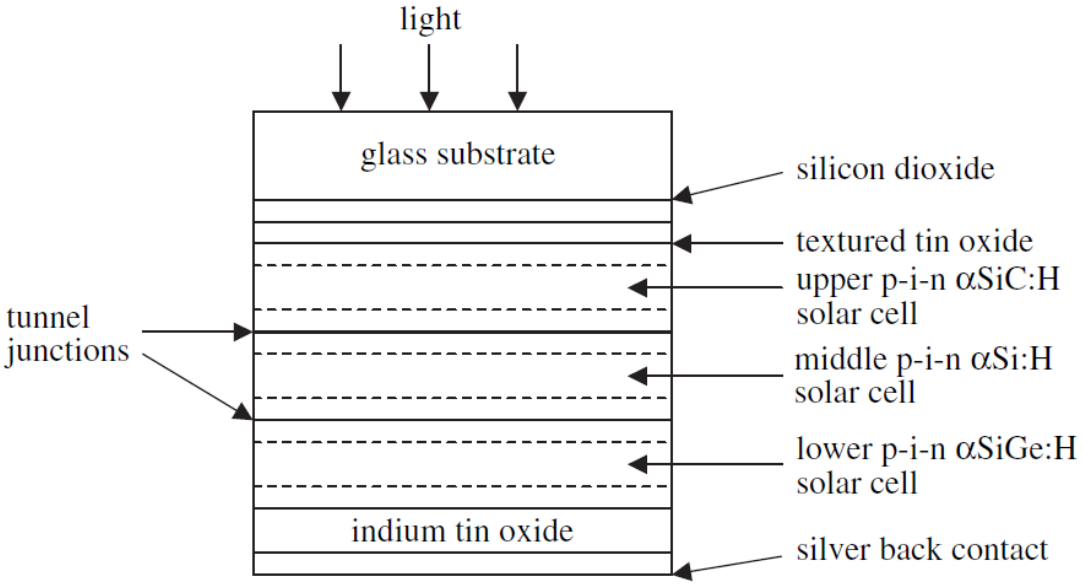

Figure 15: Schematic cross-sectional view of an amorphous silicon triple junction solar cell

Bandgap narrowing is obtained by alloying silicon with germanium and wider bandgap layers are produced by alloying silicon with carbon. *Fig.15* shows a cross-sectional schematic view of a triple junction cell. The highest reported stabilised efficiency is now higher than 9.5% for a double junction and higher than 10% for a triple junction [15].

HIT solar cell

An HIT cell is made up of an intrinsic amorphous-Si layer, a doped amorphous-Si layer and a TCO layer deposited on both sides of a crystalline Si substrate [16], this is shown in *Fig.16*. On both of the doped amorphous-Si layers grid electrodes are fabricated, therefore the cell has a symmetrical structure. Since it doesn’t have high hardness alloy metals as electrodes, it is characterized by a stress free structure that is well suited to thinner substrate solar cells.

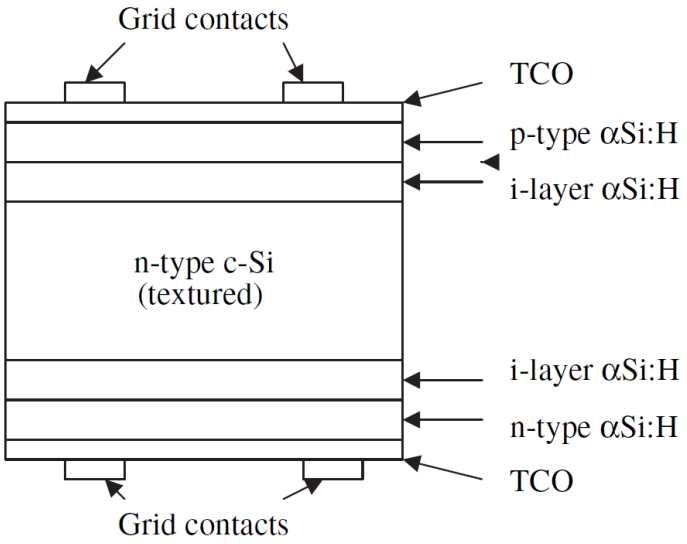

Figure 16: Schematic cross-sectional view of an HIT cell

The HIT uses high quality and very thin a-Si layers to form the hetero-junction and passivate the dangling bonds of the crystalline silicon substrate. Furthermore all of the process temperatures for this cell are below 200°C, that implies a reduction in production costs and preservation of the initial high level quality of the crystalline silicon substrate. In 2010 the conversion efficiency [16] of the standard HIT solar cell reached a level of 23% for a 100.4cm^2 crystalline silicon substrate.

1.1.4.2 III-V Semiconductors and multijunctions

III-V Compounds such as gallium arsenide (GaAs) and indium phosphide (InP) have direct energy bandgaps, high optical absorption coefficients and good values of minority carrier lifetimes and mobilities (in highly pure, single crystal material). All this peculiarities make them excellent materials for making high efficiency solar cells [12]. Single crystals of these materials can be produced using either the liquid encapsulated Czockralski method or using a Bridgmann method. The two III-V materials most widely used for single junction solar cells are GaAs and InP. Solar radiation with energy above that of the bandgap is absorbed efficiently within a few micrometers from the surface because of their high absorption coefficients. Both materials have very good bandgap values for single-junction conversion of the solar spectrum, that is 1.42eV for GaAs and 1.35 eV for InP. InP has a minority carrier diffusion length, L_n (for Zn doped p-InP wafers) in the range 2-30 μm depending on doping density.

The disadvantage of using III-V compounds in photovoltaic devices is related to the very high cost for the production of good quality substrates or epitaxial layers of these

compounds. Crystal imperfections, including unwanted impurities, severely reduce device efficiencies. The high density of the materials is also a disadvantage, in terms of weight, unless very thin cells can be produced to take advantage of their high absorption coefficients. These drawbacks led to them being considered as unpromising materials for single junction, terrestrial, solar cells. It was primarily due to their potential for space applications that development of III-V based devices was undertaken. The potential for high conversion efficiencies together with radiation resistance in the demanding environment of space power generation mitigated against the high materials cost.

The success of Si solar cells for generating electrical power in space led to a demand for higher performance devices and in the maintenance of performance during operation. An important factor that needed to be addressed was the degradation in performance due to radiation damage from high energy electrons and protons. Reducing degradation reduces the weight at launch. Radiation damage to the materials is most severe at the depth where the radiation stops giving up the energy to the crystal lattice, i.e. at the end of the range of the charged particle. The damage to the lattice is associated to the creation of recombination centres and loss of cell performance. Being an indirect bandgap semiconductor Si requires a greater volume to absorb the convertible solar radiation and this makes it more susceptible to radiation damage. Direct bandgap, high performance cells based on III-V materials can be made significantly thinner than Si based devices. Most of the protons and electrons pass through the thin active region thus causing minimal lattice damage. Testing of GaAs cells in space flights and in radiation trials confirmed the benefits of using these devices for space power generation. Weinberg et al. [17] concluded that n/p GaAs homojunction cells were superior both in radiation resistance and efficiency to conventional Si n/p devices. Also InP based devices gave high performances and shown a superior radiation resistance to GaAs. The best single junction GaAs and InP based devices were grown by epitaxial techniques using liquid phase epitaxy (LPE) and metalorganic chemical vapour deposition (MOCVD). These techniques gave the highest conversion efficiencies for these materials in terrestrial conditions (AM1.5), respectively 25.1% and 21.9%. Compared to diffusion based technology this is a high cost processing route but it enables close control over the growth parameters. The increase in device efficiency over that of non-epitaxial cells should be greater than the additional processing cost if the devices are to be produced economically. The additional cost of growing monolithic multijunctions compared to a single epitaxial junction is relatively small and the potential increase in device efficiency is much greater. Therefore, over the last 20 years

the major effort on III-V based devices has been on the multijunction system and the record single junction solar cell efficiencies have remained unchanged since the early 1990s.

GaAs solar cells

The traditional production route for GaAs solar cells (that gave the best results in terms of efficiency) was based, as aforementioned, on the homo-epitaxial growth of this material on a wafer. This implied high cost of production and also high weight for the final device. To reduce the production costs, the expensive GaAs substrate was substituted with a Si wafer [18]. This solution, based on MOCVD for the epitaxial growth of GaAs, gave good results in terms of efficiency, 16.9% in AM0. GaAs-on-Si architecture still implies the use of a thick silicon wafer as substrate and consequently a high weight for the device. Recently *Epitaxial Lift Off* was proposed as an alternative to reduce production costs and final product weight. The ELO process enables the separation of the thin-film single-crystal layer from the parent substrate by employing a sacrificial release layer [19][20]. This technology is attractive for solar cell applications since it could reduce manufacturing costs through multiple reuse of the expensive parent wafer following ELO. After lift off the cell can be joined to flexible substrates as plastic films, Ming-Chun Tseng et al. [21] proposed a GaAs thin-film device fabricated by transferring a GaAs solar cell onto a AuGe/Au mirror-coated copper substrate.

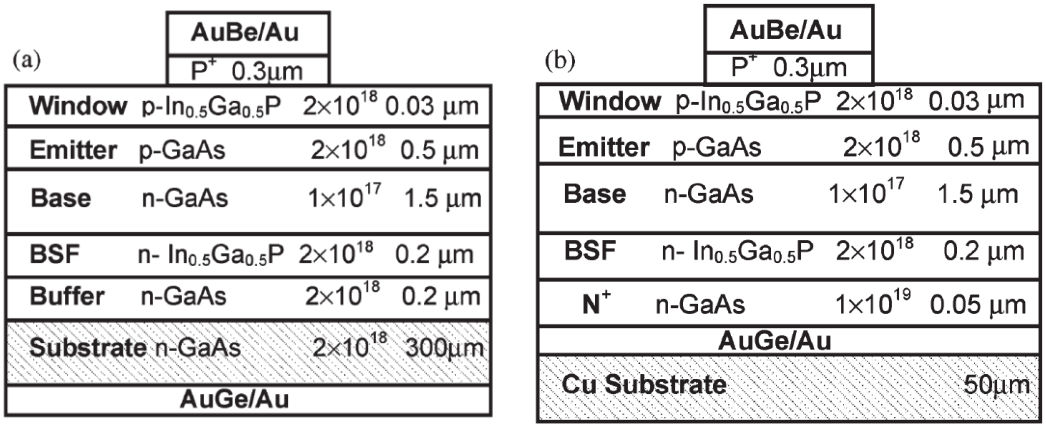

Figure 17: Schematic structures. (a) Conventional GaAs solar cell. (b) GaAs thin film solar cell on copper

With the aid of the excellent copper conductor, the thin-film solar cell exhibits significant improvement in both open-circuit voltage and short-circuit current density. The copper substrate is proposed to be performed via electrochemical deposition. In *Fig.17* it's

possible to compare a traditional GaAs cell structure on wafer and the proposed cell plated with copper on the back side, it's clear that thickness is much lower in the second architecture. High efficiencies can be achieved after transferring the lifted off cell on a plastic substrate, Kyusang Lee et al. [20] showed that p-n junction GaAs solar cells grown on original and reused wafers have power conversion efficiencies of ~23%, under simulated AM1.5 illumination.

InP solar cells

As GaAs also InP was studied as active material in solar cells for space applications as an alternative to traditional silicon cells, because of their superior radiation resistance and high conversion efficiencies. Different technologies were proposed between the '80s and the early '90s, when a high number of research programs was focused on this material for this particular application.

Traditional production technologies and performances

The first generation of InP solar cells was produced starting from a wafer, the junction was formed by thermal diffusion of dopants. The first important studies on InP cells produced with this technology were performed by Akio Yamamoto et al. [22][23]. They were the first to break the 15% efficiency value for InP cells in 1983. They produced homojunction solar cells employing a n^+-*p* structure using thermal diffusion of sulphur or selenium into *p-type* InP substrates. The substrates used had a carrier concentration in the range of $2x10^{15}$- $2x10^{16}$ cm^{-3} and (100) orientation. The diffusion was carried out at 600-700°C for 0.5-6 h in a quartz ampoule. As diffusion sources for S and Se, In_2S_3 and In_2Se_3 were used respectively. The cell front contact grid and active area were defined photolithographically. Front contacts to the n^+ layer were evaporated Au-Ge, and back contacts to the *p* substrate were Au-Zn evaporated and then annealed at 450°C. Solar cells with 25mm^2 total area were cleaved from the n^+-*p* structures. The complete cell was covered with vacuum-deposited SiO as an antireflection coating. the highest efficiency of 16.5% was obtained for a S-diffused cell under AM1 conditions, 1000W/m^2. About one year later the same authors increased cell efficiency to 18.0% in AM1, 1000W/m^2 conditions. They fabricated n^+-*p* junction InP solar using thermal diffusion of sulphur into *p-type* InP substrates. The S diffusion was carried out at 625°C for 3 h in a sealed quartz ampoule containing ln_2S_3 and red phosphorus. The InP substrates had a carrier concentration of $1x10^{16}cm^{-3}$ and (100) orientation. After the removal of the diffused layer on the rear surface of the wafer, the

back ohmic contacts to the cell were made with a vacuum evaporation of Au-Zn followed by an annealing at 450°C for 10 min in flowing N_2 gas. The front contact were formed with gold electroplated through photoresist masks. No annealing was made for the front contacts. Cells with about 25mm^2 total area were sectioned on the diffused wafers by mesa etching with a Br-(1%)methanol solution. Finally, a SiO was vacuum deposited as an antireflection coating. Mesa etching, *Fig.18,* instead of cleavage is believed to help increasing efficiency.

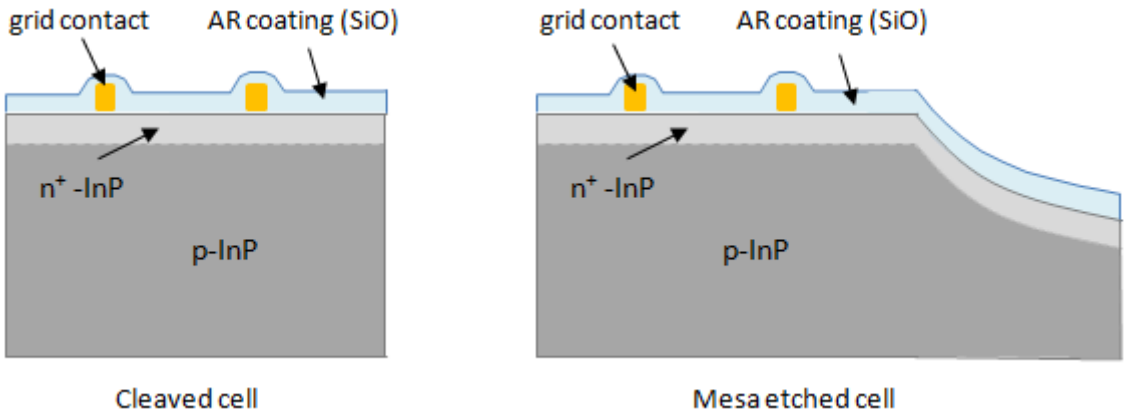

Figure 18: Comparison between cleaved and mesa etched cells

To further improve photovoltaic performance and radiation resistance, the junction structure changed to n^+-*p*-p^+ for several reasons. The use of a p^+-*substrate* with a carrier concentration higher than 10^{16}cm^{-3} brings about a reduction of the series resistance R_s, in the cell. For *p-substrates* in an n^+-*p* cell, a carrier concentration lower than 10^{16} cm^{-3} was chosen in order to attain a wide depletion layer and/or a long minority-carrier diffusion length for a high short-circuit current density I_{sc}. The use of thick p-substrates, however, causes an increase in the R_s, of the cell. By employing a n^+-*p*-p^+ structure, R_s can be reduced while maintaining a high I_{sc}. The n^+-*p*-p^+ structure is expected to have higher radiation resistance than the n^+-*p* structure because of the lower increase in R_s resulting from irradiation, which is based on the low carrier removal rate in a p^+ substrate. To the new structure was also associated a new production technique, that allowed better control on composition and material properties: MOCVD. Mitsuru Sugo et al. [24] used an OrganoMetallic Vapour Phase Epitaxy (OMVPE) apparatus equipped with a horizontal quartz reactor. Triethylindium and PH_3 were used as the In and P sources. Dimethylzinc and H_2S were also utilized as the *p-* and *n-type* dopants. The n^+-*p*-p^+ junction was constructed with successively growing *p* and n^+-*layers* on a p^+(100) InP substrate. *Fig.19* shows a cross-sectional view of a fabricated InP cell. Contacts to the n^+-*layer* (front

contact) and to the p^+-*substrate* (back contact) were made with electroplated Au and with vacuum-evaporated Au-Zn.

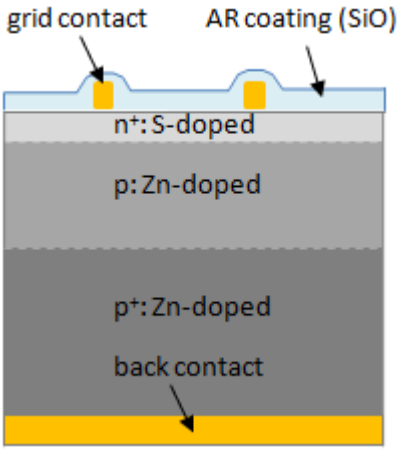

Figure 19: Schematic view of the n+-p-p+ cell

Annealing at 450°C for 10 min was needed to form good Au-Zn ohmic contacts with the p+-substrate. The front contact grid and active area were defined photolithographically. Solar cells about 25mm^2 were formed by mesa etching the surrounding region down to the substrate. This process gave cells with an efficiency up to 20% (active area) in AM1.5 conditions, but the main problem for this architecture is the presence of the thick, fragile and expensive InP wafer as substrate.

To overcome cost related problems, due to the InP substrate, hetero-epitaxial growth was then considered. The main problem for this technology is the presence of a 8% lattice mismatch between InP and Si, leading to increased dislocation density and consequently minor optical and semiconducting properties. Richard W. Hoffman et al. [25] developed high efficiency p^+-n-n^+ homoepitaxial InP solar cells with the intent of applying the technology to hetero-epitaxial InP cell growth on Ge or Si substrates. At the same time M. K. Lee et al. [26] produced p^+-n-n^+ InP cells by hetero-epitaxial MOCVD on Si wafers. *Fig.20* shows the solar cell structure. (l00) oriented n$^+$-Si wafers were used as substrates. Prior to growth, the cleaned Si substrates were preheated at 920°C in a H_2/PH_3 ambient to desorb any native oxide.

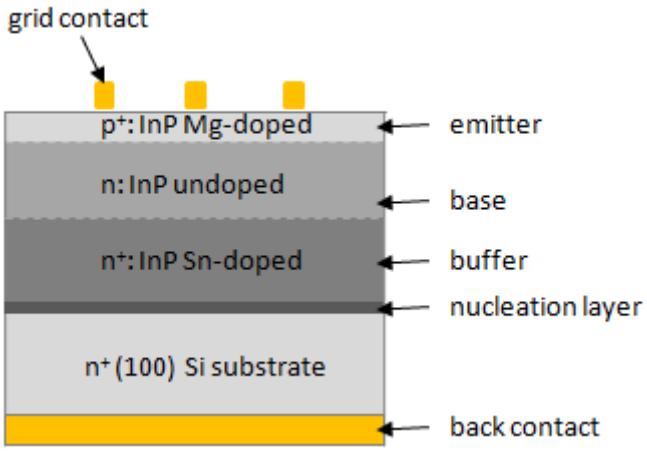

Figure 20: Epitaxial cell structure schematization

After the growth of a thin (less than 70nm) nucleation layer, three epitaxial layers were grown on the substrate successively at 610°C. Each layer consisted of n^+ (Sn), *n* (undoped), p^+ (Mg) regions that were respectively 2.0, 2.0 and 0.1-0.7µm thick. High crystallinity InP epilayers with mirrorlike surfaces were reproducibly obtained. The photoluminescence compared with that of InP homoepitaxy indicated that the undoped InP heteroepilayer is of high optical quality. The metallization was performed by evaporating AuGeNi for the substrate and AuZn through a metal mask for the grid contacts. Wet chemical etching was used in forming mesa-type cells. This resulted in a 11.9% cell efficiency under AM1 conditions.

Recent production technologies and performances

Attention on InP decreased in time due to the high production costs and the improvement of Si, GaAs and multijunction based technology. In the late years though new attention is being given to this material thanks to modern, cheaper production processes. Kuen-Ting Shiu et al. [27] applied the cold-welding technique to bond single-crystal Schottky-type InP ultrathin epitaxial-film solar cells on flexible plastic substrates that can tolerate both tensile and compressive stress by bending around radii as small as 1cm without damage, obtain a power conversion efficiency of η=10.2±1.0% and a high specific power of P_{sp} =2.0±0.2 kW/ kg. The epitaxial solar cell structure is grown by gas source molecular beam epitaxy on a *p-type*, Zn-doped (100) InP substrate. The epitaxial structure consists of a *p-type* InP buffer layer, a lattice-matched Be-doped *p-type* InGaAs etch-stop layer, a 2.0µm thick, lightly *p-doped* InP absorption layer, and finally, a lattice-matched Be-doped *p-type* InP ohmic contact layer. The fabrication of the solar cells starts with electron-beam

evaporation of the p-metal contact with thickness of 300 Å Pt followed by 300 Å Au on both the top InP contact layer and the 25μm thick Kapton sheet. After metal deposition, the wafer is mounted metal-side down on the Pt/Au coated plastic sheet. A bond is formed between the two metal surfaces via cold-welding. The InP substrate and the subsequent InGaAs etch-stop layer are then removed using an acidic etching solution Finally, a 150nm thick indium-tin-oxide (ITO) Schottky diode contact is sputtered. Kyusang Lee et al. [28] demonstrated multiple growths of flexible, thin-film ITO-InP Schottky-barrier solar cells on a single InP wafer via epitaxial lift-off (ELO). Layers protecting the InP parent wafer surface during the ELO process were subsequently removed by selective wet-chemical etching. The active solar cell layers were transferred to a thin, flexible plastic host substrate by cold welding at room temperature. The first and second-growth solar cells didn't exhibit performance degradation under simulated Atmospheric Mass 1.5 Global (AM 1.5G) illumination, and had a power conversion efficiency of η=14.4±0.4% and η=14.8±0.2%, respectively.

The limitation of III-V solar cells is the high cost that stems from price of raw materials, need for a lattice-matched substrate for single-crystal growth, and complex epitaxial growth processes. The turning point for these solar cells is the possibility of producing multicrystalline InP active layers. Ali Javey et al. [29] explored the direct non-epitaxial growth of thin poly-crystalline films of III-Vs on metal substrates by using metalorganic chemical vapour deposition (MOCVD). This method minimizes the amount of raw material used while utilizing a low cost substrate. InP is known to have a low surface recombination velocity of carriers, thereby it's an ideal candidate for efficient poly-crystalline cells where surface/interface properties at the grain boundaries are critical. The grown InP films are 1-3 μm thick and are composed of micron-sized grains that generally extend from the surface to the Mo substrate. They exhibit similar photoluminescence peak widths and positions as single-crystalline InP, as well as excellent crystallinity. Also in this process the choice of substrate metal is critical for obtaining high quality poly-InP films. At the growth temperature, it should have low solubility of both indium and phosphorus. Mo was chosen because there are no intermetallics at the growth temperature, the solubility of In is very low, there are few Mo-P compounds, and no solid solutions.

The possibility of producing InP photovoltaic cells with multicrystaline active layer allows to consider electrodeposition as an alternative to vapour phase deposition. This would led to a further reduction in device price. First electrodepositions of InP were by Cuomo and

Gambio [30] and Elwell et al. [31], in which InP was electrodeposited from molten salts at a temperature of 650°C, the main and most quoted studies on InP electrodeposition in aqueous solutions were performed by Sahu [32][33]. The experimental arrangement for electrodeposition consisted of a 100ml beaker containing a titanium cathode, platinum anode and an aqueous electrolyte containing $InCl_3$ and NH_4PF_6. Before use the titanium cathodes were mechanically polished with fine emery paper, soaked with 0.5 M NaOH and finally ultrasonically cleaned with acetone. The final pH of the bath was adjusted by adding drops of HCl. InP films (0.45 μm) could be obtained under stirred conditions on the titanium cathode within 7min by using a constant current density of 20mA/cm^2 at 22° C. It was observed that near stoichiometric InP, 49% indium and 51% phosphorus, could only be obtained for a particular solution composition of $InCl_3$ (1.25mM) and NH_4PF_6 (58.6mM). The phosphorus content in the deposit was noticed to increase with increasing NH_4PF_6 concentration. However, a slight increase in $InCl_3$ concentration is responsible for an increase (by about 100%) of the indium content in the deposit. At a higher current density (>20mA/cm^2) or lower pH (< 2.0) evolution of hydrogen predominates and only indium could be deposited. At higher pH (> 2.8) or at higher electrolysis temperatures (>50°C) the phosphorus content in the deposit decreases. The same author [34] performed deposition in non aqueous solutions. The experimental setup consisted of a 100mL beaker as electrochemical cell having Ti-cathode, Pt-anode and $InCl_3$ and NH_4PF_6 dissolved in dimethyle formamide (DMF). The Ti foil (0.2mm thick) was polished with fine emery paper, soaked with NaOH (0.5mM) for 5min, washed with deionised water and, finally, ultrasonically cleaned with acetone. Electrodeposition was carried out by varying the solution composition, at 23°C and under constant stirring. The applied current density ranged from 1.5 to 3.0mA/cm^2. A near stoichiometric InP could only be prepared for a particular solution composition of $InCl_3$ (2.0mM) and NH_4PF_6 (38.0). The electrodeposition was carried out for 10min, which corresponds to a thickness of only 0.4μm. Compositional and structural characterization was performed before and after annealing at 300°C in vacuum, 1.3x10^{-3} Pa, for 2 h. The X-ray and optical absorption studies of the as deposited films indicated formation of InP. Annealing did not show any improvement in the quality of the film. The overall studies indicate that the films were poor in quality.

These studies demonstrate that electrodeposition of InP at low temperature is possible both in aqueous and non-aqueous solutions. The quality of deposited film should be improved to

satisfy the high control in morphology and composition required for solar photovoltaic applications.

1.1.4.2.3 Multijunction devices

A single junction device is able to convert solar radiation with energy above the bandgap value of the absorber material. However, as the photon energy increases, the energy in excess of the bandgap does not generate electron-hole pairs, but it's transferred to the lattice as heat which limits the efficiency of the cell. It has been shown theoretically that is possible to increase the conversion efficiency of a device by increasing the number of junctions [12], every junction must have a bandgap value tailored to the range of photon energies available in the solar spectrum. The bandgap values selected for the MJ depend on the number of junctions used. The most common MJ are based either on the mechanical stacking of discrete cells on top of one another or growing, monolithically, the cells in a stack where they are in physical, electrical and optical connection. For both the mechanically and monolithically stacked cells the incident light must pass through the stack from highest bandgap sub-cell to the lowest. Mechanically stacked devices (denoted by the ''//'' between materials) offer greater flexibility in terms of the sub-cells and electrical connections that can be used allowing the utilization of incompatible materials. For many years the highest efficiency device was a gallium arsenide upper cell in tandem with a gallium antimonide solar cell below GaAs//GaSb (1.42 eV// 0.72 eV, efficiency > 30%). The technological difficulties of maintaining the optical arrangement and electrical connections to the individual cells in mechanical stacking made it advantageous to follow the monolithic approach.

To produce a monolithic device two fundamental conditions must be satisfied, different layers must be compatible and allow growth of one cell on another and the current produced must be matched for the sub-cells since they are connected in series. The most successful materials currently used for MJ cells are the ternary III-V alloys based on GaAs and InP. Increasing the number of junctions to increase the solar spectrum absorption the complexity of the device also increases, this caused most MJ devices to be either two or three junction cells (tandem or triple junction). The foundation of monolithically grown MJs was laid with the development of metalorganic vapour phase epitaxy, also known as MOCVD. Selecting a suitable material system, it was possible to grow monolithic device structures able to achieve high efficiencies and more easily integrated into an array. The

development of the $GaInP_2$/GaAs materials system in the 1980s and the invention of the first two-junction (cascade) cell at NREL in 1984 was a key development in III-V monolithic MJ research. This latter work later yielded a high performance (21.8% AM1.5) $GaInP_2$/GaAs device [35]. By 1990 the efficiency had reached 27.3% (*Fig.21*) and provided a path to develop triple junction devices with the $GaInP_2$/GaAs grown on a diffused Ge junction.

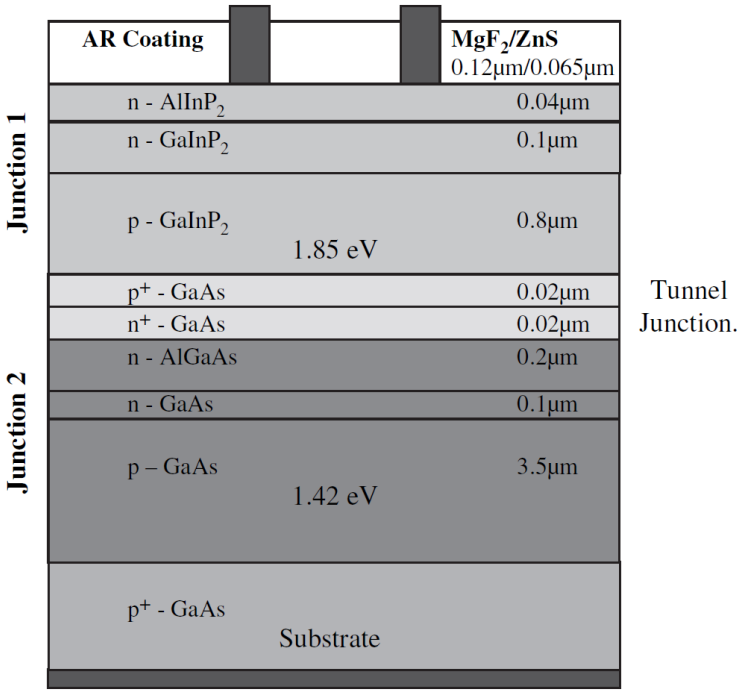

Figure 21: Schematic cross-section of the monolithic GaInP2/GaAs tandem cell grown on GaAs

The current confirmed highest efficiency device is a GaInP/GaAs/GaInAs triple junction device at 37.9% made by National Renewable Energy Laboratory (NREL) in the US. This device was of small area < 0.3 cm^2 and was measured under a low aerosol density direct beam spectrum and under concentration (10 suns). The high cost of MJ cells means that they are not competitive for terrestrial applications even with 30% conversion efficiency values. However, if used to convert concentrated solar radiation, the cost per Watt can be reduced by the concentration ratio. Generally, concentrator systems are not able to be as widely used as flat plate systems and therefore, terrestrial multijunction devices are likely to be limited to locations where long periods of direct sunlight are common. Suitable locations require minimal cloud cover and tracking systems to follow the Sun across the sky.

1.2 ELECTRODEPOSITION PRINCIPLES

Electrodeposition consist in a film growth process which implies the formation of a metallic coating onto a base material occurring through the electrochemical reduction of metal ions from an electrolyte [36]. The corresponding technology is often called *electroplating*. If metal deposition implies the reproduction of moulds to form objects directly in their final shape we talk about *electroforming*. In most cases the metallic deposit thus obtained is crystalline. The electrolyte is a ionic conductor where chemical species containing the metal of interest are dissolved into a suitable solvent (precursors) or brought to the liquid state to form a molten salt. The solvent is most often water, but recently various organic compounds and other ionic liquids are being used for selected electroplating processes.

The electrodeposition process consists essentially in the immersion of the object to be coated in a vessel containing electrolyte and a counter electrode, followed by the connection of the two electrodes to an external power supply to make current flow possible. The object to be coated is connected to the negative terminal of the power supply, in such a way that the metal ions are reduced to metal atoms, that eventually form the deposit on the surface.

Metal deposition processes are and have been utilized for practical purposes in a wide variety of technical fields, ranging from metallurgy and heavy engineering industries to (more recently) microelectronics and nanotechnology. Examples of these applications include the following: gold and gold alloy deposition for electrical contacts in electronic circuits, Cu deposition for microelectronic interconnects, Ni–Fe alloys for magnetic recording heads, or the production of high purity metals. Currently, the most intensively developing branches of electrodeposition are associated with information and energy technologies, as well as microelectronics, sensors and microsystems in general. Suffice here to say that the length scales of commercially synthesized materials covers many orders of magnitude, going from the hundreds of meter of tin-coated strips to the 20-100nm width of copper interconnects.

1.2.1 Electrode processes

A general reaction for the process of metal formation can be written as:

$$\left(M_x L_y\right)^z + nxe \rightarrow xM^0 + yL$$

L is a molecule, an ion, or radical (e.g. H_2O or Cl^-) tightly bound to the metal ion M and thus forming a complex species $(M_xL_y)^z$ which takes part in the charge transfer process. This intermediate compound is usually named the electroactive species. In the previous equation *n* is the net amount of electrons transferred in the overall process to deposit a single metal atom; this is always a positive quantity. *z* is the electric charge of the electroactive species in electron units; *z* can be both negative or positive, and may also be zero. The electric charges of *M* and *L* are not shown in the previous equation. The simplest case of metal ion discharge is that of the simple (hydrated) metal ion, where $n=z$. The reaction in this case is written:

$$M^{z+} \cdot xH_2O + ze^- \rightarrow M^0 + xH_2O$$

where the dot indicates an electrostatic interaction. In general however $n \neq z$, and *n* should not be confused with *z*. We notice that *n* electrons, i.e. a charge of *ne*, need to be transferred for the deposition of one atom of the metal. Consequently, the formation of one mole of the metal requires $N_Ane=nF$ coulombs of electricity (N_A is the Avogadro number $N_A=6.022\times10^{23}mol^{-1}$; $F=N_Ae$ is the Faraday constant $F=96485Cmol^{-1}$). This relationship is referred to as Faraday's Law:

$$m = QA/nF$$

where *m* is the deposited metal mass (grams), *Q* the net charge passed through the circuit (Coulombs), and *A* the atomic weight of the metal. This equation is very important and widely used in practice to calculate the amount of metal deposited during electrolysis or to determine the duration of electrolysis necessary to achieve a predetermined thickness. To determine the deposit thickness (*h*) we can rearrange the previous equation and write:

$$h = ItA/nFS\rho$$

Where *S* is the surface area, ρ is the metal density, *I* the deposition current, and *t* the deposition time. We can observe the importance of the *current density* ($i=I/S$) that governs the rate of the deposition process and it is usually expressed in amperes per square metre, Am^{-2}.

1.2.1.1 Electrode potential and overpotentials

Another important parameter involved in the deposition process is the *electrode potential*. First of all we can define the electrode as the region at which the electrochemical process of interest is occurring; depending on the current direction or the nature of the reaction, it can be the cathode (where a reduction occurs) or the anode (where oxidation occurs); in

some cases an electrode can comprise both cathodic and anodic areas. In a purely electrochemical sense it is the half-cell element as a whole, i.e. the combination of the solid electrode and the electrolyte region in contact with the electrode, where a predetermined reaction is occurring. In some cases the reaction forms a new phase and the term "electrode" refers to a particular sequence of phases together with their interfaces. An example of electrode is the reference electrode where the equilibrium between Ag and AgCl takes place; this electrode is schematically indicated by the series of phases Ag|AgCl|KCl present at the interface. The potential φ of the electrode is the potential drop between the solution and the bulk of the metal, otherwise called the Galvani potential difference.

It is conventional to measure the electrode potential with reference to some other electrode having a constant, reproducible and stable potential. Various reference electrodes of this kind exist; the Standard Hydrogen Electrode (SHE) uses the equilibrium between H^+ and hydrogen gas to generate this potential, and it is most often used as a standard. Its potential at any temperature is defined equal to zero. Electrode potential expressed relative to SHE is symbolized by the letter E. SHE is too inconvenient to be practical; in the laboratory practice therefore one can use other reference electrodes (calomel or silver/silver chloride electrode), using other reactions to generate the potential. Current density and electrode potential of any given electrode reaction at steady state are related to each other through a one-to-one correspondence; however, when a growth process is occurring at one electrode, conditions are rarely stationary. For this reason a potentiostatic process (at *E*=const) occurs with the current density changing over time; similarly, a galvanostatic process (with *i*=const) is usually accompanied by variations in E. This can be due to different phenomena occurring during deposition, as the surface state (roughness, morphology) evolution with time and the change in composition of the solution adjacent to the electrode (concentration of chemical species, pH). These changes can be significant in the first stages of deposition.

The electrode potential at which the current density *i* is zero assumes particular importance. If this potential corresponds to the thermodynamic equilibrium of a well defined electrode process it is defined as the *equilibrium potential* for this process, E_{eq}. This potential is described by the Nernst equation and is related to the thermodynamic activity of the electroactive species in solution. For the simplest case of an equilibrium between a metal ion and the reduced metallic solid it is:

$$E_{eq} = E_0 + RT/nF\,(\ln a_{M^{z+}})$$

R=8.3145J/molK (gas constant), and T is the absolute temperature. E_0 is called the *standard potential* and is observed under standard conditions (unit activity for all the species involved, T=298K, and atmospheric pressure). It is important to realize that the thermodynamic equilibrium implies that the overall rate for the process of interest is zero; however, this equilibrium is achieved by the balance of two partial reactions occurring in opposite directions. Ershler and Shlygin [36] were the first to introduce the term "exchange current density" i_o to quantify the rate of these two partial processes at equilibrium. To obtain metal deposition at a finite rate it is necessary to shift the electrode potential in the cathodic (negative) direction from its equilibrium value. It follows that a negative potential shift speeds up reduction processes whereas a positive shift accelerates anodic reactions (oxidation). The value of this shift is called the overpotential (overvoltage) of this process and is usually indicated by the greek letter η:

$$\eta = E - E_{eq}$$

In this notation the overpotential has a definite sign, in another notation just its modulus is considered and it is distinguished in anodic (positive) or cathodic (negative). The overpotential value can range from few mV to some V, and it's strictly related to process rate and deposit morphology. Considering Piontelli classification we know that high melting temperature metals also have high overpotentials, at the same time low melting metals have low overpotentials. This classification is closely related to the exchange current densities measured for the reduction/oxidation of these elements: high values of i_o correspond to low overpotential and vice-versa. This classification is valid only if the metal ions in solutions aren't involved in complexes. In this latter case in fact it is possible to alter the value for η at a given current density and correspondingly change the characteristic film morphology, that is generally small grained for high values of η.

When deposition is performed using a soluble anode of the metal we want to deposit, the potential difference between the two electrodes, U, can be defined as the sum of the two overpotentials and the ohmic drop, RI, in the solution:

$$U = |\eta_a| + |\eta_c| + RI$$

Sometimes a phenomenon called *underpotential deposition* can occur, this implies the deposition of the metal from the solution at a potential higher than the equilibrium one.

1.2.1.2 Current efficiency

In most practical processes part of the overall current (charge) is consumed by side processes occurring in parallel with metal deposition. It is therefore important to determine the relationship between the current densities of the different processes occurring simultaneously at some potential. Side reactions can be of various nature. An example of side reaction is hydrogen evolution that may occur in aqueous baths, as the result of water electrolysis:

$$2H_3O^+ + 2e^- \rightarrow H_2 + 2H_2O$$

Other side reactions can occur, as partial reduction of metal ions in solution:

$$M^{z+} + ne^- \rightarrow M^{(z-n)+}$$

When an alloy is deposited the side reaction can be the co-deposition of the other metal, in this last case the current density for each process is strictly related to the composition of the codeposited alloy. When other side reactions proceed, the ratio between the partial current of the process of interest i_p and the overall current is called *current efficiency,* CE:

$$CE = i_p/\Sigma_j\, i_j$$

Normally this value is expressed in percent. The current efficiency is equal to the ratio of the actual deposit mass Δm to its theoretical value calculated from Faraday's Law:

$$CE = nF\Delta m/QA$$

The values of CE can differ widely for different metal deposition processes. CE depends on metal, solution composition and deposition conditions.

1.2.2 Electrodeposition solvents

A plating bath is often classified depending on the solvent used to dissolve the precursors, the most used system are based on aqueous solvents, but there are also organic solvents and ionic liquid based systems.

1.2.2.1 Aqueous solutions

All general concepts described before are valid for aqueous solutions. In this systems the main cathodic side reaction is the hydrogen evolution process, that causes a local increase of pH. At the anode we can have metal dissolution or oxygen evolution depending if the anode is soluble or not:

- Anode dissolution: $M^0 \rightarrow ze^- + M^{z+}$
- Oxygen reduction: $4OH^- \rightarrow 4e^- + O_2 + 2H_2O$

$$\text{or:} \quad 2H_2O \rightarrow 4e^- + 4H^+ + O_2$$

It's possible to notice that the anodic oxygen evolution process implies a local acidification of the solution. Together with the cathodic hydrogen evolution process it can cause changes in the overall solution pH.

In principle, metal deposition is possible from simple solutions of some salt or other soluble compound containing the metal in the form of cation, anion or complex. One component solutions are however rarely used in practice since they do not provide high quality deposits. It is conventional to include in commercial electrolites some additional compounds, each playing a specific role. Inorganic acids or alkali are added to increase the electrical conductivity of the aqueous solution; more conductive electrolytes permit to decrease voltage increasing thickness uniformity of the deposit. Substances taking no part in electrode processes are called "supporting electrolytes". Moreover, acids and alkali are also used for adjusting pH since the standard recipes for plating solutions also indicate optimum pH values. Acidity has to be stable and constant throughout the entire bath (the cell volume) including the region near the electrode; this is achieved by addition of buffering agents. Buffering is especially necessary when hydrogen evolution occurs because the latter leads to higher pH near the electrode as a consequence of H^+ consumption.

Along with these most important components, so-called 'additives' are also widely used in practice. An example of this sort of substances are surfactants added to the solution to decrease the surface energy of the electrode and facilitate the detachment of hydrogen bubbles from the surface. Adhesion of hydrogen bubbles to the electrode leads to undesirable 'pitting', that is the occurrence of macroscopic point defects at the plated surface. Additives can be classified as: 'brighteners' (allowing the production of bright deposits without post-deposition polishing), or 'levellers' (filling pre-existing scratches or pits and smoothening the surface). Additionally, some additives contribute to decrease internal stresses in the deposit, activate anode dissolution, increase current efficiency, suppress dendrite formation, etc. The additives usually inhibit the deposition, this is translated in the increase of η.

The concentration of additives in the plating solutions is usually between 10^{-4} and 10^{-2} moles per litre, but some of them can influence the deposition process at much lower concentrations. The mechanism of their action is based predominantly on adsorption at the electrode surface, resulting in much higher surface concentration as compared to the solution bulk. Additive concentration decreases in the course of plating as a result of

incorporation by the growing deposit or following decomposition at the cathode. Therefore periodic correction of each additive concentration is necessary.

1.2.2.2 Non-aqueous solutions

Electrodeposition of metals from non-aqueous solutions has attracted attention in the last few years. Conventional aqueous solutions cannot be always used as electrolytes due to the liberation of hydrogen molecule during electrolysis, narrow electrochemical windows, low thermal stability, and evaporation. These are the reasons why scientists have searched for new non-aqueous solutions to electrodeposit metals. The role of non-aqueous electrolytes in technology has become more and more important. Facing serious problems concerning environment and energy, scientists have found out new possibilities in electrochemical applications using non-aqueous electrolytes. However, there are technical issues that make their commercialization hard, such as cell heat balance, corrosion of cell components, low current efficiency, dendritic deposition, and similar difficulties. To overcome these problems intensive and systematic studies (scientific and technological) of new electrolytes are required.

Molten salts and ionic liquids

Ionic liquids are, as the name predicts, composed solely of ions [37][38] . Although the intensively investigated and, in technical processes, widely used high-temperature molten salts also fulfil this definition, it was suggested in recent years to distinguish “artificial” ionic liquids from “classical” molten salts as systems with melting points below 100°C. General features of molten salts are as follows: they can function as solvents, liquids (like water), have good heat capacity, can attain very high temperatures (>700°C), and conduct electricity. Typical application temperatures are 450–1025°C but can be as low as 70°C. The most common molten systems are LiCl–KCl, NaCl–KCl and LiF–CaF_2, but also other mixtures are used and investigated. Interesting air-stable ionic liquids are nowadays available and increasingly employed as a replacement for organic solvents in basic research because they are non-volatile, and in some cases stable up to temperatures of 400°C.

In contrast to the classical molten salts, which are highly corrosive and make it difficult to find container materials that can withstand chemical attack by the melts, the design of electrochemical cells is much easier for low-melting ionic liquids. Historically, they can more or less be divided into three groups:

- systems based on $AlCl_3$ and organic salts such as 1-butylpyridinium chloride (BP^+Cl^-), 1-ethyl-3-methylimidazolium chloride ($[EMIm]^+Cl^-$), 1-butyl-3-methylimidazolium chloride ($[BMIm]^+Cl^-$) and derivatives;
- systems based on organic cations as of the previous calss and BF_4^-, PF_6^- and SbF_6^-;
- systems based on the aforementioned organic cations with anions of the type $CF_3SO_3^-$, $(CF_3SO_2)_2N^-$ and similar.

Liquids made on the basis of the latter ions are stable under ambient conditions with only low water uptake. Ionic liquids behave very differently to traditional molecular liquids when they are used as solvents. ILs are usually non-volatile, in most cases non-flammable, less toxic, good solvents for both organic and inorganic materials, and can be used over a wide temperature range. Another virtue is that the problems associated with hydrogen evolution typical of protic solvents can be eliminated, because ionic liquids are usually aprotic. Moreover, ILs show good electrical conductivity and have wide electrochemical windows. In electrochemistry the stability window of a solvent is of great importance. Any solvent is suitable for conducting a range of electrochemical experiments on species dissolved within it, if only these species are more easily oxidized or reduced than the solvent itself. In ILs, it is found that the constituent anions are oxidized at sufficiently large potentials and organic cations undergo reduction at sufficiently low ones. The potentials, at which these bulk processes appear, determine the accessible electrochemical window for each liquid. The stability windows for ILs remain in the broad range from 2 to 6 V, but typically are 4.5V.

The main drawbacks of ILs stem from the low conductivity, the high production costs, the high viscosity and the high density. The high viscosity of ILs causes some difficulties in their handling. Viscosity plays an important role in conductivity and self-diffusion because conductivity is inversely proportional to the medium viscosity, so as viscosity increases, the conductivity falls.

Organic solvents

Electrodeposition of metals and alloys from non-aqueous solutions [37] (such as aromatic, dimethylsulfone, acetone and acetates) provides cost-effective and easy to control technique to fabricate thin films and intermetallic compounds. Organic solvents are less aggressive towards materials that are normally reactive with aqueous electrolytic solutions.

Organic solvents allow the use of a wider range of complexing ions with respect to aqueous solutions. Disadvantages are mainly safety related, e.g. toxicity, flammability and explosion hazard, moreover water absorption can lead to undesired side reactions, conductivity and solubility of some precursors are low and finally the high cost is in some cases a limiting factor in the utilization of such solvents.

Examples of deposition from such solvents are: Lutetium–cobalt thin film electrodeposited from anhydrous dimethylsulfoxide (DMSO), Zirconia films (ZrO_2) deposited in a non-aqueous electrolyte based on absolute ethyl alcohol, methanol, acetonitrile and propylene carbonate baths used to electrodeposit zinc telluride and so on.

Chapter 2

Experimental Procedure

In this part the experimental procedure is described, the research work was performed in different times and laboratories: most of the investigation on direct electrodeposition of InP was performed in Politecnico di Milano while pure indium deposition, In and red phosphorus composite deposition, phosphorization and indium deposition followed by red phosphorous dropcasting were studied in University of California, at Berkeley. For this reason the description of experimental procedure will be organized depending on the process used to finally obtain InP. After the description of sample preparation and production, information are given also about further treatments and characterization processes performed on the samples themselves; examples are thermal treatments, x-ray diffraction measurements, electrochemical characterization and SEM/EDX analysis.

2.1 DIRECT INDIUM PHOSPHIDE CODEPOSITION

Experiments on direct InP deposition were performed mainly in Politecnico di Milano, the main target of this set of experiments is to verify and study the possibility of depositing indium phosphide in a single process via electrochemical methods.

2.1.1 Raw chemicals and solutions

Several solutions were prepared for electrodeposition of InP, using reagents with purity between 98% and 99.99%. The first passage before the production of the individual solution for deposition was the preparation of concentrated stock solutions of indium precursors. It's possible to distinguish among different sets of experiments depending on solution composition: solution based on Ni-P plating, solution based on Sahu works [32][33][34], solutions with complexing agents and solutions with alcohols. The different solutions are classified and the main ingredients are reported in the following table (*Table 2.1).* The reagents used were:

- Indium trichloride anhydrous: powder, purity 98 and 99.99%, indium corporation of America
- Indium sulfate anhydrous: powder, purity 98%, sigma-aldrich
- Indium sulfate hydrate: powder, purity 99.99%, sigma-aldrich
- Phosphorous acid: crystals, purity 99%, sigma-aldrich
- Phosphoric acid: solution 85wt.% in H_2O, purity 99%, sigma-aldrich
- Sodium hypophosphite monohydrate: crystals, purity 99%, sigma-aldrich
- Ammonium hexafluorophosphate: crystals, purity 98%, sigma-aldrich
- Citric acid: crystals, purity 99.5%, sigma Aldrich
- Sodium citrate dihydrate: crystals, purity 99%, sigma-aldrich
- Triethanolamine (TEA): liquid, purity 99%, sigma-aldrich
- Ethylenediaminetetraacetic acid disodium salt dehydrate: powder, purity 99%, sigma-aldrich
- Hydrochloric acid: solution, assay 37%, sigma-aldrich

Table 2.1: solution classification and composition

set of solutions	solvent	In precursors	P precursors	complexing agents
Ni-P based	Water	$InCl_3$ $In_2(SO_4)_3$	H_3PO_3 H_3PO_4 NaH_2PO_2	-
Sahu work based	Water	$InCl_3$ $In_2(SO_4)_3$	NH_4PF_6	-
With complexants	Water	$InCl_3$ $In_2(SO_4)_3$	H_3PO_3 H_3PO_4 NaH_2PO_2	EDTA, TEA, citric acid, sodium citrate
With alcohols	Water and alcohols	$InCl_3$ $In_2(SO_4)_3$	H_3PO_3 H_3PO_4 NaH_2PO_2	-

2.1.1.1 Solutions based on Ni-P electrodeposition

In Ni-P electrodeposition and electroless deposition [39][40][41] aqueous solutions of Ni precursor salts and phosphorous precursors are prepared. Normally Ni precursors include nickel sulphate and nickel chloride, while phosphorus precursors can include phosphoric acid, phosphorous acid and sodium hypophosphite. In particular sodium hypophosphite is a reducing agent that promotes Ni reduction in electroless deposition, to activate its

oxidation, and thus the metal ion reduction, high temperatures (even higher than 90°C) are normally needed.

All this phosphorus precursors were used in the attempt of depositing indium phosphide. More than a hundred samples were produced trying to emulate Ni-P deposition, changing deposition conditions solution composition and substrates. Some significant examples will be described.

Solution composition

Plating solution ranged in composition and precursor concentration over a wide range of values. Indium precursors were used solely or combined into the same deposition bath and were $InCl_3$ and $In_2(SO_4)_3$. The total In^{3+} concentration in the solution ranged from 0.375mM to 0.25M. Phosphorus precursors were also used in combination and individually, they were phosphoric acid, phosphorous acid and sodium hypophosphite hydrate. The phosphoric acid concentration ranged from nil to 5M, phosphorous acid concentration from nil to 1M, and Na hypophosphite concentration from nil to 0.5M. For every precursor in some experiments the concentration in solution was nil, because different mixes of precursors were considered and the P sources were used individually too, together with indium salts.

2.1.1.2 solutions with complexing agents

This group of solution can be considered as a subclass of the Ni-P based, in fact precursor type and concentrations are more or less the same as in the previous set for both phosphorus and indium. The main difference is in the presence of complexing agents for In. The idea of using comlexants for indium derived from the inability to obtain any InP peak in the XRD analysis of the samples obtained with the simpler solutions without this kind of additives. The principle is that of lowering indium reactivity in solution, decreasing its reduction potential and thus making reduction easier for phosphorus precursors, this is usually done when depositing alloys of metals with difference in reduction potential [36] and to control relative concentration of alloy metals into the deposit. In fact standard reduction potential of phosphoric acid and phosphorous acid to phosphorous are lower than that of In^{3+} to metallic indium and consequently indium reduction preferentially occurs (*Table 2.2*).

Table 2.2: Standard reduction potential for several precursors

Reaction	Standard potential E_0 (V vs SHE)
$In^{3+} + 3e^- \rightleftharpoons In$	-0.3382
$H_3PO_4 + 2H^+ + 2e^- \rightleftharpoons H_3PO_3 + H_2O$	-0.276
$H_3PO_3 + 3H^+ + 3e^- \rightleftharpoons P + 3H_2O$	-0.454
$HPO_3^{2-} + 2H_2O + 2e^- \rightleftharpoons H_2PO_2^- + 3OH^-$	-1.65
$HPO_3^{2-} + 2H_2O + 3e^- \rightleftharpoons P + 5OH^-$	-1.71

Solution composition

For what concerns In and P precursors, it's possible to repeat what previously described for Ni-P based solutions. Indium precursors were used individually into the deposition bath and were $InCl_3$ and $In_2(SO)_4$. The total In^{3+} concentration in the solution ranged from 65mM to 250mM. Phosphorus precursors were also used in combination and individually, they were phosphoric acid, phosphorous acid and sodium hypophosphite hydrate. Since phosphorous acid was found to cause precipitation even in very small amounts if used together with sodium hypophosphite, this combination of phosphorus precursors wasn't used for deposition. In this sense the main phosphorus precursors used were phosphoric acid with either sodium hypophosphite or phosphorous acid. The phosphoric acid concentration ranged from 26mM to 750mM, phosphorous acid concentration from nil to 100mM, and Na hypophosphite concentration from nil to 750mM. The main difference with respect to the previous set of solutions is the presence of complexing agents for In, as sulfamic acid, Triethanolamine (TEA), Ethylenediaminetetraacetic acid tetrasodium salt (a salt of EDTA), citric acid and sodium citrate. The concentrations reported are referred only to the solution that showed stable and allowed deposition afterwards. Only one stable bath was produced with TEA and sulfamic acid with a concentration of respectively 2% in weight and 265mM. the other stable solution was based on a mix of EDTA and citrates, with EDTA tetrasodium salt ranging from 10% to 14% in weight and citric acid and sodium citrate from 75mM and 175mM to 150mM and 350mM respectively.

2.1.1.3 Solutions based on Sahu works

In his papers Sahu affirms the possibility of depositing InP starting from an aqueous solution of an indium salt and NH_4PF_6 as phosphorus precursor. Experimental procedure and solution composition described in the papers were reproduced with the aim of depositing indium phosphide. Sahu's work is the most quoted when talking about

electrodeposition of InP from aqueous solutions, for this reason it was considered as a reliable source.

Solution composition

In this set of solutions only $InCl_3$ was used as In precursor as reported in Sahu's works, two groups of solutions were prepared and deposition was performed in several conditions. The first set of solutions was prepared with the same composition of the solution giving the best results in terms of composition and XRD analysis in Sahu's experiments. These solutions were composed by $InCl_3$ 1.25mM and NH_4PF_6 58.3mM, the addition of some drops of concentrate HCl was necessary, as reported in the papers, to reduce the pH below 3 and stabilize the solution, thus avoiding precipitation of indium hydroxides. The second set of solution was prepared maintaining the same $InCl_3$ to NH_4PF_6 ratio in solution but increasing their concentration respectively to 12.5mM and 583mM. This modification was performed since no deposition was observed for several plating conditions in the first group of solutions, because of the higher precursor concentration in the solution a slightly higher amount of HCl was necessary to reduce the solution pH and stabilize the In^{3+} ions from precipitation.

2.1.1.3 Solutions with alcohols

Also this set of solutions can be considered as a subgroup of the Ni-P inspired, since also in this case precursors for indium and phosphorus are the same. The use of this kind of solution with addition of alcohol arises from a study performed by Cavallotti and Djoki [42] on the process of Ni-P deposition with sodium hypophosphite. In this work a mechanism is proposed that highlights the importance of the presence of a metal hydroxyl ion in solution, in fact the hypophosphite can only interact with this particular ion of Ni forming a complex that is adsorbed on the electrode surface and subsequently decomposed in Ni and P thanks to the Hydrogen evolution process. Given this process the presence of alcoholic species was thought to help the stabilization of an indium hydroxide ion in solution.

Solution composition

Indium chloride and sulphate were used individually as indium precursors, phosphorous acid and sodium hypophosphite as P precursors were also used individually. In this solutions phosphoric acid wasn't used since, as confirmed by literature and electrochemical

studies performed during research, it's a complexing agent for indium and would hinder interaction between In ions and hypophosphite ions. Three different alcoholic species were used, methanol ethanol and isopropyl alcohol (IPA). In^{3+} concentration ranged from 20mM to 50mM, Na hypophosphite concentration from 40mM to 80mM and phosphorous acid concentration from 20mM to 30mM. The solvent was a mixture of water and alcohols, none of the solutions with ethanol gave stable conditions even for amounts of alcohol lower than 1% in volume. Stable solutions were produced with mixtures of water and IPA or water and methanol, IPA concentration ranged from 20% to 37.5% in volume, while methanol concentration from 13% to 93% in volume. Indium chloride showed to be more suitable for this alcoholic solvent mixture and was used preferentially over indium sulphate. Moreover when dissolving both indium chloride and indium sulphate in IPA the formation of a concentrated solution in water was necessary before the addition of the alcohol, while indium chloride was easily dissolved directly in methanol.

2.1.2 Materials and experimental procedure

Given that the experiments were held in different laboratories the experimental procedure was conserved over the whole set of experiments, the main differences are due to the different raw chemicals, the different instrumentation and different materials, i.e. glassware and substrates for deposition. All the deposition were performed in the hood.

2.1.2.1 Deposition with solutions inspired to Ni-P

Solutions for deposition, with the range of compositions aforementioned, were prepared from concentrated aqueous stock solutions of indium chloride and indium sulphate. These solutions were diluted to the right amount and added with the phosphorus precursor necessary for the particular solution composition desired. This procedure allows to obtain an higher reproducibility if compared to the individual preparation of solutions with a given amount of indium precursor. Several deposition conditions were considered, first of all an important parameter was P/In ratio in solution, this ranged from 0.5 to 400, moreover for every solution three current densities were considered: low 5mA/cm^2, intermediate 15-20mA/cm^2 and high 30-50mA/cm^2. These three current density were considered for every solution at room temperature, therefore, for the current density condition giving more promising results also high temperature, 50-95°C, depositions were performed.
Since indium is stable in solution only for low pH values, deposition was always performed in acidic environment with pH between 1 and 2.5.

Stock solutions were prepared in volumetric flasks, some of the solution was poured into a 100mL beaker, there addition of phosphorus precursors was performed. After phosphorus precursor addition and stirring to get complete dissolution, the mix was added with water to reach the desired volume in other volumetric flasks, typically a 50mL flask. The initial quantity of stock solution poured into the beaker depended on the concentration of the stock solution itself and on the concentration desired for the final solution.

Figure 22: Hot plate magnetic stirrer(left) and galvanostat/potentiostat (right)

After solution preparation, deposition was performed. The standard two electrodes plating cell was made up of a 100mL beaker filled with the solution and set on a hot plate magnetic stirrer (*Fig.22*), inside the electrolyte the two electrodes were placed and connected to the Elektro Automatic EA-PSI 8065-05 T galvanostat/potentiostat. The working electrode was connected to the negative pole of the generator and the counter electrode to the positive pole. In all the depositions a Pt net counter electrode was used, while both commercial Molybdenum foil (0.1-0.5mm thick) and commercial AISI 304 foil (1mm thick) were used as working electrodes. Before utilization both molybdenum and AISI 304 foil underwent a cleaning and etching step to activate the surface for the subsequent deposition. The cleaning procedure was the same for the two materials and consisted in a two-step sonication in acetone and IPA for 10 minutes followed by deionised water rinse. Finally the substrate was dipped in 10% HCl for 5 minutes and carefully rinsed with DI water.

Before deposition the working electrode was masked with kapton tape to expose a surface of about 1cm^2, electrical connections to the generator were performed with copper cables provided with an alligator on one side to fix the electrodes.
Deposition was performed in the described two electrode setup under imposed current. Current flow was monitored with a multimeter to verify its actual value. In high temperature depositions the solution was first brought to the desired temperature while covered to avoid evaporation, subsequently with the help of a vertex thermometer, temperature was kept stable and deposition was performed.
In all the depositions solution stirring was achieved and kept constant with the utilization of a magnetic stir bar. Deposition time ranged from 10 minutes to one hour depending on solution type, current density and temperature.
After deposition the samples were carefully rinsed with deionised water and then dried with N_2 gas.

2.1.2.2 Deposition with complexing agents

Since this group of experiments can be considered a continuation of the Ni-P based depositions, the experimental procedure is the same, the deposition cell and setup are conserved also for these samples. Only AISI 304 was used as substrate and the cleaning procedure was the same as in the previous group of depositions. The only differences arise from the presence of complexing agents, these chemicals allowed higher pH for the deposition bath without indium compounds precipitation, therefore the pH range for deposition was shifted to higher values and ranged between 1.9 and 3.7.
All these depositions were performed at high temperature with the aim of activating phosphorus precursor decomposition to give elemental phosphorus bound to the metallic indium, therefore deposition temperature was included in the 50 to 90°C range. Deposition current lied in the 10 to 30mA/cm^2 range for times going from 10 to 20 minutes. The usual rinsing and drying procedure was performed also for these samples.

2.1.2.3 Sahu's work based deposition

Two main sets of deposition were performed trying to reproduce Sahu work: depositions in the same conditions reported in Sahu's paper and deposition performed increasing precursor concentration in the solution and varying temperature and current density. The experimental setup is the same described for the first group of experiments, the only differences, excluding the precursors used for phosphorus, are the substrate used as

working electrode and the cleaning procedure performed before deposition. The applied current density ranged between 10mA/cm^2 and 100mA/cm^2, the temperature between room and 80°C, and the pH was adjusted for every solution at a pH between 2 and 3 as suggested in the papers, with the utilization of concentrated HCl. Deposition time was in the 7 to 15 minutes range.
Commercial titanium foil (3mm) was used as a substrate for deposition, the cleaning procedure was based on a 10 minute sonication in acetone. After grease removal in acetone, etching and surface activation was performed in 5% HF for 1 minute. Finally accurate DI water rinse was performed and kapton tape mask applied after drying. After deposition a thorough water rinse was performed followed by drying with nitrogen gas.

2.1.2.4 Deposition with alcoholic solutions

The experimental procedure described for the other depositions is valid also in this case, the only differences lie in the substrate used, only molybdenum indeed was used as working electrode for deposition. The cleaning and activation procedures were the same used for substrates in Ni-P based depositions as the masking step. Only few experiments were held with these solutions, the cell setup consisted in the 2 electrode system described before, the current density was lower than in the other groups of deposition, due to higher overvoltages, and ranged between 4 and 15mA/cm^2. Deposition was performed only at room temperature since an increase in temperature caused precipitation to occur and alcohol evaporation. Deposition times were higher than in the other cases and went from 60 to 150 minutes. Water rinse after plating was performed in a delicate way to avoid deposit detachment, due to the scarce adhesion, and drying didn't occur by nitrogen gas flow but was performed in atmosphere at room temperature.

2.2 INDIUM AND RED PHOSPHORUS COMPOSITE DEPOSITION

This process was inspired to some papers describing the possibility of codepositing copper and red phosphorus powder via electrodeposition to produce copper-phosphorus alloys after thermal treatment [43][44].
This set of experiments was performed exclusively in University of California Berkeley.

2.2.1 Raw chemicals and solutions

From a compositional point of view this set of solution was simple, the bath was made up of an indium precursor and a suspension of red phosphorus powder was obtained through

agitation with a magnetic stir bar. Consequently, besides deionised water, the only chemicals used for these solutions were:

- Indium trichloride anhydrous: powder, purity 99.99%, indium corporation of America
- Indium sulfate hydrate: powder, purity 99.99%, sigma-aldrich
- Red phosphorus: powder,100μm average size, purity 99%, sigma-aldrich

2.2.2 Materials and experimental procedure

First of all concentrated stock solutions of indium sulphate and chloride were prepared into volumetric flasks. Consequently dilution was performed transferring a given amount of stock solution in another volumetric flask using 5 or 10mL graduated pipettes. Finally solution was brought to volume by addition of deionised water into the flask. The solution obtained could be used to deposit pure indium; to obtain the suspension, addition of red phosphorus to the indium salt solution was performed.
Depositions occurred under the hood, in a Pyrex 100ml beaker, set on a hot plate magnetic stirrer. The cell setup is the two electrode one, with a platinum plate or pure indium plate counter electrode and a molybdenum foil working electrode connected respectively to the positive and negative pole of a potentiostat/galvanostat. Electrical connections were performed through copper cables with an alligator on one end to allow electrode fixing and electrical contact. In the beaker was placed a Teflon magnetic stirrer used to stir the solution at a constant rate, this allowed the phosphorous suspension to be stable and the phosphorus distribution in the deposit to be homogeneous.
To avoid any kind of contamination in the solution, all the glassware and tools used during solution preparation and deposition (plastic tweezers, stir bar, platinum counter electrode) were cleaned with concentrated nitric acid. The working electrode used as substrate was a 250μm thick Molybdenum foil, this was cleaned using the two step acetone and IPA sonication for 10 minutes, therefore every substrate was rinsed with water and etched with 10% HCl for 5 minutes. Finally after an accurate deionised water rinse the substrates were masked with kapton tape to expose a surface of about $2cm^2$.

Three different deposition processes were considered in this set of experiments (*Fig.23*):

- One step composite deposition: the In precursor solution was added with phosphorus powder and deposition was performed in one single step. The best conditions were found to be 10 to $15mA/cm^2$, for a time between 15 and 20

minutes, at room temperature and with a solution composed by $In_2(SO_4)_3$ 100mM or $InCl_3$ 200mM, added with 3-5g/L of red phosphorus powder;

- Two step deposition: a seed layer of pure indium was deposited, subsequently red P powder was added to the solution and a second deposition was performed to obtain the composite; in this process a thin seed layer of pure indium was deposited at room temperature, imposing a current density of 10mA/cm^2 for 5 minutes. Subsequently the 100mM $In_2(SO_4)_3$ solution used for pure indium deposition was added with 5-50g/L of red phosphorus powder and composite deposition was performed for 15 to 20 minutes at room temperature. Stirring and electrode position was adjusted to increase red phosphorus powder incorporation in the deposit. Current density was held constant at 20-25mA/cm^2.
- Three step deposition: after the seed layer and the composite deposition a new pure indium solution was used to plate an indium capping layer on the composite. In this last process after the first two stages, performed as described in the two step deposition, a new solution composed by $In_2(SO_4)_3$ 100mM or $InCl_3$ 200mM was prepared. The sample was immersed in this new solution and deposition of a pure In capping layer was performed at room temperature. In these cases, because of the insulating nature of phosphorous particles in the deposit and on its surface, voltage during deposition was much higher. For this reason lower current density and longer times were necessary to produce the top indium layer, current density was held constant for 5 to 8 hours at 2 to 5mA/cm^2.

After deposition all the samples were cleaned with deionised water in a gentle way, to avoid the red P particles on the surface to detach during rinsing. After water rinse, samples were set in the hood until completely dry, a nitrogen gas flow would have caused surface red P particle to be removed.

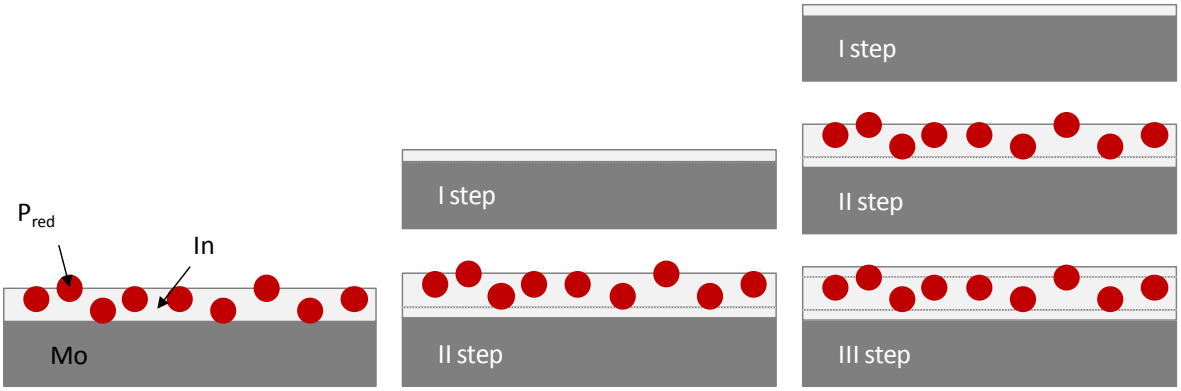

One-step deposition *Two-step deposition* *Three-step deposition*

Figure 23: Schematic view of the three different structures

2.3 PURE INDIUM PLATING AND SUBSEQUENT PHOSPHORUS INCORPORATION

In this set of experiments the production of pure indium deposits was performed to assist two different phosphorus incorporation process: the first process involved red phosphorus dropcasting on the surface and successive thermal treatment to promote diffusion into the indium; the second process, phosphorization, wasn't performed in the laboratory I was working in, but by members of the laboratory I was strictly cooperating on the indium phosphide project, in Berkeley.

2.3.1 Raw chemicals and solutions

Two different groups of solutions were prepared to deposit pure In layers. A first set of solutions was prepared with the dissolution in deionised water of $In_2(SO_4)_3$, a second series of solution was prepared with a mix of $In_2(SO_4)_3$ and $InCl_3$ with the introduction of complexing agents to improve deposit quality and homogeneity. This addition was performed because of the need of thinner and high quality deposit that couldn't be obtained with the pure indium sulphate solution. The idea of using citrates as complexing agents to increase deposit quality derives from a patent [45] that claims the possibility of producing highly homogeneous and pure films of indium for thin film photovoltaic applications using citrates. Considering the red P dropcasting two different techniques were used: at first a aqueous suspension of P_{red} was produced, consequently to improve the dropcasted layer quality a suspension in hexane was employed. Besides deionised water the chemical used for these solutions were:

- Indium sulfate hydrate: powder, purity 99.99%, sigma-aldrich

- Indium trichloride anhydrous: powder, purity 99.99%, indium corporation of America
- Citric acid: crystals, purity 99.5%, sigma-aldrich
- Sodium citrate dihydrate: crystals, purity 99%, sigma-aldrich
- Red phosphorus: powder,100μm average size, purity 99%, sigma-aldrich
- Hexane: liquid, assay 95%, sigma-aldrich

2.3.2 Materials and experimental procedure

Before starting with any operation all glassware and plastic tools were cleaned with concentrated nitric acid to avoid any contamination. The first step was the production of concentrated stock solutions of indium sulfate and chloride into volumetric flasks. Consequently dilution was performed transferring a given amount of stock solution in another volumetric flask using 5 or 10mL graduated pipettes. Finally solution was brought to volume by addition of deionised water into the flask. For solutions with complexing agents an intermediate step was necessary, with the addition of citrates to the concentrated stock solution in a 100mL beaker. After mixing the solution was poured in a volumetric flask and brought to volume with DI water.

2.3.2.1 DC deposition

Both depositions with and without complexing agents were performed in the two electrode setup with the cell structure described before: plating was performed under the hood, in a 100ml Pyrex beaker, set on a hot plate magnetic stirrer. In the beaker, a pure indium plate counter electrode and a molybdenum foil working electrode were placed and connected respectively to the positive and negative pole of a potentiostat/galvanostat. Electrical connections were provided through copper cables with an alligator on one end to allow electrode fixing and electrical contact. In the beaker was placed a Teflon magnetic stir bar used to stir the solution at a constant rate. It is possible to distinguish between the deposition conditions for the pure indium sulfate solution and for the solution with complexing agents:

- Pure Indium sulfate solution: the stock solution was diluted to a concentration ranging from 25 to 200mM, the current density was held constant during plating at values going from 5 to 25mA/cm^2 for times in the 15 to 60 minutes range. Deposition temperature was varied between room and 65°C.

- Solution with complexing agents: the stock solution was added with sodium citrate and citric acid and diluted to the desired concentration. Thanks to the higher cathodic efficiency current density was increased in the 5 to 60mA/cm^2 range. On the other hand deposition time was decreased, since thinner deposits were needed, in the 1 to 10 minutes range. All deposition were performed at room temperature both with a mix of $In_2(SO_4)_3$ and $InCl_3$ or with one of these precursors individually. Total In normality ranged from 50 to 200mN, citric acid concentration varied between 100 and 250mM and sodium citrate concentration from 50 to 350mM. For these solutions, calculations were performed in order to achieve the correct pH value, mentioned in the patent as optimal [45] at a value of 2, without the addition of other acidic species. HCl addition to correct the pH was indeed found to be detrimental for deposit quality. Calculation led to the correct citric acid and sodium citrate concentration to be respectively of 250 and 50mM for a solution containing 100mM indium chloride and 50mM indium sulfate. In these depositions besides the conventional constant current plating another process was studied. To allow an higher nucleation rate in the first stages of deposition a two step current profile was imposed: a short time nucleation period with high current density, ranging from 40 to 60mA/cm^2 , for 2 to 10 seconds; a growth stage lasting 1-2 minutes with lower current density, 25-30mA/cm^2.

Another difference between the solutions without complexants and with complexants is the molybdenum substrate cleaning and etching procedure. For the pure indium sulfate solution the conventional two-step sonication in acetone and IPA for 10 minutes was performed, followed by 5 minutes 10% HCl immersion. After each step an accurate DI water rinse was performed. No kapton tape mask was applied to avoid any type of contamination from external agents during deposition in pure indium sulphate solutions. Considering deposition from solutions with citrates the pre-treatment on the molybdenum substrate was longer and more aggressive. In this case indeed after the two step sonication in acetone and IPA a stronger etching process was performed. After water rinsing and drying with nitrogen gas flow, the Mo foil was sonicated in concentrated (37%) HCl for 20-30 minutes. This aggressive process was needed to assure an homogeneous deposition of indium in the first plating stages. After sonication in HCl the foil was rinsed with DI water and dried with nitrogen gas.

2.3.2.2 Pulsed current deposition

This should be considered as a preliminary work since few depositions were tried and deeper studies should be performed on this topic. Pulsed deposition was performed to increase nucleation rate to obtain higher homogeneity in the deposition of pure indium.
Using a concentrated solution of indium sulfate and indium chloride with total indium concentration 1N, depositions were performed in the three electrode setup using an Princeton Applied Research EG&G electrochemical station. The cell consisted in a 100mL Pyrex beaker filled with 30mL of solution and the three electrodes dipped in the solution itself. Both solutions with citrates and without citrates were used, all with the same indium normality. Solution with complexing agents were added with 250mM citric acid and 50mM sodium citrate. Pulsed deposition was performed on commercial Molybdenum foil using a platinum wire as a counter electrode and a saturated SSC electrode as reference. Mo foil was cleaned following the double step sonication in IPA and acetone followed by concentrated HCl sonication described before.
Several parameters must be considered when describing pulsed deposition, pulse cycles lasted for 1 or 2 seconds with duty cycle from 6.25% to 50%. Average current density ranged from 20 to 100mA/cm^{2}s resulting in current densities during pulse in the 166mA/cm^2-2A/cm^2 range. All depositions, performed at room temperature, lasted 6 to 90 seconds and were performed under constant stirring, with a magnetic stir bar. After deposition samples were rinsed with DI water and dried with nitrogen gas flow.

2.3.2.3 Red phosphorus dropcasting

After indium deposition red phosphorous dropcasting was performed. When describing this process it's necessary to perform an introduction on the different architectures considered in the production of this kind of samples, shown in *Fig.24*.
With the gradual understanding of the effect of thermal treatments on the samples different architectures were considered. The first architecture was the simpler, a suspension of red P in water was dropcasted directly on the plated indium layer, in time the suspension was performed in hexanes since this solvent gave better results in terms of suspension stability and evaporation time, thus leading to higher quality red P layers.

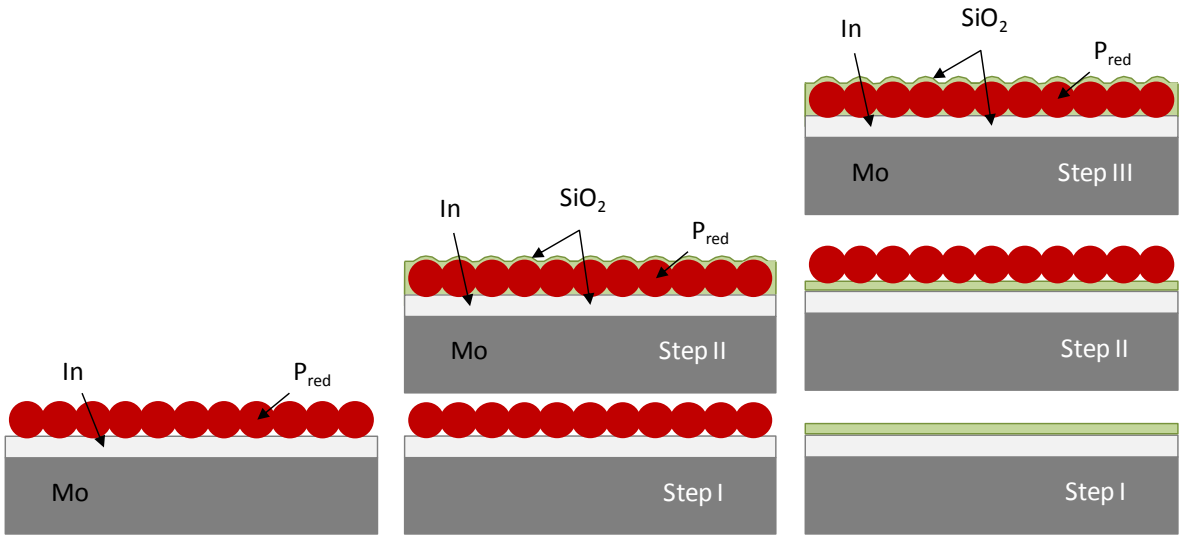

Figure 24: Schematic view of the different dropcasting structures

The second architecture implied the addition of a capping layer on red phosphorus, this was produced by thermal evaporation or e-beam evaporation of silicon dioxide on the dropcasted deposit. This modification was mainly related to the need of constraining the indium layer in its original shape even at high temperature, indium melts at 156°C and this is a problem in thermal treatments, and avoid phosphorus sublimation. Red phosphorous suspension was performed in hexanes. The last architecture implied the addition of another silicon dioxide capping layer, this was deposited by thermal evaporation on the dropcasted phosphorus (suspension still performed in hexanes); the resulting architecture is then: substrate-In-SiO_2-P_{red}- SiO_2. The three architectures are represented schematically in *Fig.24.*

The dropcasting process was performed with a 1mL plastic pipette. The suspension was prepared by weighting 45mg of red phosphorus powder on a precision scale, then the powder was poured into a 0.5mL plastic test-tube. Afterwards addition of hexane (or water in the first trials) to reach 0.5mL was performed, the test-tube was sealed and mechanical agitation performed. Finally the suspension was sucked with the pipette and dropcasted on the sample trying to produce a uniform layer.

Phosphorization process

The phosphorization process was performed in UC Berkeley in the professor Javey's lab. This process is performed on pure indium samples, these were previously capped with silicon dioxide. This passage is fundamental since SiO_2 avoids indium to move on the

surface in the molten state during heating, SiO_2 was thermally or electron-beam evaporated to form a 50-100nm layer. An official laboratory procedure was followed to evaporate silicon dioxide: deposition was performed at 10^{-6} torr. Once the sample is capped it can be phosphorized, the standard phosphorization process used in Javey's lab is performed in a LPCVD chamber and implies:

- T: 750°C
- P: 97torr of 10% PH_3 in H_2 flow
- t: 23 min

Since samples prepared by electrodeposition were thicker than the vapour phase produced samples usually phosphorized in that group, time of phosphorization was increased to 30-60 minutes depending on sample thickness. The process is based on supersaturation of the In melt with P that leads to progressive InP crystallization.

2.4 ELECTROCHEMICAL CHARACTERIZATION

Electrochemical characterization was performed to determine the behaviour of reactants used in different solutions to plate indium and indium phosphide. In all the measurements the same experimental procedure was conserved. Most of the test were performed in UC Berkeley using Princeton Applied Research EG&G electrochemical station. Solutions were prepared with different compositions and concentrations using glassware previously cleaned with concentrated nitric acid to remove any contamination.
Testing was performed in 50mL beakers filled with 30mL of solution. Plastic beakers were used when the solution investigated contained indium precursors to avoid indium adsorption on the glass walls of the beaker itself. Before proceeding with the measurement all the solutions were covered with Parafilm and bubbled with N_2 for 30min. during the measure bubbling was interrupted but solution stirring was performed using a magnetic stir bar and a stirring plate. Most of the tests were performed at room temperature, some at 90°C to activate sodium hypophosphite.

Before describing testing parameters it is necessary to give a brief overview over the electrochemical characterization process. To determine the behaviour of solutions used in this research a particular characterization method was used, called cyclic voltammetry. This test can be performed using a three electrode system, one stationary electrode used as reference (RE), one working electrode (WE), whose potential is measured with respect to

the reference electrode, and a counter electrode (CE) that allows current flow, together with the working, through the solution. In cyclic voltammetry a cyclic potential history is imposed between the working and the reference and the current flow is measured between the working and the counter.

Several potential histories can be imposed, potential can decrease and then increase or vice versa, one or more cycles can be imposed, scan rate can be slow or fast. All these parameters influence the information that can be gained from this kind of test. Changing the potential, at the working electrode surface several reactions can occur. When an electrochemical reaction occurs at the WE surface the measured current is altered and thus it's possible to identify electrochemical processes occurring during the polarization by representing the exchange current density as a function of the imposed potential. It's possible to localize an oxidation process when an anodic current peak is present, while a reduction process is denoted by the presence of a cathodic current peak. Reversible processes show both cathodic and anodic peaks that are normally shifted in potential because of the non ideality of the polarization process, the hysteresis is indeed greater as the scan rate increases.

A schematic polarization curve is reported in *Fig.25,* this reports a forward cathodic curve, peaks relative to oxidation and reduction process are highlighted and hydrogen evolution potential limit is marked in light blue. It is also possible to notice the hysteresis between oxidation and reduction peaks due to the non dynamic nature of the polarization process that implies non equilibrium conditions.

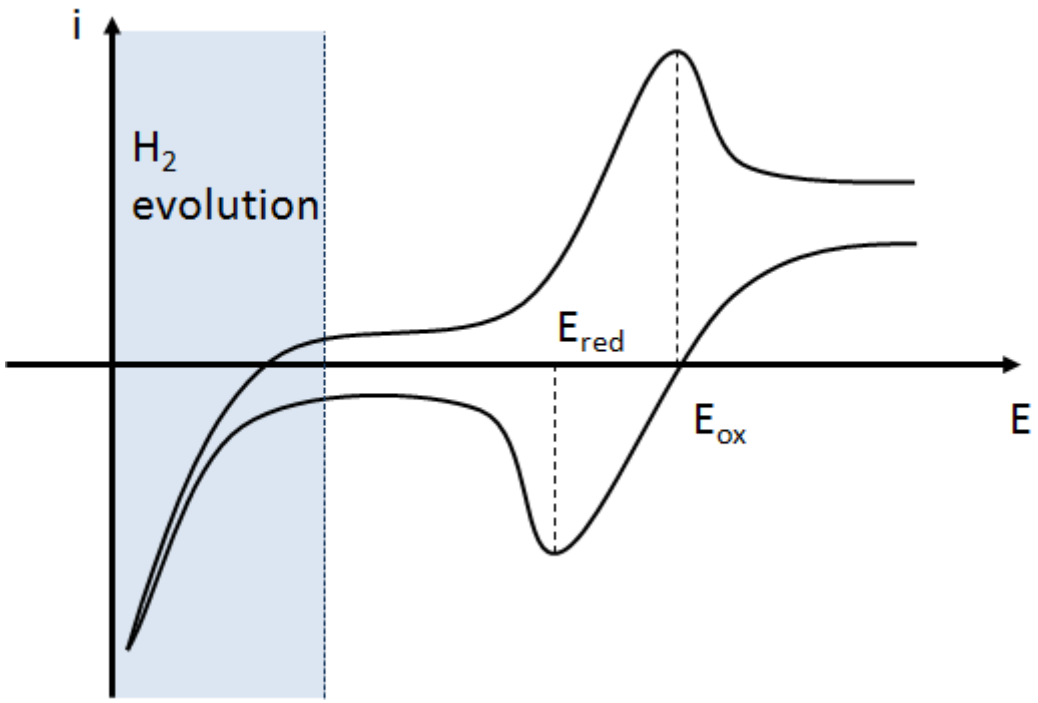

Figure 25: Schematic example of forward cathodic cyclic polarization curve

During testing several solution were characterized, a KCl saturated Ag/AgCl electrode (SSC electrode) was used as reference having a potential of +0.199V vs SHE. Measurements were performed on different materials, molybdenum and nickel were used as working electrodes depending on the solution to be characterized. A Platinum wire was used as CE. Scan rate ranged between 10 and 100mV/s, starting potential was normally set as E_{max} and ranged between 0 and +0.6V vs SSC, and E_{min} was varied between -0.8 and -1.5V vs SSC. Froward cathodic polarization was always performed. After every measure RE and CE were cleaned to avoid contamination and the working electrode was substituted or cleaned with alumina powder and rinsed with DI water. Working electrode was masked with Kapton tape to expose a small surface, depending on the material the exposed surface was 0.5 or 1cm^2.

2.5 MICROSTRUCTURAL AND COMPOSITIONAL ANALYSIS

Samples were analyzed to determine their composition and their morphology, all the promising samples underwent XRD, EDX and SEM analysis. Some AFM measures were performed on pure indium deposits to determine their surface roughness.

2.5.1 XRD principles

Diffraction effects are observed when electromagnetic radiation impinges on periodic structures with geometrical variations on the length scale of the wavelength of the radiation. The interatomic distances in crystals and molecules amount to 0.15–0.4nm which correspond, in the electromagnetic spectrum, to the wavelength of x-rays having photon energies between 3 and 8keV.

Accordingly, phenomena like constructive and destructive interference should become observable when crystalline and molecular structures are exposed to x-rays. In XRD analysis a sample is impinged by a planar monochromatic x-ray wave, the impingement angle is varied gradually and diffracted signal is collected after impingement.

Constructive interference conditions, that are the basis for the understanding of a diffraction pattern, are given by Bragg's law:

$$2dsin\theta_B = n\lambda$$

Where d is the crystal lattice spacing, λ is the x-ray wavelength, θ is the impinging angle and n an integer number. Bragg equation may be obtained geometrically, which is visualized in *Fig.26*.

A set of crystallographic lattice planes with distances d_{hkl} is irradiated by plane wave x-rays impinging on the lattice planes at an angle θ. The relative phase shift of the wave depends on the configuration of atoms as it is seen for the two darker atoms in the top plane and one plane beneath. The phase shift comprises of two shares, Δ_1 and Δ_2 , the sum of which equals $2dsin\theta$ for any arbitrary angle θ. Constructive interference for the reflected wave, however, can only be achieved when the phase shift $2dsin\theta$ is a multiple of the wavelength.

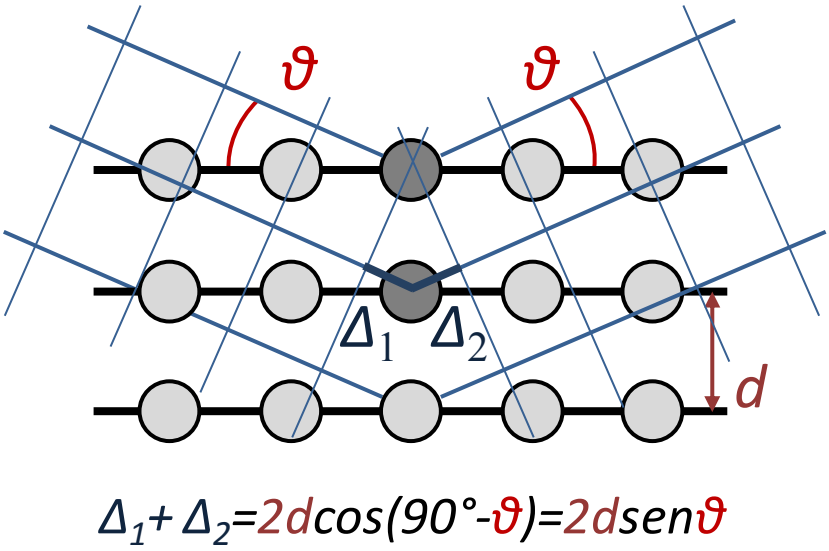

Figure 26: Visualization of the Bragg equation

Once that principle is clear, it's possible to determine the composition of a crystalline sample observing its diffraction pattern and being aware of the wavelength of the impinging x-rays, since every material has different cell parameters.

The most common scanning procedure is the $\theta/2\theta$ scan. The working principle of a $\theta/2\theta$ scan is visualized in *Fig.27*.

The sample is positioned in the centre of the instrument and the probing x-ray beam is directed to the sample surface at an angle θ. At the same angle the detector monitors the scattered radiation. The sample coordinate vectors s_1 and s_3 lie in the scattering plane defined by K_0 and K. During the scan the angle of the incoming and exiting beam are continuously varied, but they remain equal throughout the whole scan: $\theta_{in}=\theta_{out}$.

The $\theta/2\theta$ scan can also be understood as a variation of the exit angle when this is determined with respect to the extended incoming beam and this angle is 2θ for all points in such a scan. This is the reason for naming the measurement procedure a $\theta/2\theta$ scan. The quantity measured throughout the scan is the intensity scattered into the detector. The results are typically presented as a function of $I(2\theta)$ type.

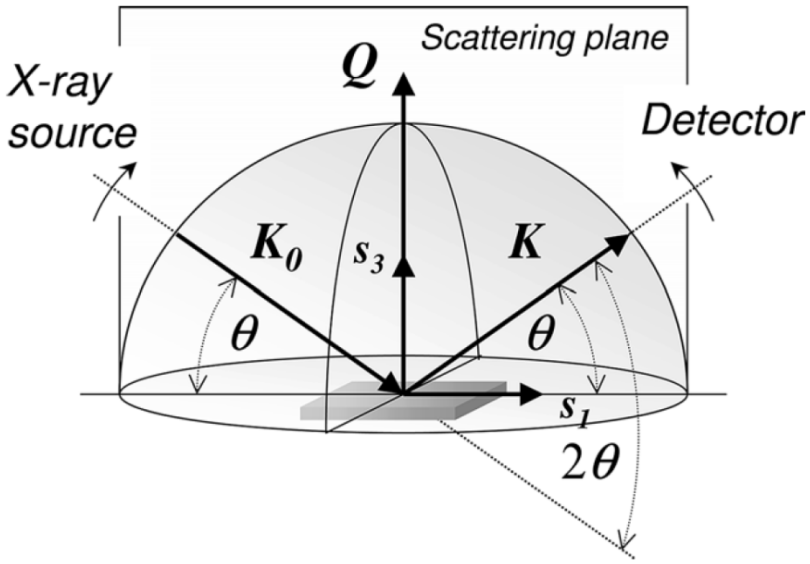

Figure 27: Schematic representation of a θ/2θ scan

Samples were analyzed using Cu k_α radiation with wavelength of 1.54A.

2.5.2 SEM and EDX principles

The scanning electron microscope, SEM, uses a focused beam of high-energy electrons to generate a variety of signals at the surface of solid specimens. The signals that derive from electron-sample interactions reveal information about the sample including external morphology and chemical composition. In most applications, data are collected over a selected area of the surface of the sample, and a 2D image is generated that displays spatial variations in these properties. Areas ranging from approximately 1cm to 5μm in width can be imaged in a scanning mode using conventional SEM techniques with magnification ranging from 20X to approximately 30,000X. The SEM is also capable of performing analyses of selected point locations on the sample; this approach is especially useful in qualitatively or semi-quantitatively determining chemical compositions, using EDX.

Accelerated electrons in a SEM carry significant amounts of kinetic energy, this energy is dissipated as a variety of signals when the incident electrons are decelerated in the solid sample. These signals include secondary electrons, that produce SEM images, backscattered electrons (BSE), diffracted backscattered electrons (EBSD) and photons (characteristic X-rays that are used in EDX analysis). Secondary electrons and backscattered electrons are commonly used for sample imaging: secondary electrons are most valuable for showing morphology and topography while backscattered electrons are most valuable for illustrating compositional contrast in multiphase samples, i.e. for rapid

phase discrimination. X-rays are generated by inelastic collisions of the incident electrons with electrons in discrete orbitals (shells) of the atoms in the sample. As the excited electrons return to lower energy states, they yield x-rays that are of a fixed wavelength (that is related to the difference in energy levels of electrons in different shells for a given element). Thus, characteristic x-rays are produced for each element in a material that is "excited" by the electron beam. SEM analysis is considered to be "non-destructive", i.e. x-rays generated by electron interactions do not lead to volume loss of the sample, so it is possible to analyze the same materials repeatedly.

EDX makes use of the generated x-rays to obtain a localized chemical analysis. All elements from atomic number 4 (Be) to 92 (U) can be detected in principle. Qualitative analysis involves the identification of the lines in the spectrum and is fairly straightforward owing to the simplicity of X-ray spectra. Quantitative analysis (determination of the concentrations of the elements present) entails measuring line intensities for each element in the sample and for the same element in calibration standards of known composition. By scanning the beam in a television-like raster and displaying the intensity of a selected x-ray line, element distribution images or 'maps' can be produced. The scanning electron microscope (SEM), which is closely related to the electron probe, is designed primarily for producing electron images, but can also be used for element mapping, and even point analysis, if an X-ray spectrometer is added. There is thus a considerable overlap in the functions of these instruments.

Characteristic X-rays result from electron transitions between inner orbits of the atoms in the material, which are normally full. An electron must first be removed in order to create a vacancy into which another can 'fall' from an orbit further out. In electron probe analysis vacancies are produced by electron bombardment. The *critical excitation energy* (E_c) is the minimum energy which bombarding electrons (or other particles) must possess in order to create an initial vacancy. In electron probe analysis the *incident electron energy* (E_0) must exceed E_c and should preferably be at least twice E_c to give reasonably high excitation efficiency. Electron bombardment not only produces characteristic X-ray lines resulting from electron transitions between inner atomic shells but also a continuous X-ray spectrum, or continuum, covering all energies from zero to E_0. This continuum arises from interactions between incident electrons and atomic nuclei. The intensity of the continuum decreases monotonically with increasing X-ray energy.

Samples were analyzed both with SEM instrument and with SEM/EDX system allowing to obtain information on morphology and on elemental composition. The main difference between XRD and EDX in the compositional analysis stands in the fact that the first gives information about compounds in the sample, while the second gives information about the elements.

2.5.3 AFM principles

The AFM is an imaging method in the family of scanning probe microscopes, surface imaging is achieved through the motion of a cantilever with a tip placed in proximity of the surface. The essential property of the AFM is the interaction force between the tip and the sample, which depends on their distance. At close contact the force is repulsive while at a larger separation the force is attractive. This results in different operation modes which should be chosen according to the characteristics of the sample, since each mode has different advantages. With this technique size measurements or even manipulations of nano-objects may be performed.

The probe is a micromachined cantilever with a sharp tip at one end, which is brought into interaction with the sample surface, to detect the displacement of the cantilever a laser is reflected off the back of the cantilever and collected in a photodiode. The measure can be performed only if there is an actual force interaction between the sample and the probe, the typical force diagram as a function of tip to surface distance is reported in *Fig.28*. In the contact regime, the cantilever is held less than a few angstroms from the sample surface, and the interatomic force between the cantilever and the sample is repulsive. In the non-contact regime, the cantilever is held on the order of tens to hundreds of angstroms from the sample surface, and the interatomic force between the cantilever and sample is attractive. This causes cantilever to bend downwards when feeling attractive forces and upwards when feeling repulsive forces.

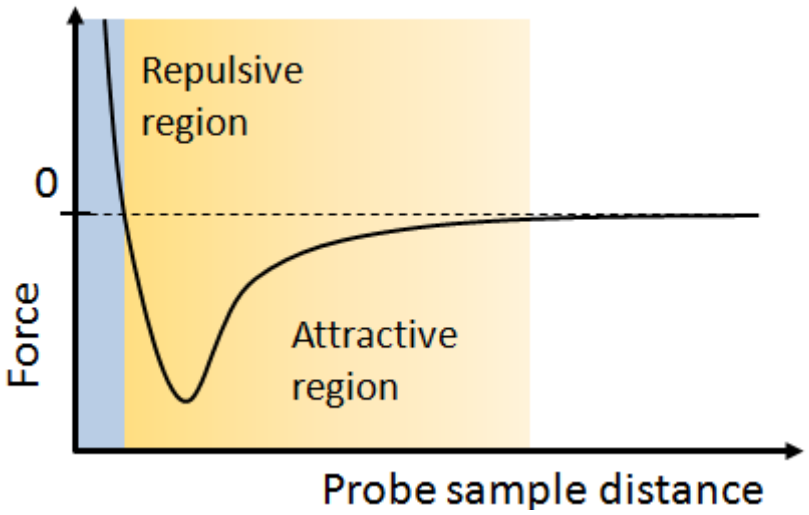

Figure 28: Qualitative force-distance diagram

In the contact mode, the tip makes soft "physical contact" with the surface of the sample. The deflection of the cantilever Δx is proportional to the force acting on the tip, via Hook's law, $F=-k\Delta x$, where k is the spring constant of the cantilever. In contact-mode the tip either scans at a constant small height above the surface or under the conditions of a constant force.

In non contact mode, the probe operates in the attractive force region and the tip-sample interaction is minimized. The use of non-contact mode allows scanning without influencing the shape of the sample by the tip-sample forces.

The force measured by AFM can be classified into long-range forces and short-range forces. The first class dominates when we scan at large distances from the surface and they can be Van der Waals force or capillary forces (due to the water layer often present in an ambient environment). When the scanning is in contact with the surface the short range forces are very important, in particular the quantum mechanical forces (Pauli Exclusion Principle forces). In tapping mode-AFM the cantilever is oscillating close to its resonance frequency. An electronic feedback loop ensures that the oscillation amplitude remains constant, such that a constant tip-sample interaction is maintained during scanning. Forces that act between the sample and the tip will not only cause a change in the oscillation amplitude, but also change in the resonant frequency and phase of the cantilever. The amplitude is used for the feedback and the vertical adjustments of the piezoscanner are recorded as a height image. Simultaneously, the phase changes are presented in the phase image (topography). The advantages of the tapping mode are the elimination of a large part of permanent shearing forces and the causing of less damage to the sample surface, even with stiffer probes. Different components of the sample which exhibit different adhesive

and mechanical properties will show a phase contrast and therefore even allow a compositional analysis.

Samples were analysed with AFM to determine their roughness, tapping mode was used with silicon tips. Normally scanning was performed on a $5x5\mu m^2$ or $10x10\mu m^2$ area, with a 1μm/s scan rate on 200 lines with 200 samplings per line.

2.6 THERMAL TREATMENTS

Thermal treatments were performed on several samples for different reasons, the main focus of thermal treatments, namely annealing, was that of inducing interactions between phosphorous and indium present in the deposits, to form indium phosphide.

Depending on the nature of the sample considered and on the skills matured during several thermal treatments, different technologies and process parameters were adopted.

Three instruments were used to perform thermal treatments on our samples, CVD chamber, RTA chamber and CSS chamber.

Before describing in detail the parameters used for the annealing process it's necessary to briefly describe the instruments: normally these instruments are used to perform physical or chemical vapour deposition, in the CVD chamber for example the reaction leading to deposition occurs due to thermal decomposition of precursors.

The Chemical Vapour Deposition chamber consists in an horizontal quartz tube that is heated normally by resistive heating, a schematic view of a LPCVD setup is represented in *Fig.29.* Operational temperature can be varied between 300°C and more than 1000°C, and pressure is normally in the 0.25-2torr range.

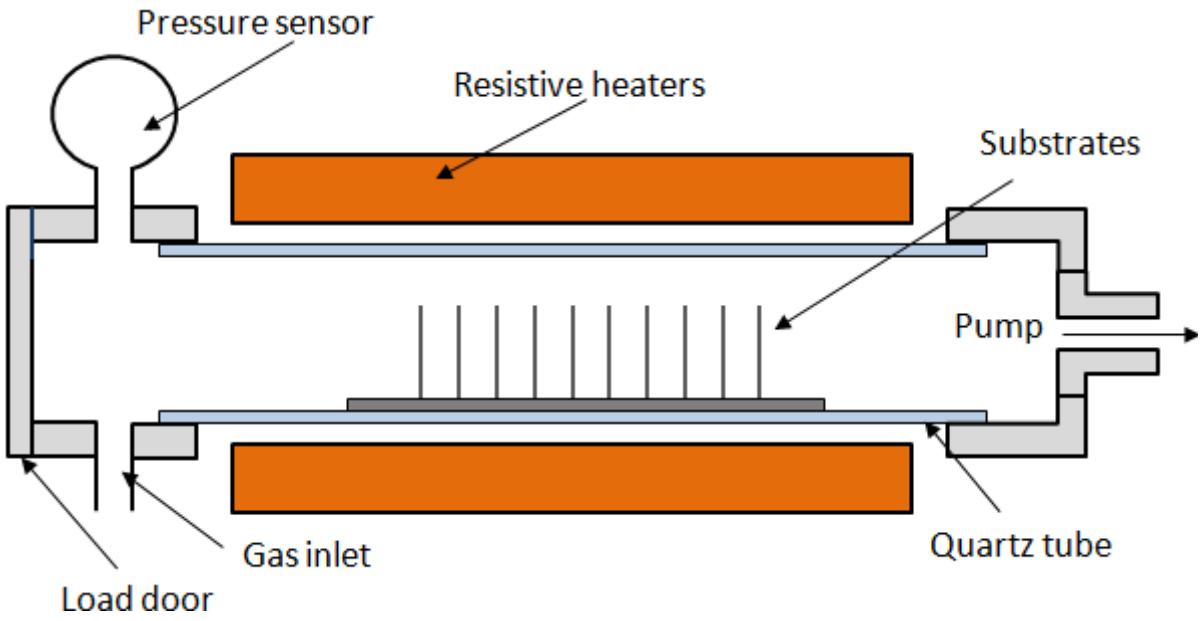

Figure 29: Schematic view of a LPCVD chamber

Lamp heated rapid thermal annealing RTA (*Fig.30*) and rapid thermal processing RTP equipment are using lamp heating in order to ramp up and cool down semiconductor wafers pretty fast. This equipment is therefore mainly used for applications where the substrate needs to be brought to a certain temperature just for short time. The high ramp rates allow a short overall process time and keep the thermal budget, i.e. the total time of exposure to high temperature, of the sample low. Because of the design of the heaters, RTA is used mainly for single wafer treatment, thus samples have to be treated one by one.

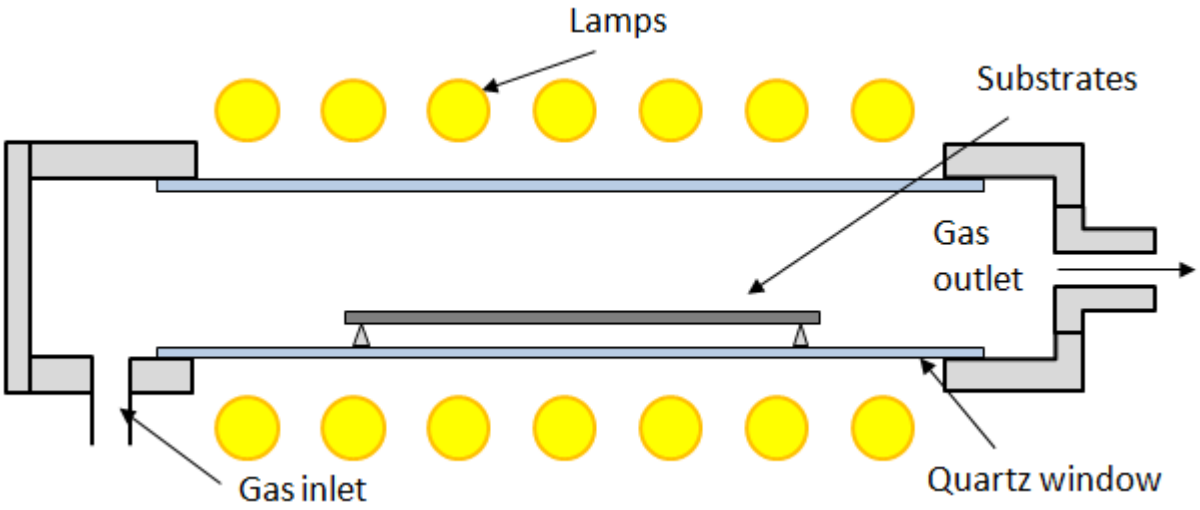

Figure 30: Schematic view of an RTA chamber

Closed Space Sublimation, CSS, is designed to obtain an high chemical efficiency of converting source into a deposited layer. As it can be seen in the schematic representation, *Fig.31,* it contains a source plate which is the source of material to be deposited. Source

material is transferred to the substrate, facing the source plate at short distance, thanks to the temperature difference between the two plates. The source plate is normally kept above 1000°C and the substrate in the 600-900°C range. The separation between the two plates is kept from few mm to 1cm maximum. Due to this narrow gap, the environment between the two plates becomes saturated with the source material and high transfer efficiencies are achieved. As in RTA heating is performed through lamps, this allows high heating rates. For annealing no source material was introduced in the chamber but the system was simply used to heat up and cool down in a controlled environment the samples.

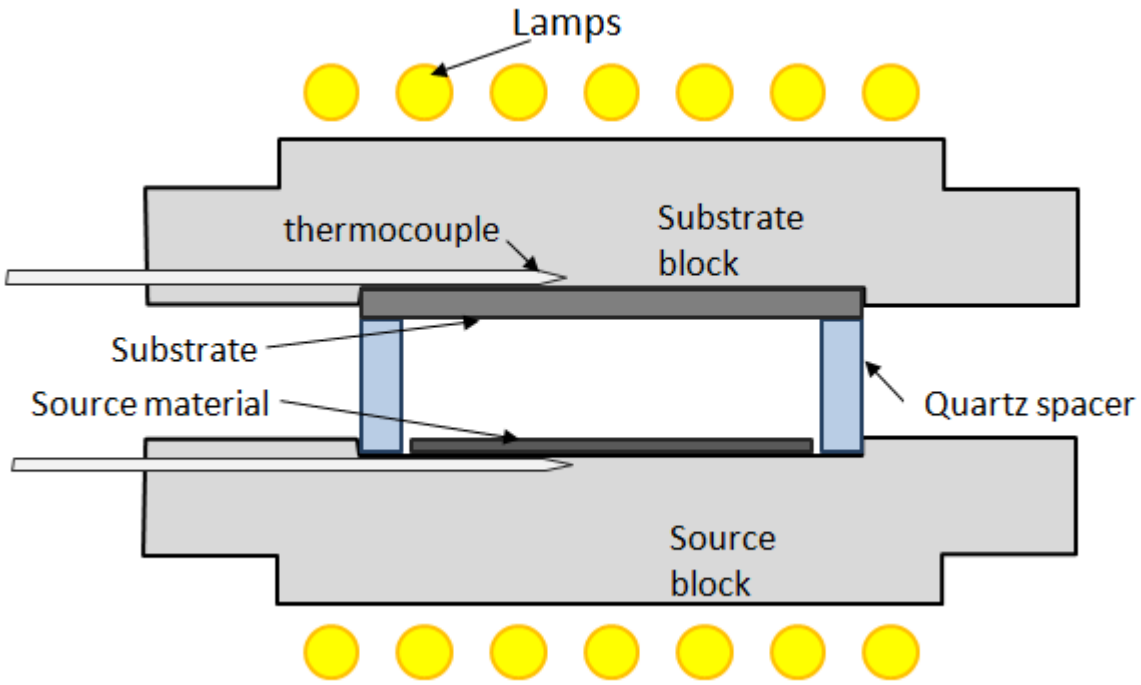

Figure 31: Schematic view of a CSS chamber

Once the three technologies are clear it's possible to define the annealing parameters:

- during annealing in the CVD chamber temperatures going from 360 to 800°C were used for times ranging from 10 to 30min. The chamber was kept at low pressure in hydrogen environment;
- annealing in CSS chamber was performed varying the bottom plate temperature between 0 and 315°C and top plate temperature between 500 and 600°C. If we define the annealing time as the time of holding at the mentioned temperatures, it ranges between nil (heating and immediate cooling) and 1min. Annealing was performed at 100torr in nitrogen gas environment;

- In annealing with RTA equipment, temperatures in the 500-700°C range were used for short times going from 15s to 1min. the chamber was kept at ambient pressure, 760torr, in nitrogen gas environment;

These thermal treatments were performed on some samples produced with solution for direct InP deposition, on In/rep phosphorus composite samples and on In/dropcasted red phosphorus samples.

2.7 OPTICAL CHARACTERIZATION

Samples showing the wanted composition from XRD and EDX analysis, i.e. samples with almost stoichiometric In/P ratio and giving InP signal in XRD, underwent optical characterization to verify the optical and semiconducting nature of the produced material. In this case optical characterization implied the determination of the material bandgap through photoluminescence (PL) and exciton lifetime through time resolved photoluminescence (TRPL).

Photoluminescence spectroscopy is a contactless, non-destructive method of probing the electronic structure of materials. Light is directed onto a sample, where it is absorbed and imparts excess energy into the material in a process called photo-excitation. One way this excess energy can be dissipated by the sample is through the emission of light, or luminescence. In the case of photo-excitation, this luminescence is called photoluminescence.

The intensity and spectral content of this photoluminescence is a direct measure of various important material properties. Photo-excitation causes electrons within the material to move into allowed excited states. When these electrons return to their equilibrium states, the excess energy may be released with emission of light (a radiative process) or may not (a non-radiative process). The energy of the emitted light (photoluminescence) relates to the difference in energy levels between the two electron states involved in the transition between the excited state and the equilibrium state. The intensity of the emitted light is related to the relative contribution of the radiative process. Since in semiconductors the electron decay will occur from the conduction to the valence band, this process can be used to determine the bandgap value of a semiconductor. This is useful both to characterize new materials and to determine the quality of a product, comparing the results obtained by the measure with those present in the literature. In our case PL was performed to verify the good quality of the deposited InP comparing the results with known values for bandgap.

TRPL is a contactless method to characterize recombination and transport in photovoltaic materials [46]. TRPL is measured by exciting luminescence from a sample with a pulsed light source, and then measuring the subsequent decay in photoluminescence (PL) as a function of time. A wide variety of experimental configurations can accomplish this. Most experiments excite the sample with a pulsed laser source, and detect the PL with a photodiode, streak camera, or photomultiplier tube (PMT). Trough TRPL exciton lifetime was measured for different samples and compared to that relative to a high quality evaporated InP sample. In this way an idea on the quality of the sample can bear, since lifetime is bound to defect density and proportional to sample purity and quality.

PL was performed using an HeNe laser at a wavelength of 632.8nm with a 5μm spot size.

The TRPL excitation source was a tunable Mira 900-F Ti-sapphire laser set to 800nm, different incident light power were used, ranging from 150mW to 400mW. The time between pulses was ~12ns.

.

Chapter 3

Experimental Results

In this chapter results relative to the performed experimentation are reported, results are organized as the experimental procedure. For each set of experiments only the most significant results are described.

3.1 DIRECT INDIUM PHOSPHIDE CODEPOSITION

Results are illustrated showing the characterizations performed and are organized depending on the plating bath used. All the samples were characterized with XRD, in Milan SEM was performed only on the promising samples while it was more used in Berkeley. PL and TRPL were performed only on samples for which compositional analysis gave satisfactory results.

3.1.1 Deposits based on Ni-P plating

As mentioned in the previous chapter a very broad range of solution compositions and deposition conditions was considered in this group of experiments, characterization is reported for some significant samples of which experimental conditions will be described.

As can be seen from XRD spectrum of sample E19 (*Fig.32*), no InP could be deposited from this kind of solutions at room temperature. Sample was produced in the following conditions:

- Solution: 1.5mM $InCl_3$, 50mM H_3PO_3, 25mM NaH_2PO_2;
- Deposition conditions: t=25min, T=25°C, i=-10mA/cm^2;

It's possible to recognize peaks for iron and for indium, iron peaks are relative to the AISI 304 substrate while In peaks are relative to the deposit. Other depositions changing current density, namely at -5 and -30mA/cm^2, were performed under the same conditions and gave similar results from XRD analysis, resulting in In signal from the deposit and iron signal from the substrate.

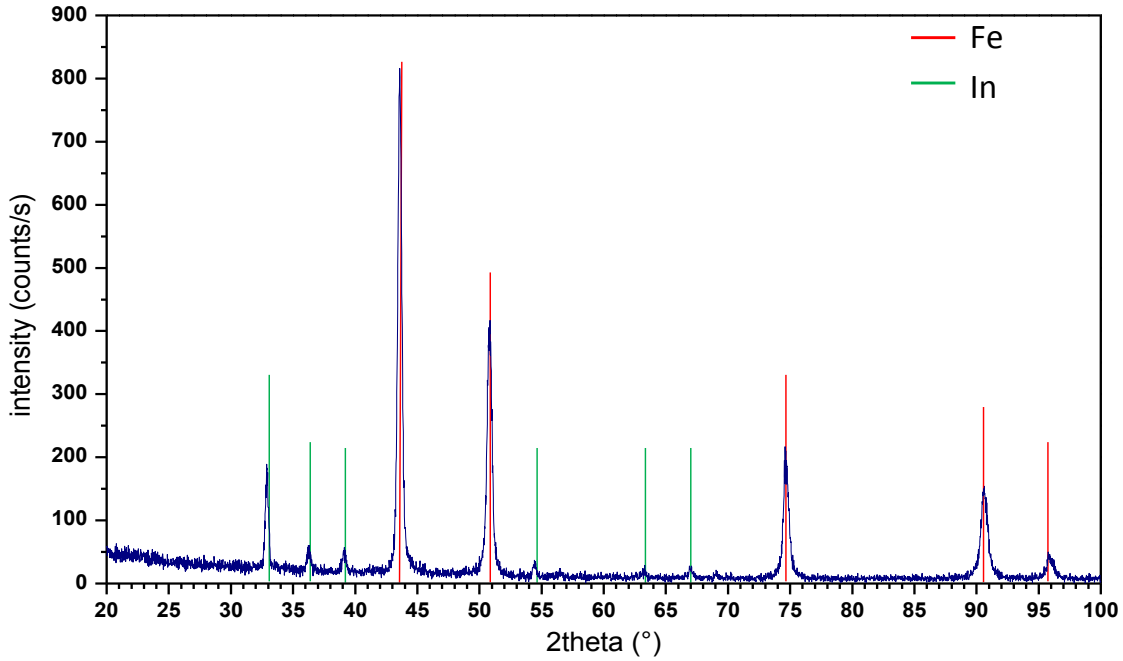

Figure 32: XRD pattern for sample E19

Even changing solution composition and deposition conditions, as for sample E24, the XRD pattern (*Fig.33)* doesn't show any marked modification. Sample E24 was deposited at higher temperature with the idea of activating sodium hypophosphite reactions, the deposition was performed in the following conditions:

- Solution: 1.5mM $InCl_3$, 30mM H_3PO_3, 30mM NaH_2PO_2, 17.5mM H_3PO_4;
- Deposition conditions: =30min, T=85°C, i=-10mA/cm^2;

Even in this case depositions were performed in the same conditions, for different current density values.

The XRD pattern just highlights the presence of In and Fe.

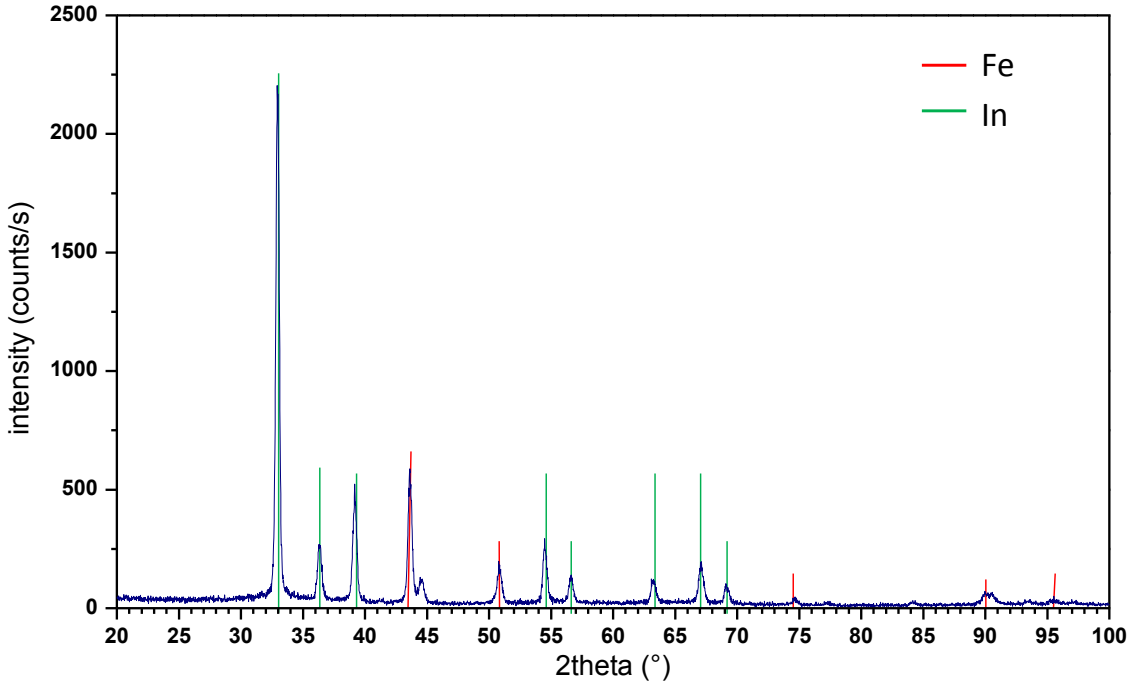

Figure 33: XRD pattern for sample E24

The XRD patterns reported here represent just a small portion of the quantity of samples produced with this type of solution. These particular samples were selected as representative, in order to give an idea of the results obtained, since all the experiments led qualitatively to the same XRD patterns.

On some samples produced in Berkeley after XRD characterization also SEM imaging with EDX elemental analysis was performed. Sample B9 is an example, this was produced in the following conditions:

- Solution: 100mM $InCl_3$, 2M H_3PO_4, 100mM NaH_2PO_2
- Deposition conditions: t=50min, T=60°C, i=-15mA/cm^2

XRD pattern for this sample is reported in *Fig.34*, this deposition was performed on commercial molybdenum foil. Sample B9 at visual inspection didn't appear silvery white as the other samples that revealed to be pure indium, it had light grey coloration. This was confirmed by EDX elemental analysis associated with SEM imaging (*Fig.35*), that showed incorporation of a high quantity phosphorus in the deposit with P/In ratio was almost 0.8. For this reason thermal treatments were performed on this sample.

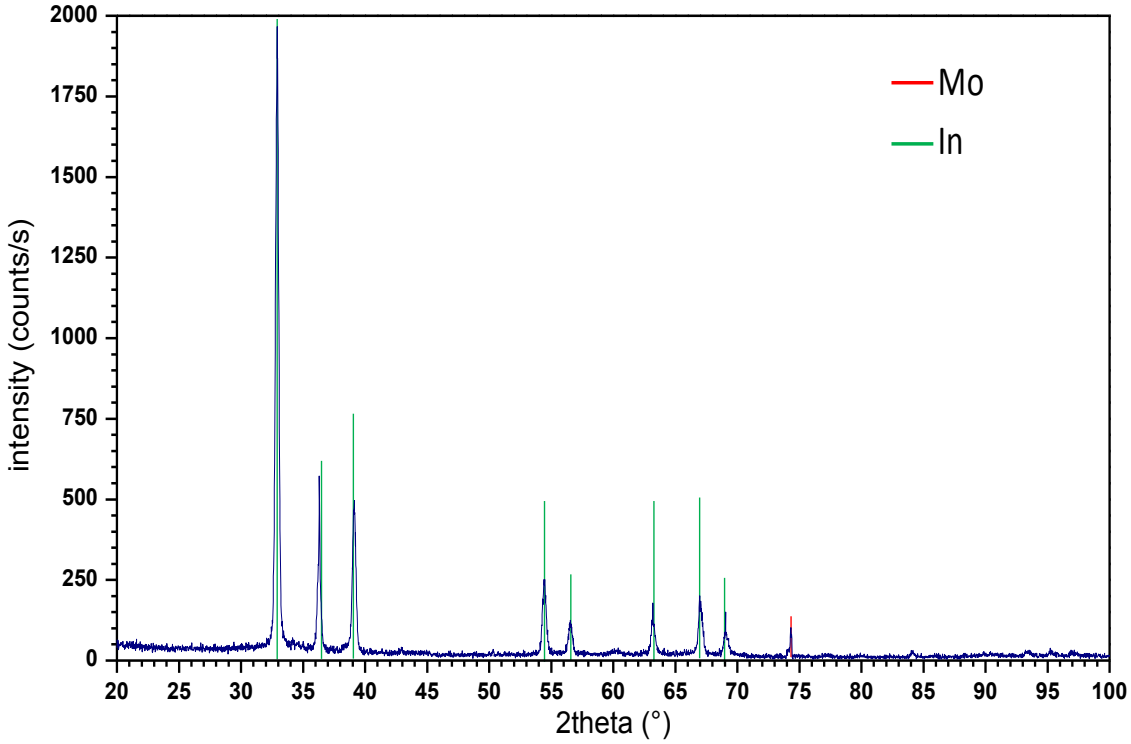

Figure 34: XRD pattern for sample B9 before annealing

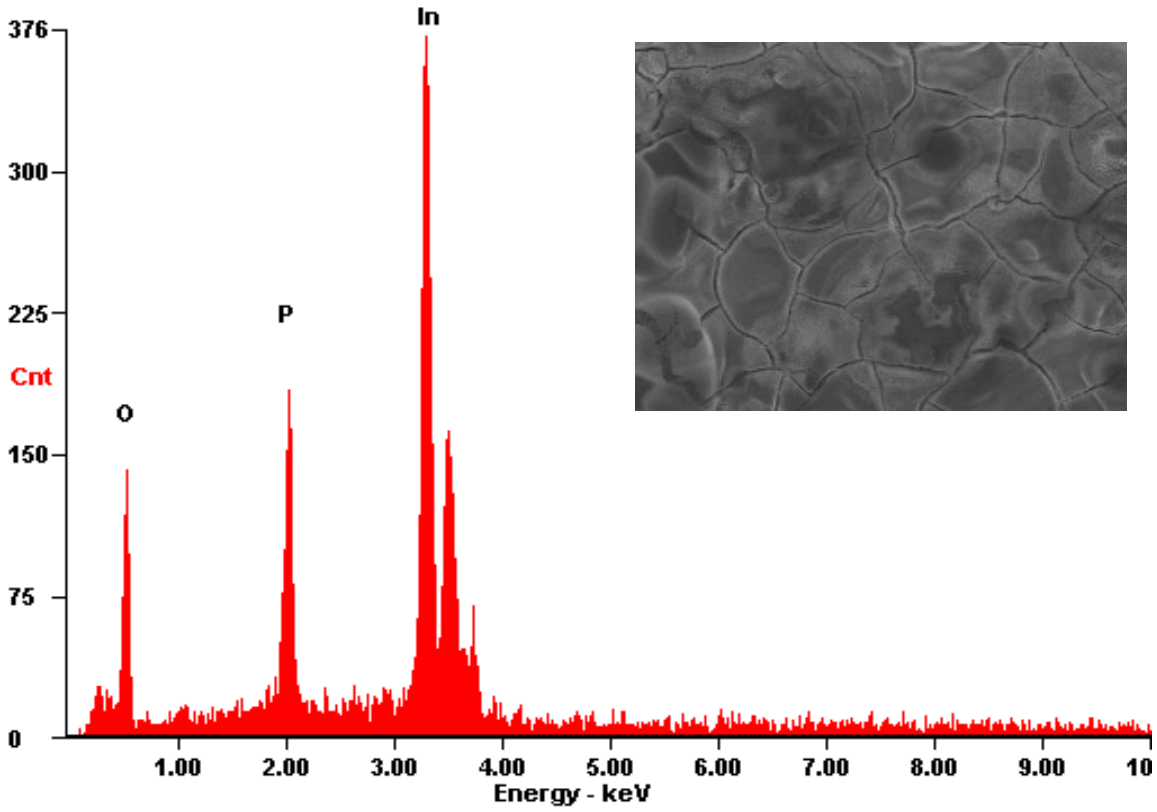

Figure 35: EDX spectrum for sample B9 with SEM image of the investigated area before annealing

Elemental mapping was performed on sample B9 before annealing and after annealing (*Fig.36*).

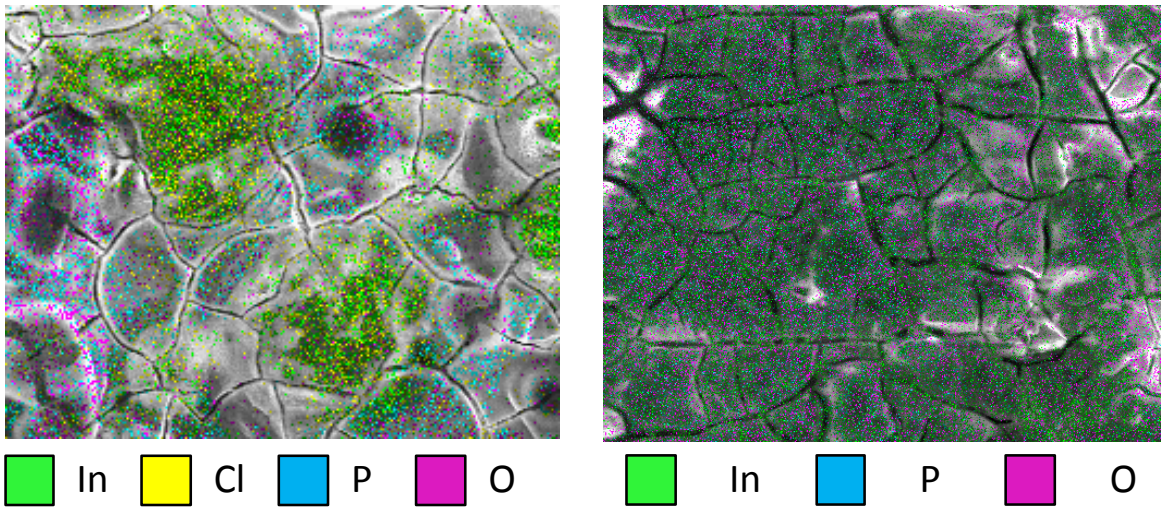

Figure 36: SEM image with elemental mapping on sample B9 before(left) and after annealing(right)

Before annealing a 100nm SiN cap was performed at 100°C using PECVD. Annealing was performed in the following conditions:

- Under vacuum
- H_2 Atmosphere 50 sccm (standard cubic centimetre per minute)
- 360°C for 30min
- Cooled to ambient rapidly

The resulting XRD spectrum after annealing is reported in *Fig.37*.

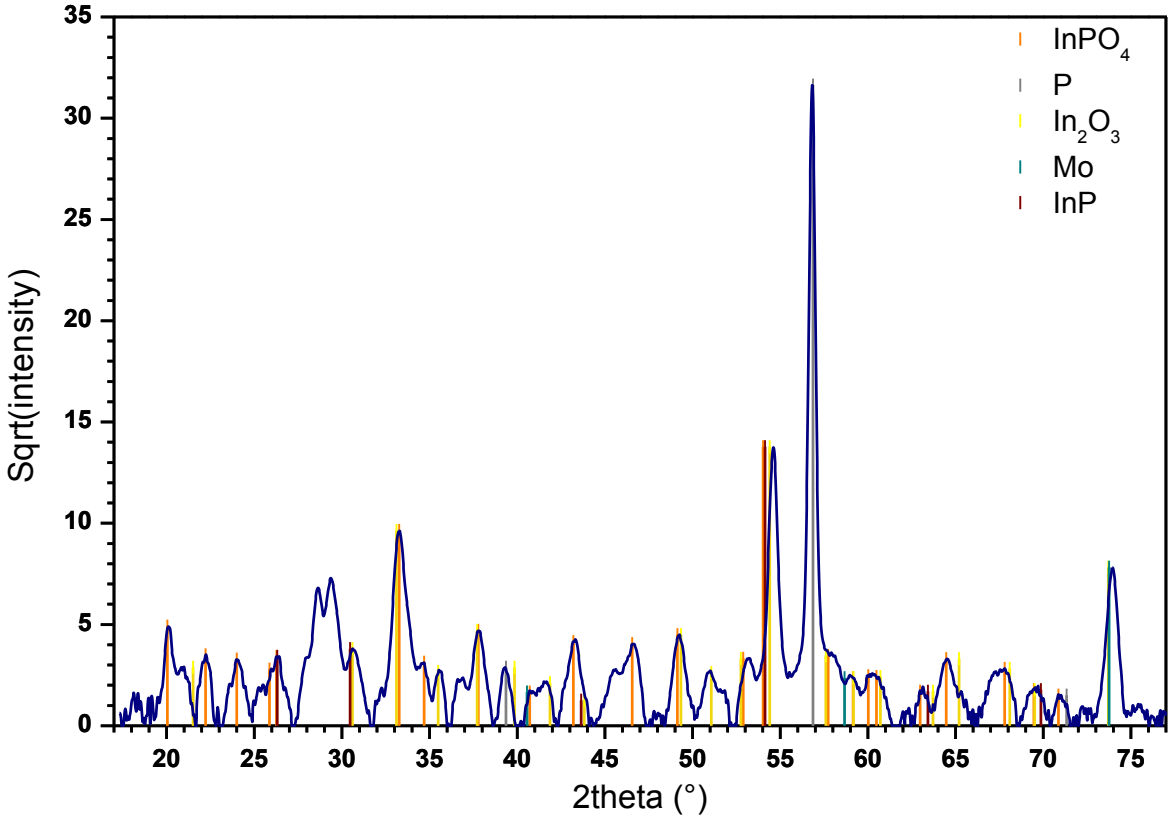

Figure 37: XRD spectrum for sample B9 after annealing

PL was performed on the sample after annealing, the results are reported in *Fig.38.*

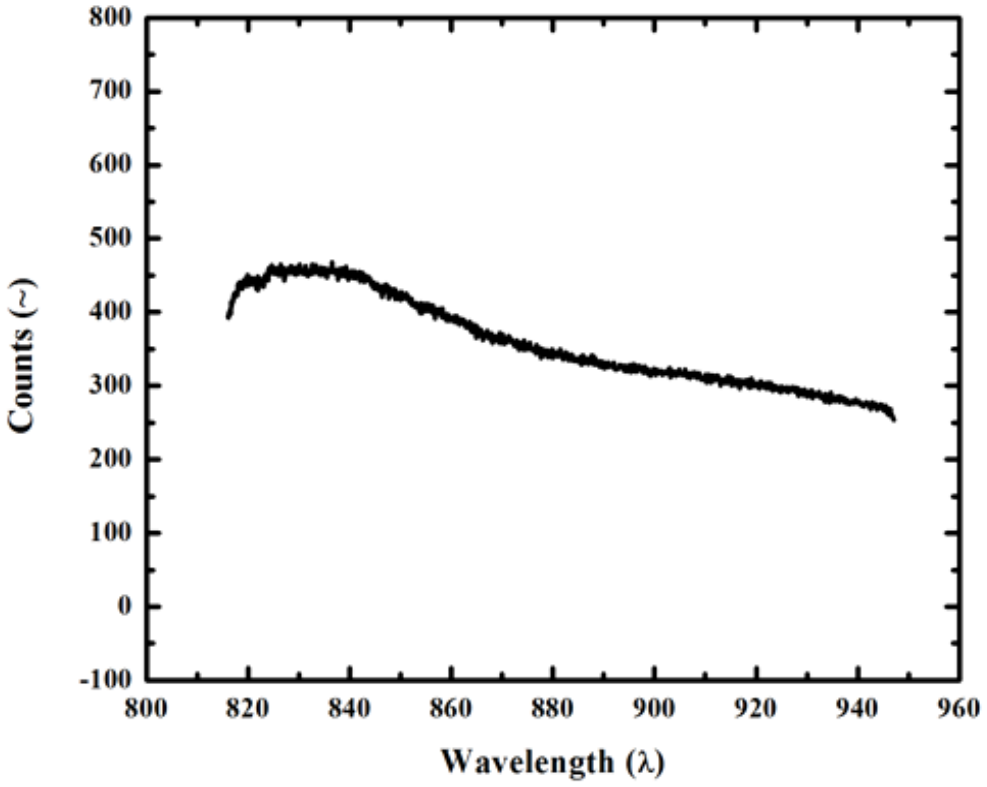

Figure 38: PL spectrum for sample B9 after annealing

3.1.2 Deposits produced with complexing agents

Complexing agents were used together with precursors employed in solutions inspired to Ni-P, the chemicals used are mentioned in the previous chapter. Results for some of the samples produced are reported below.

Fig.39 shows XRD pattern for sample E41, this was produced in the following conditions:

- Solution: 230mM $InCl_3$, 26mM H_3PO_3, 26mM H_3PO_4, 267mM H_3NO_4S, 2%w TEA;
- Deposition conditions: t=10min, T=50°C, i=-10mA/cm^2;

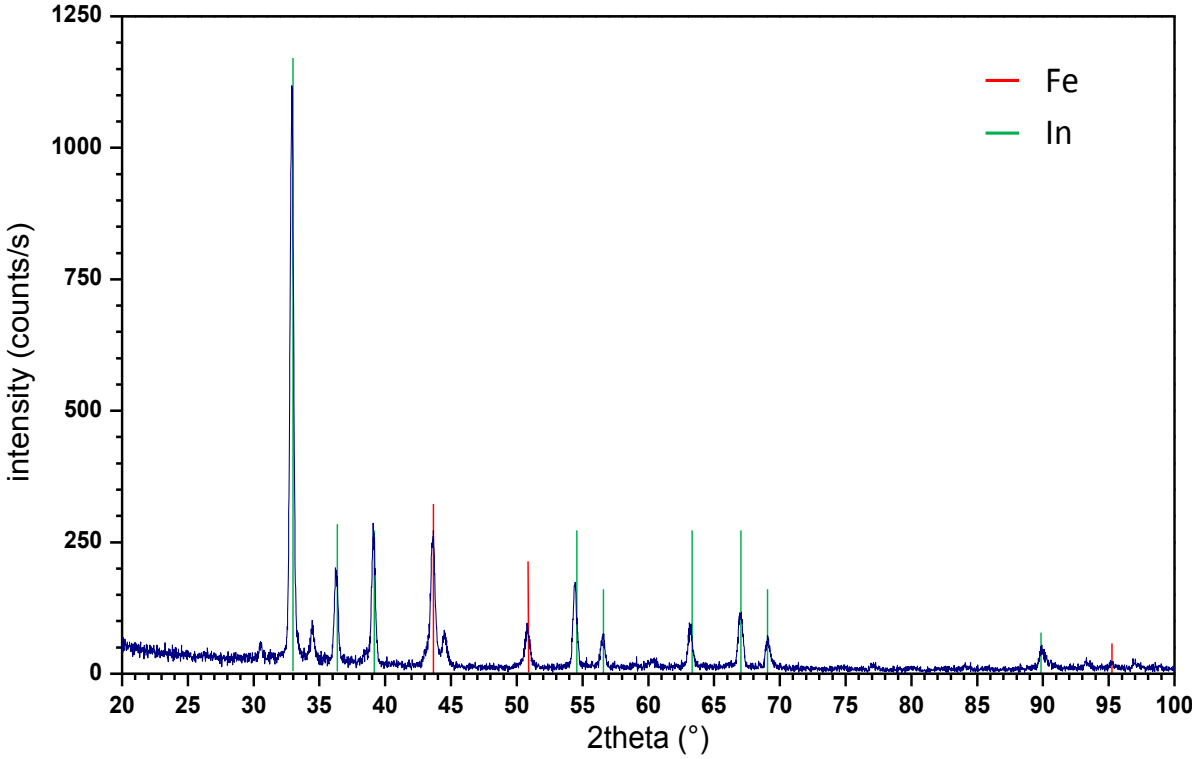

Figure 39: XRD pattern for sample E41

E41 was deposited on AISI 304, after XRD also SEM with EDX was performed on the sample to verify the elemental composition, *Fig.40.*

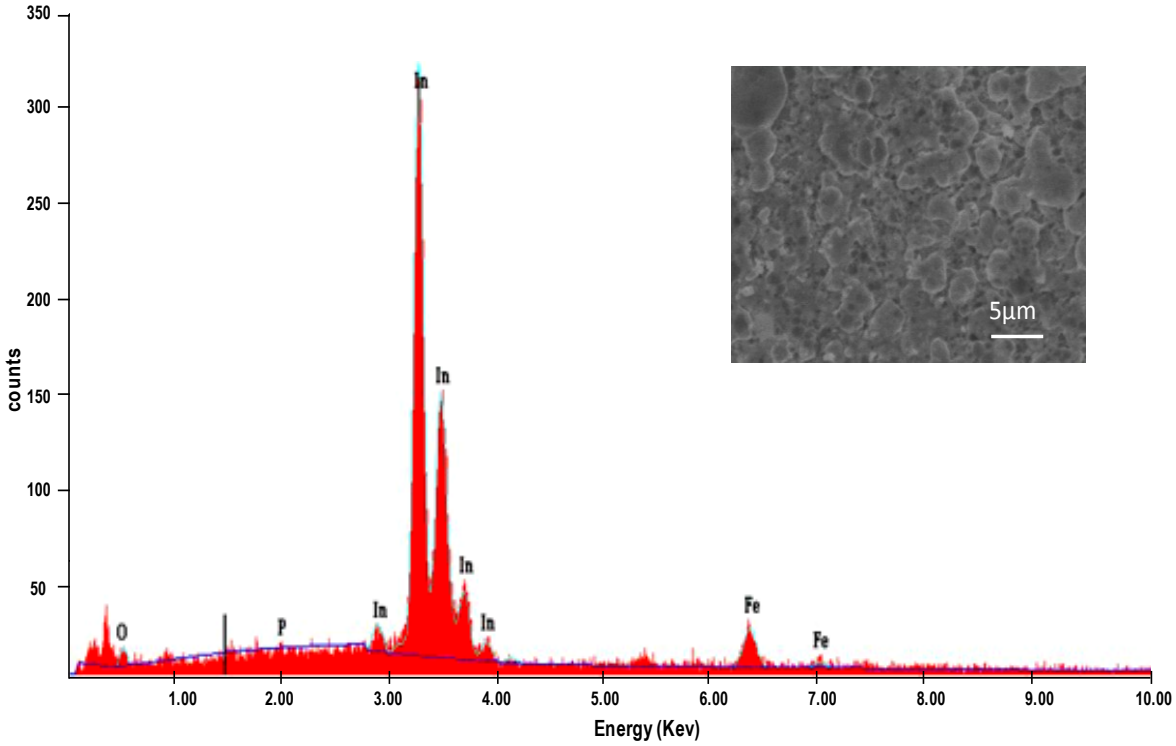

Figure 40: EDX analysis for sample E41with SEM image of the investigated area

Other samples were produced changing complexing agents and phosphorus precursors, sample E45 was produced in the following conditions:

- Solution: 100mM $InCl_3$, 200mM H_3PO_4, 200mM NaH_2PO_2
  150mM citric acid, 350mM Na citrate, 14%w EDTA
- Deposition conditions: t=20min, T=90°C, i=-20mA/cm^2

For this sample AISI304 was used as substrate, *Fig.41* shows the XRD spectrum for the deposit E45.

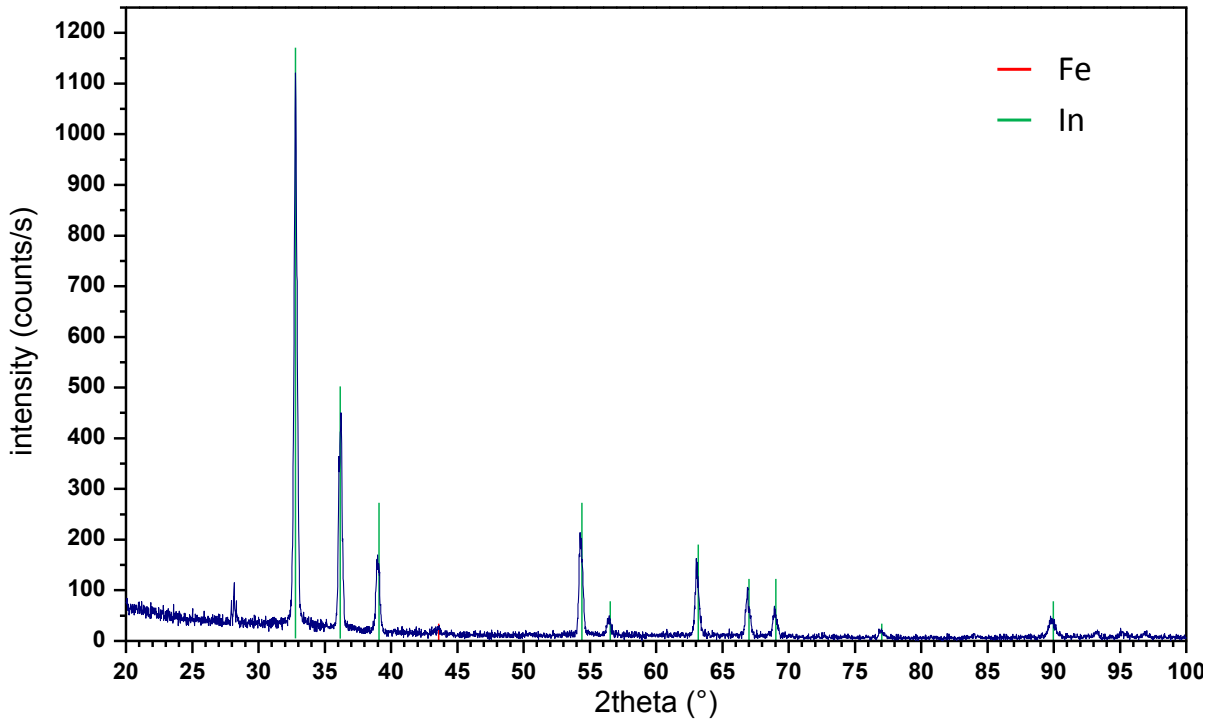

Figure 41: XRD pattern for sample E45

Fig.42 shows EDX spectrum for sample E45.

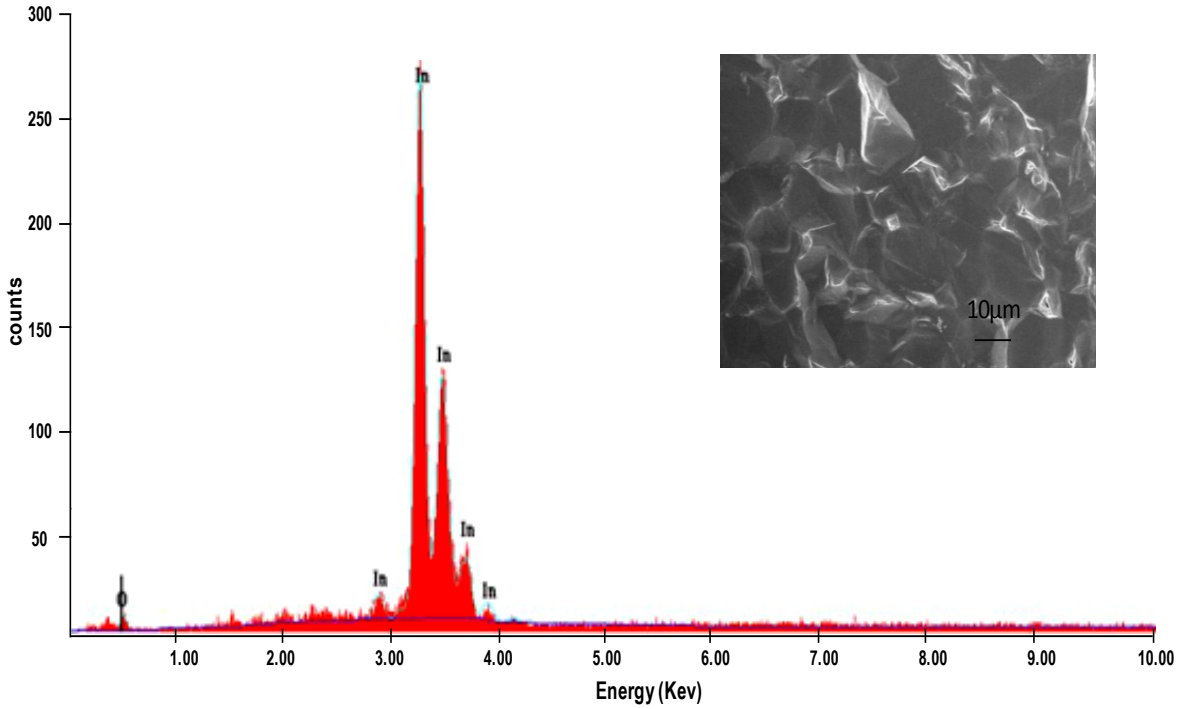

Figure 42: EDX of sample E45 with SEM image of the investigated area

3.1.3 Deposits based on Sahu's works

Results are presented relative to samples produced with solutions and experimental conditions inspired to Sahu's publications. *Fig.43* shows the XRD spectrum for sample A1.

This was produced in the following conditions, using commercial Ti foil as substrate:

- Solution: 12.5mM $InCl_3$, 583mM NH_4PF_6;
- Deposition conditions: t=15min, T=25°C, i=-20mA/cm^2;

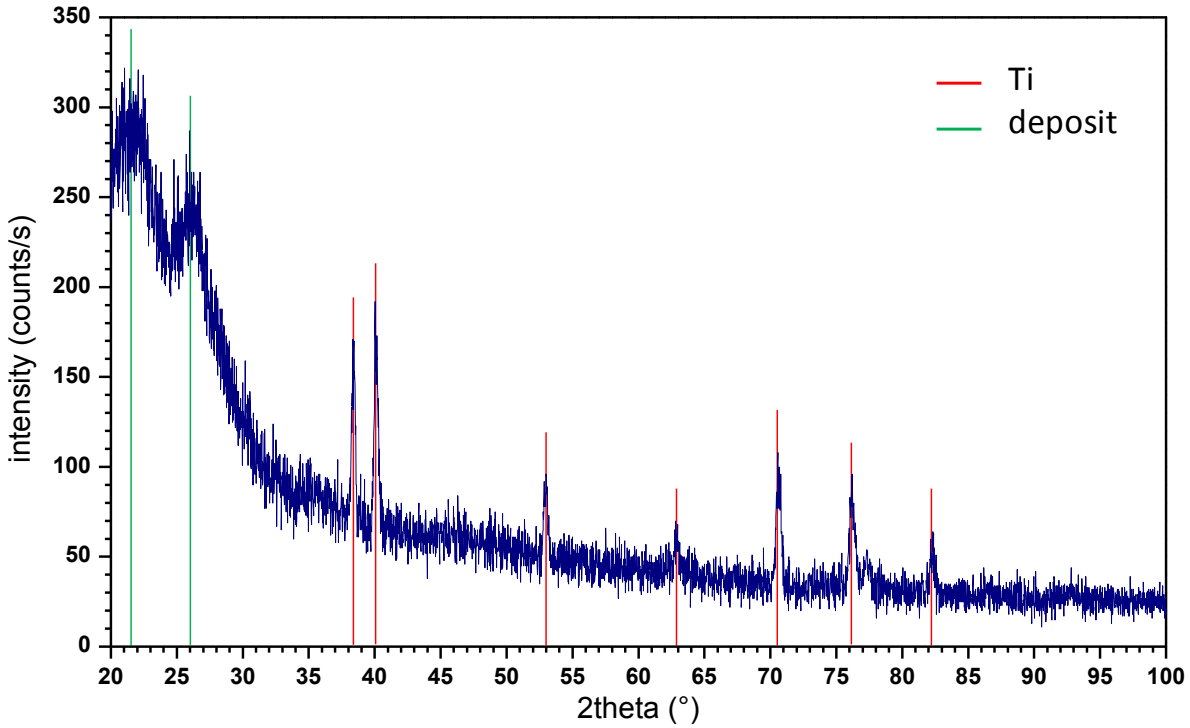

Figure 43: XRD pattern for sample A1

SEM imaging with EDX analysis was performed on sample A1, surface image is reported in *Fig.44*.

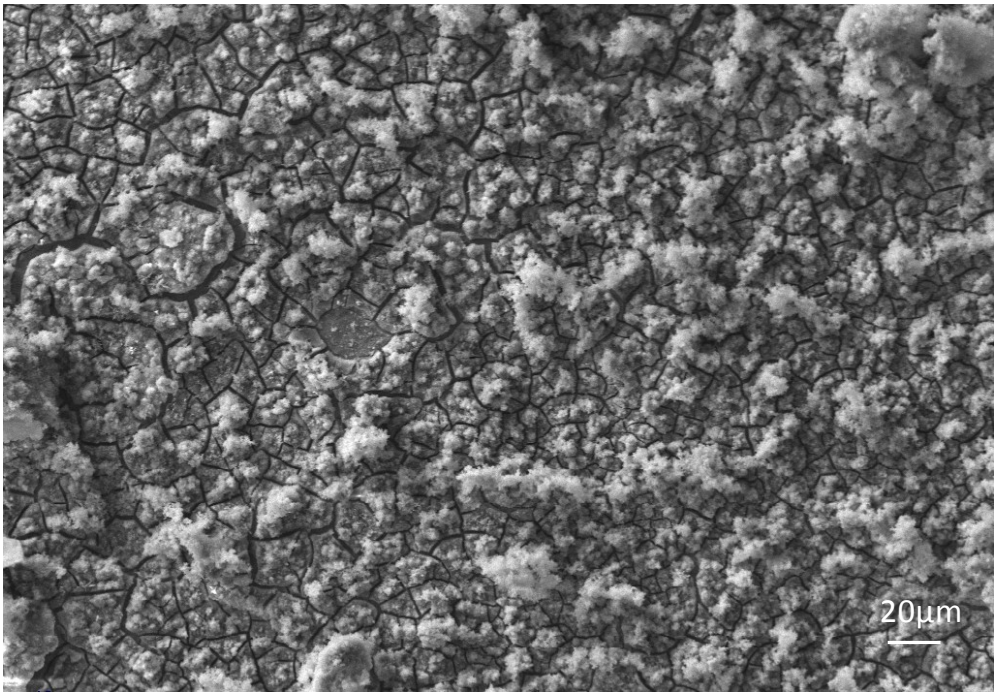

Figure 44: SEM image of the surface of sample A1

EDX analysis reports that the sample is composed by In and P respectively at 75% and 25% in weight, that converted in atomic percent gives In 44%at and P 56%at. Subsequently samples were cleaned to remove the superficial, not adherent, layer and characterization was repeated. SEM imaging is reported in *Fig.45*.

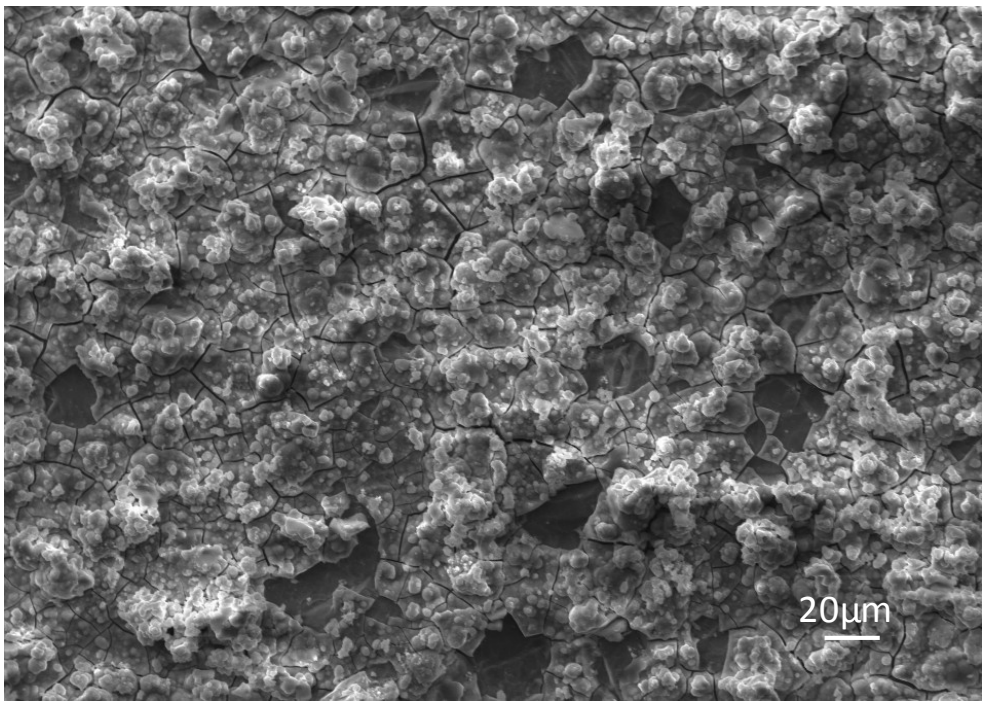

Figure 45: SEM image of sample A1 after cleaning

EDX (*Fig.46*) analysis after cleaning revealed presence of high amounts of oxygen and some fluoride besides In and P: the composition in atomic percent reveals In 8.48%at, P 10.17%at, F 6.34%at and O 75%at. Moreover if we consider just indium and phosphorus the composition is unchanged: In 45%at and P 55%at.

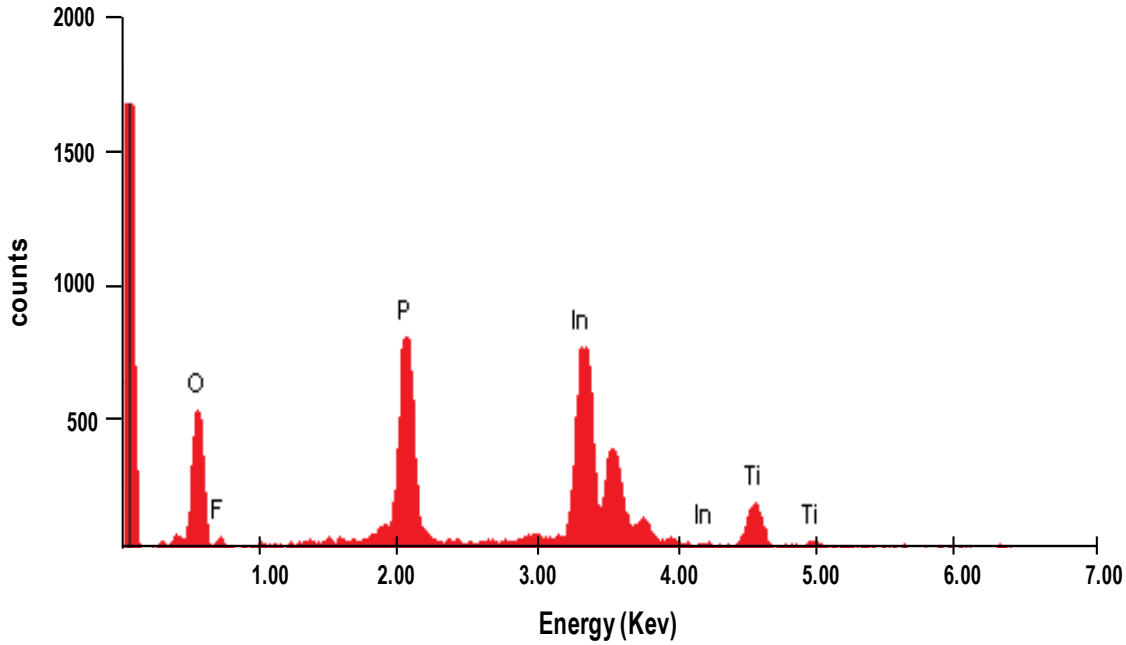

Figure 46: EDX spectrum for sample A1 after cleaning

3.1.4 Deposits with alcoholic solutions

Solutions based on Ni-P plating were added with alcohols with the idea of stabilizing ionic species of indium hydroxide in solution. Results are reported below.

Fig.47 shows XRD for sample B76, this was deposited on molybdenum in the following conditions:

- Solution: 20mM $InCl_3$, 20mM H_3P0_3, 20%vol IPA
- Deposition conditions: t=60min, T=25°C, i=-15mA/cm^2

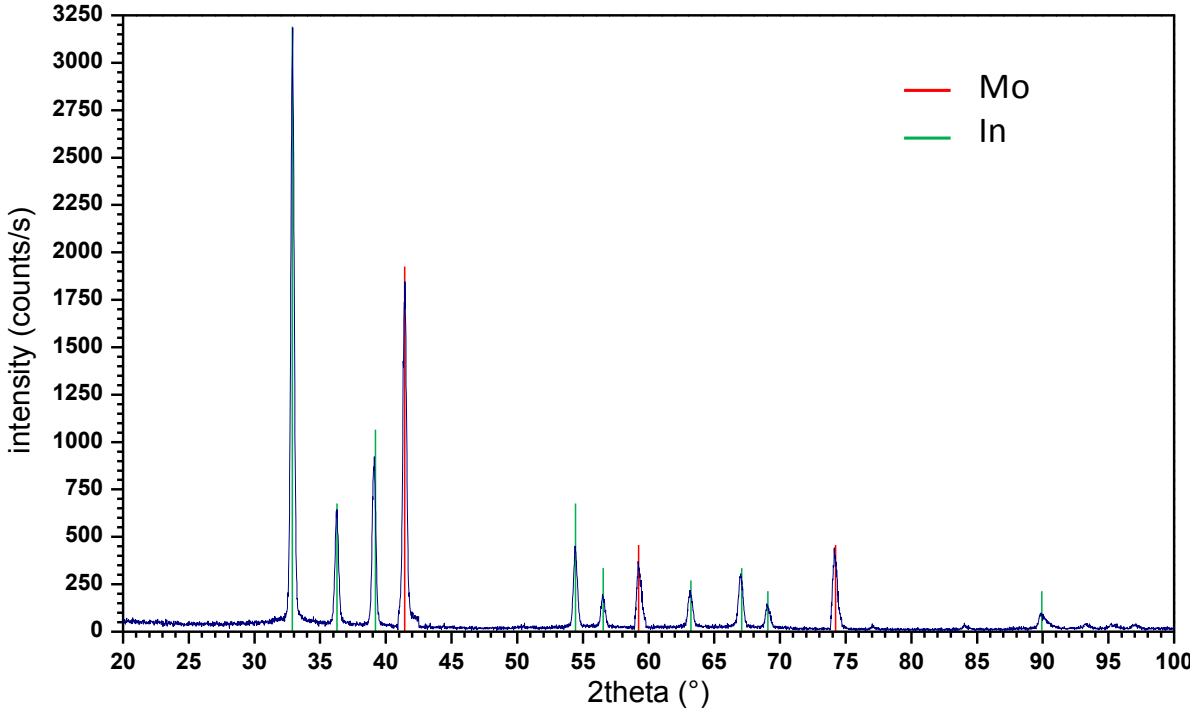

Figure 47: XRD spectrum for sample B76

EDX spectrum for sample B76 is shown in *Fig.48.*

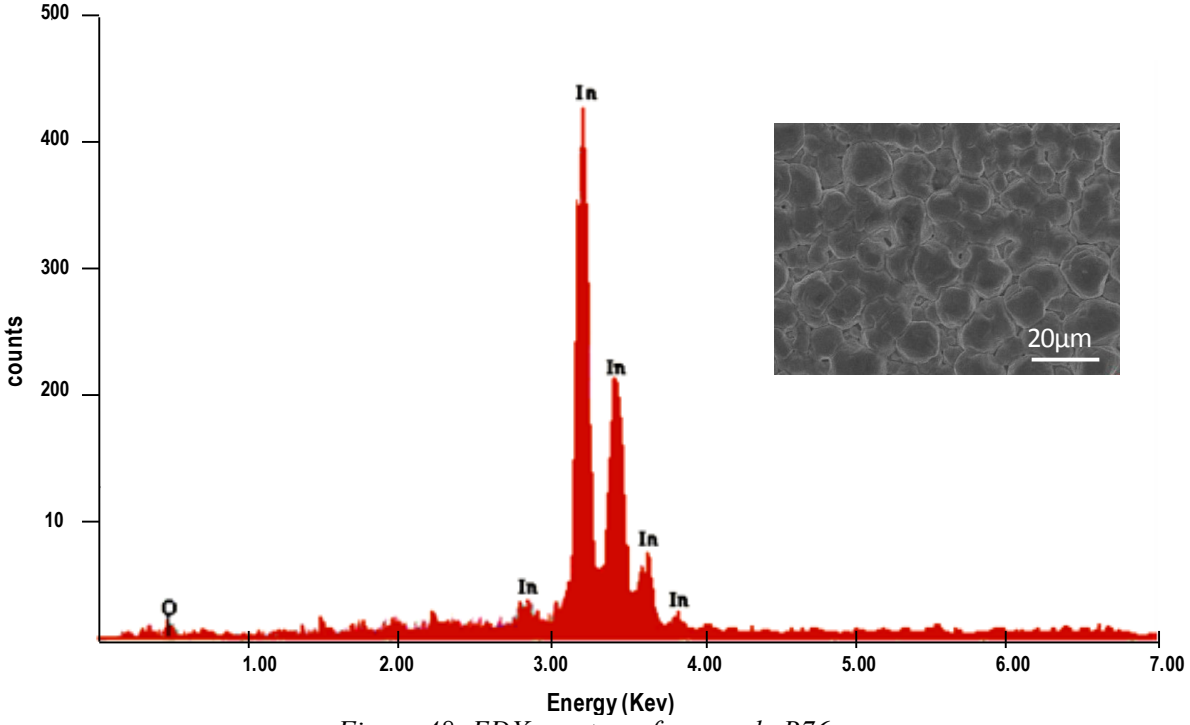

Figure 48: EDX spectrum for sample B76

The same results were obtained using methanol as alcoholic addition to the solution. An example is sample B80, XRD results for this sample are shown in *Fig.49.* This sample was produced under the following conditions:

- Solution: 50mM $InCl_3$, 30mM H_3P0_3, 30%vol methanol
- Deposition conditions: t=60min, T=25°C, i=-10mA/cm^2

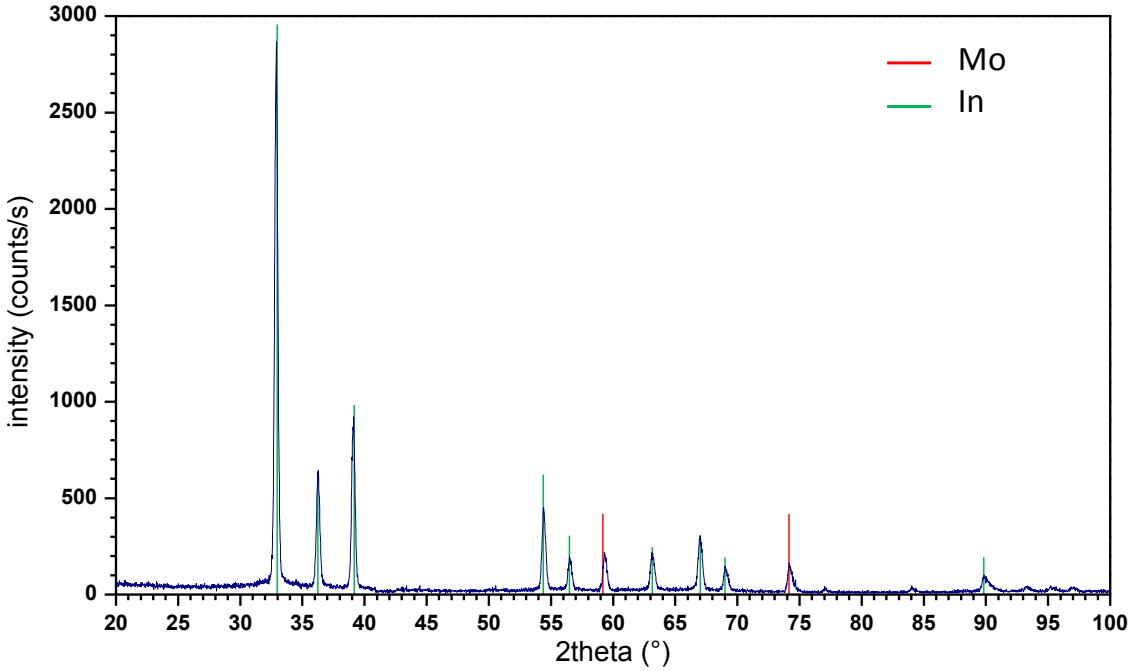

Figure 49: XRD pattern for sample B80

3.2 INDIUM AND RED PHOSPHORUS COMPOSITE DEPOSITION

All the samples with an adequate quantity of phosphorus incorporated in the deposit underwent thermal treatments, therefore characterization is reported before and after thermal treatment for the samples chosen as noteworthy.

Sample B72 was produced with the one-step deposition presented in chapter 2, the deposition conditions are the following:

- Solution: 100mM $In_2(SO_4)_3$, P_{red} powder 3g/L
- Deposition conditions: t= 30min, T= 25°C, i=-20mA/cm^2

Deposition was performed on a commercial molybdenum foil and XRD pattern before annealing is presented in *Fig.50*.

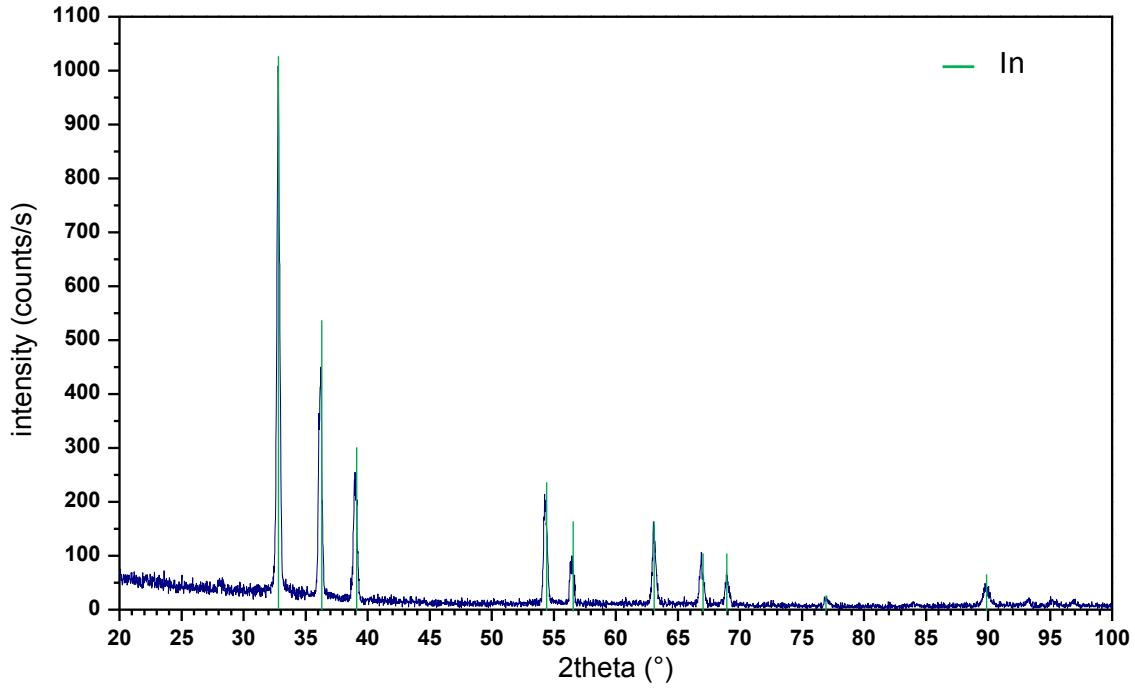

Figure 50: XRD pattern for sample B72 before annealing

Sample B72 was then capped with 500nm of e-beam evaporated SiO_2 and divided into 4 equivalent pieces. Each of them underwent one of the thermal treatments reported in *Table 3.1*.

Table 3.1

Sample	Chamber	Temperature (°C)	Time (s)	Environment	Pressure (torr)
B72a	RTA	700	15	N_2	760
B72b	RTA	700	30	N_2	760
B72c	RTA	700	60	N_2	760
B72d	CVD	700	600	H_2	10^{-1}

For each of the four pieces, after thermal treatment, SEM imaging with EDX elemental analysis was performed, *Fig.51* shows EDX pattern after the 15s RTA treatment.

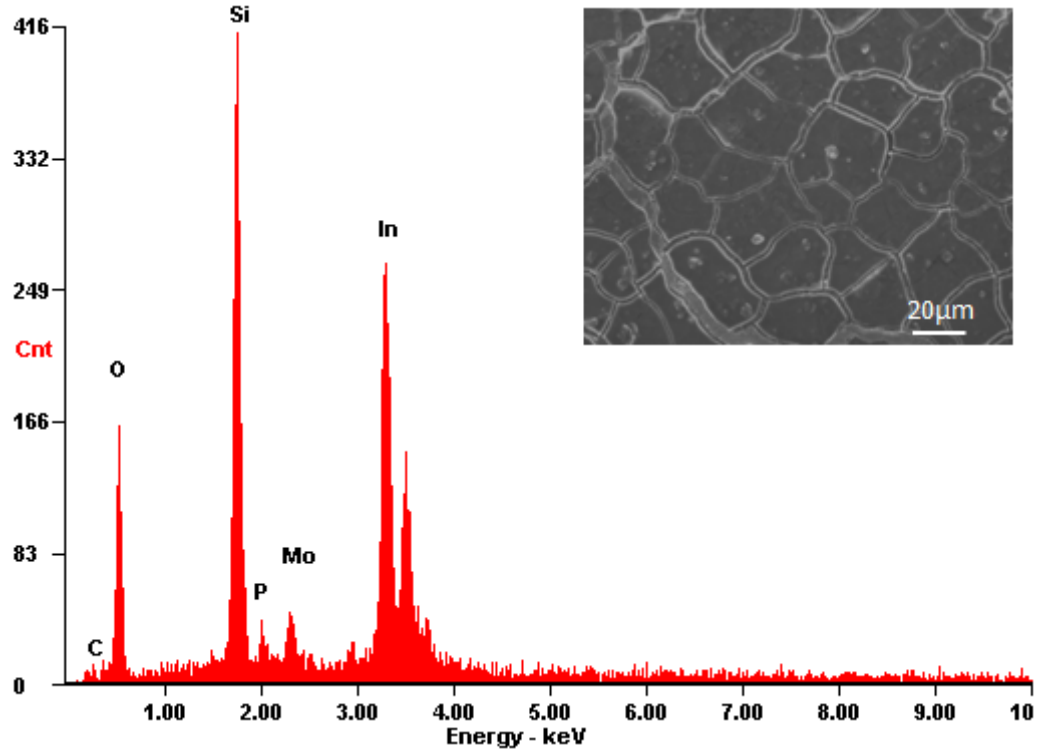

Figure 51: EDX pattern for sample B72a after 15s RTA and SEM image of the investigated area

After annealing 5%HF etching was performed for 1min to remove the silicon dioxide cap, the resulting EDX analysis is reported in *Fig.52.*

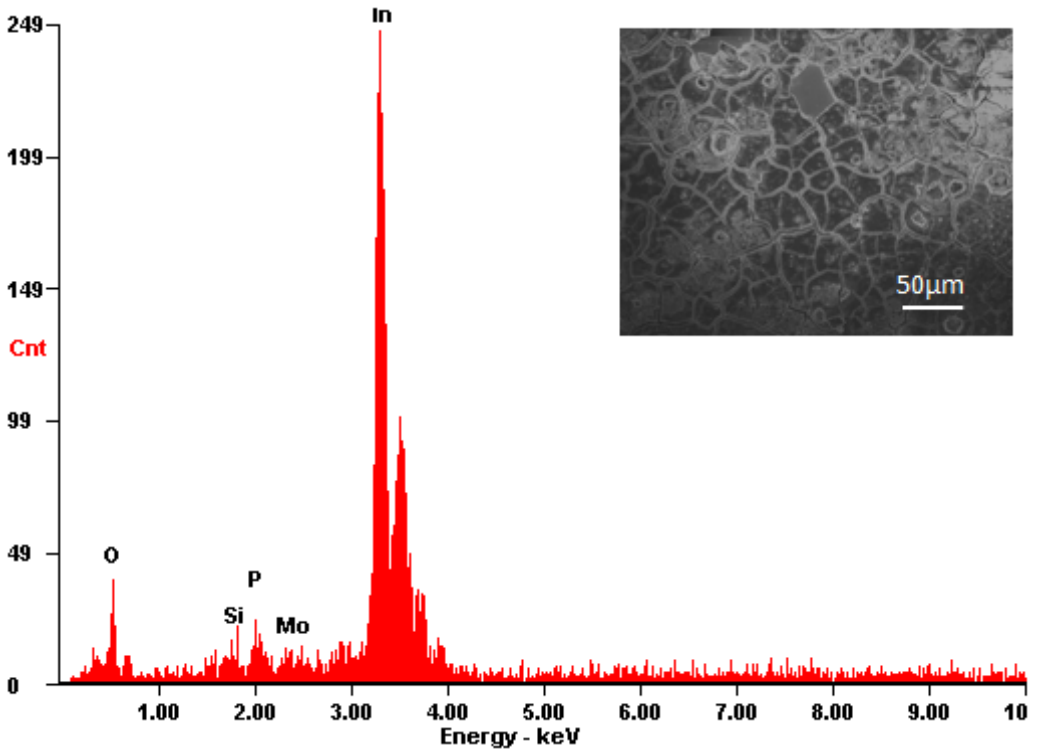

Figure 52: EDX pattern for sample B72.a after HF etch and SEM image of the investigated area

Fig.53 shows EXD analysis results with SEM image of the investigated area, for sample B72c after annealing.

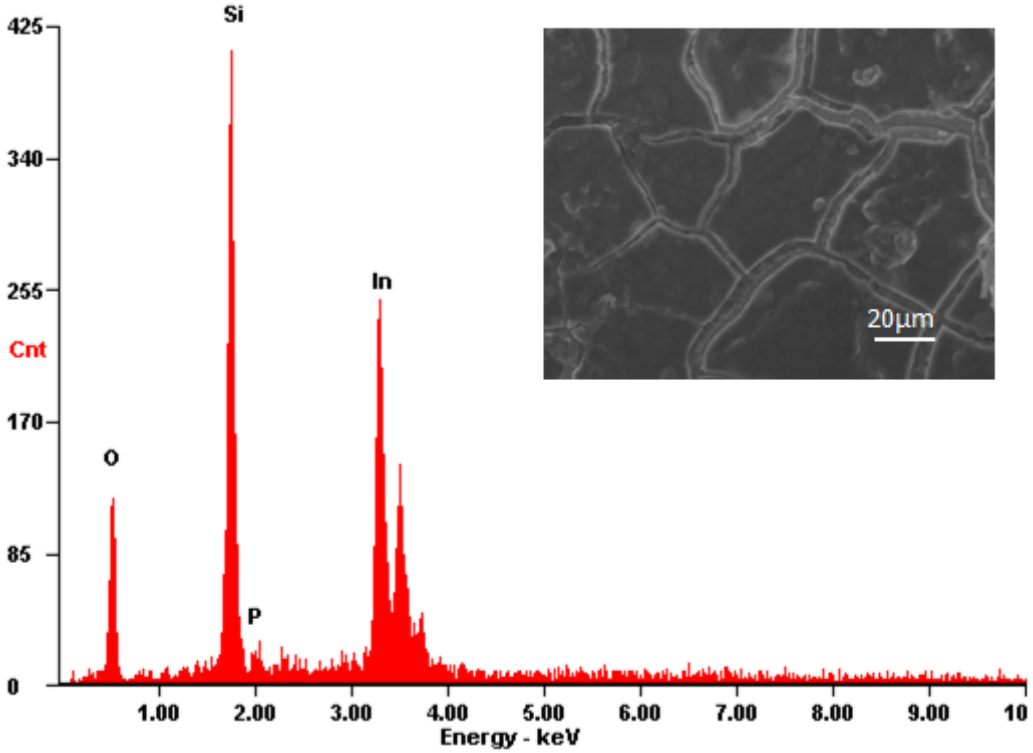

Figure 53: EDX pattern for sample B72c after 60s RTA and SEM image of the investigated area

Fig.54 shows EDX pattern for sample B72c after 10%HF etch for 1min.

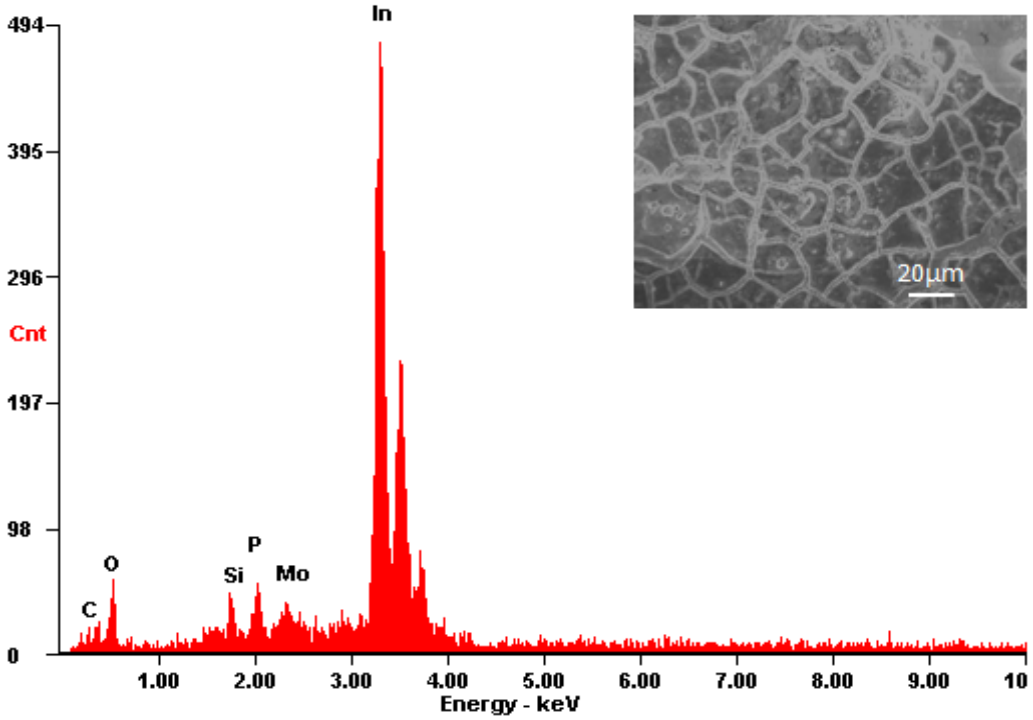

Figure 54: EDX pattern for sample B72c after HF etch and SEM image of the investigated area

Fig.55 shows EDX pattern for sample B72d after annealing in the CVD chamber.

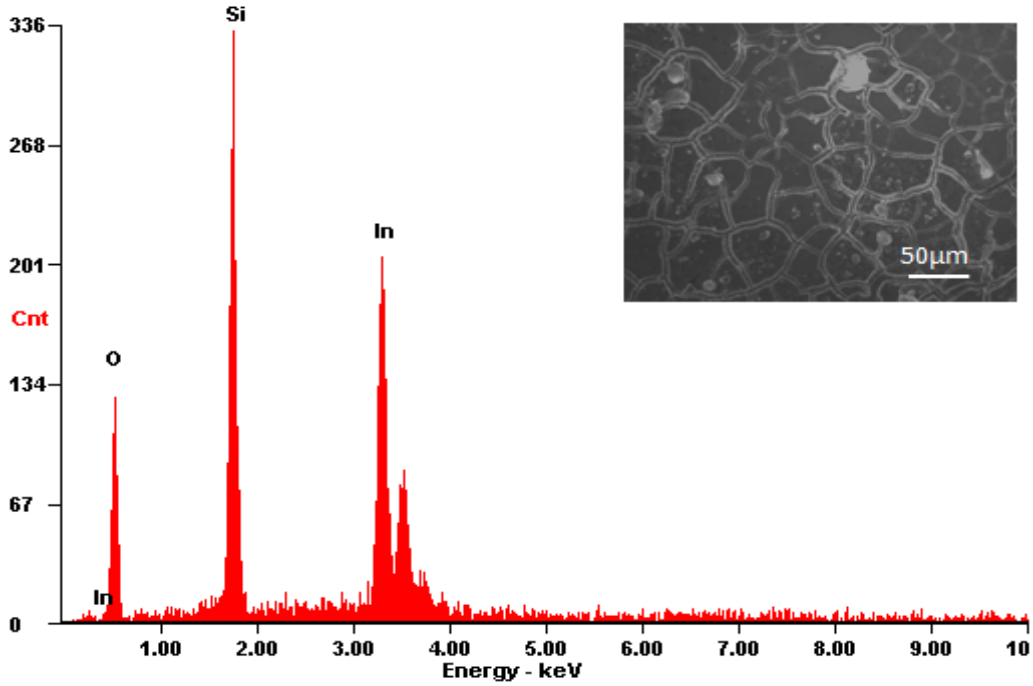

Figure 55: EDX pattern for sample B72 after CVD annealing and SEM image of the investigated area

Sample B90 was produced with the two-step deposition presented in chapter 2, the deposition conditions for the first step were the following:

- Solution: 50mM $In_2(SO_4)_3$,
- Deposition conditions: t= 30min, T= 65°C, i=-16,3mA/cm^2

For the second step conditions were:

- Solution: 100mM $In_2(SO_4)_3$, P_{red} powder 50g/L
- Deposition conditions: t= 30min, T= 25°C, i=-20mA/cm^2

XRD analysis was performed after deposition, giving the results reported in *Fig.56.*

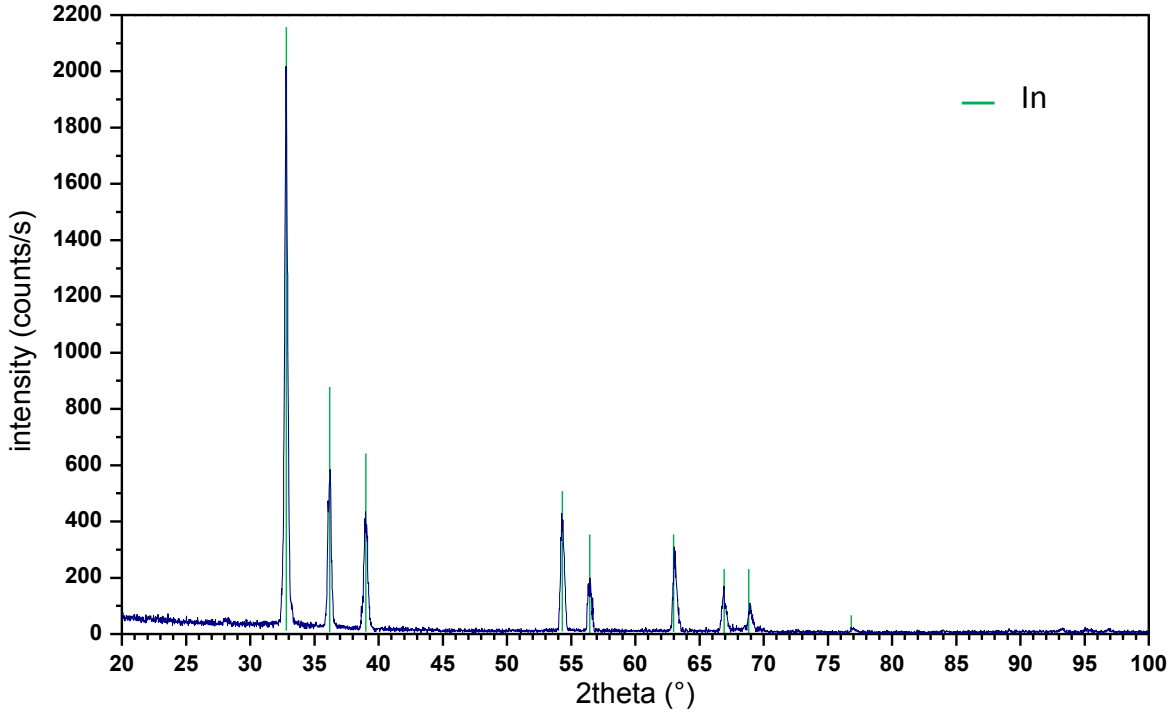

Figure 56: XRD spectrum for sample B90 before thermal treatments

After the two-step deposition sample was capped with a 1µm SiO_2 e-beam evaporated layer. Subsequently thermal treatments were performed, also this sample was divided into several parts and underwent different thermal treatments, just the most interesting results are reported.

Annealing conditions are reported in *Table 3.2*.

Table 3.2

Sample	Chamber	Top T(°C)	Bottom T (°C)	Environment	Pressure (torr)
B90a	CSS	0	500	N_2	300
B90b	CSS	315	500	N_2	300

XRD for sample B90b after annealing is represented in *Fig.57*.

Fig.58 reports EDX analysis for the same sample.

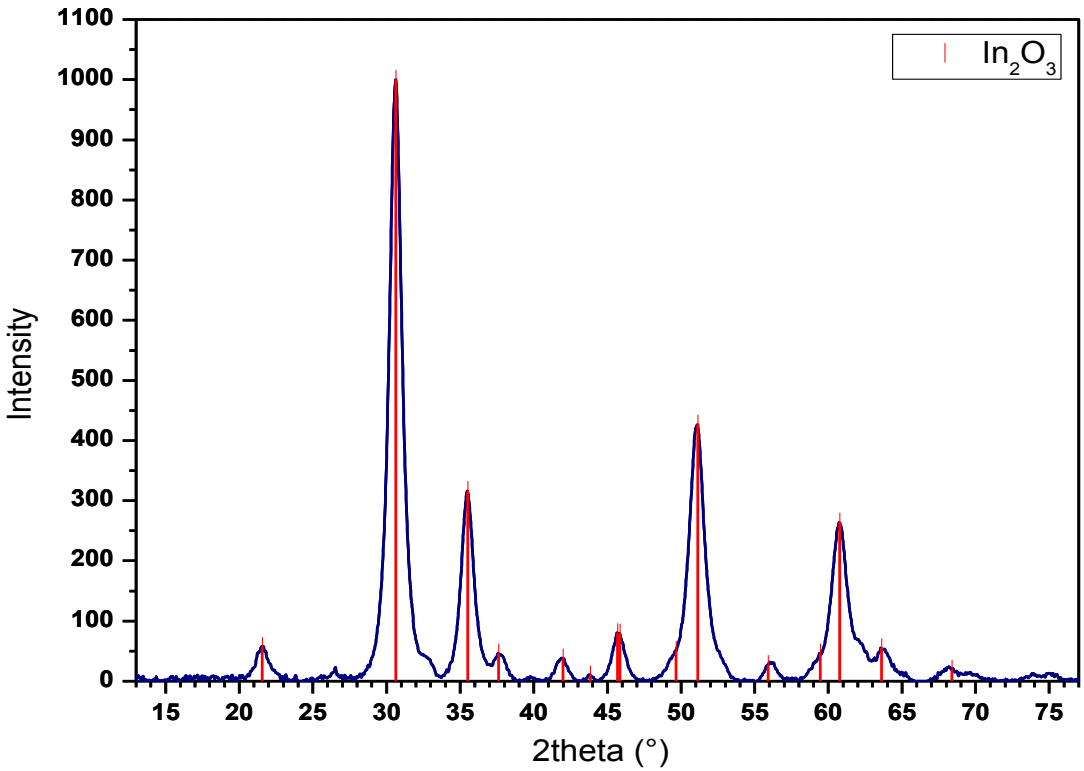

Figure 57: XRD spectrum for sample B90b after thermal treatments

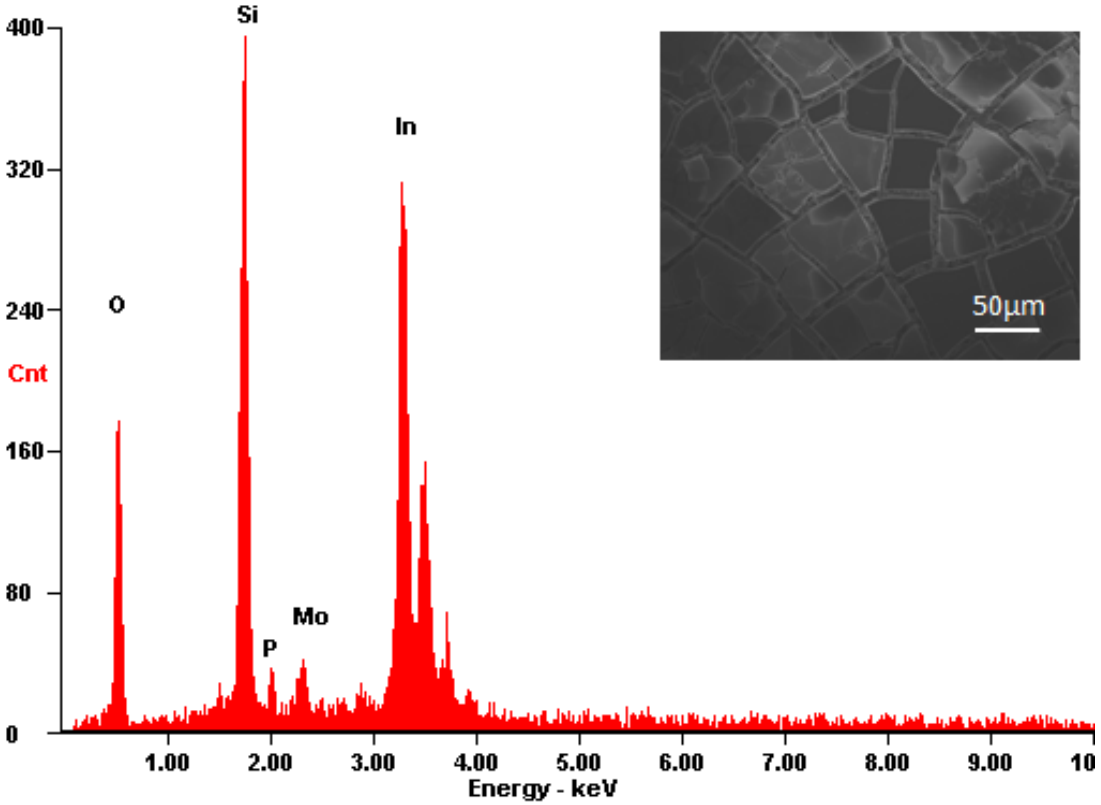

Figure 58: EDX spectrum for sample B90b after annealing and SEM image of the investigated area

In *Fig.59* EDX spectrum is reported for a local measure performed on sample B90b, the red rectangle highlights the area analyzed during EDX analysis.

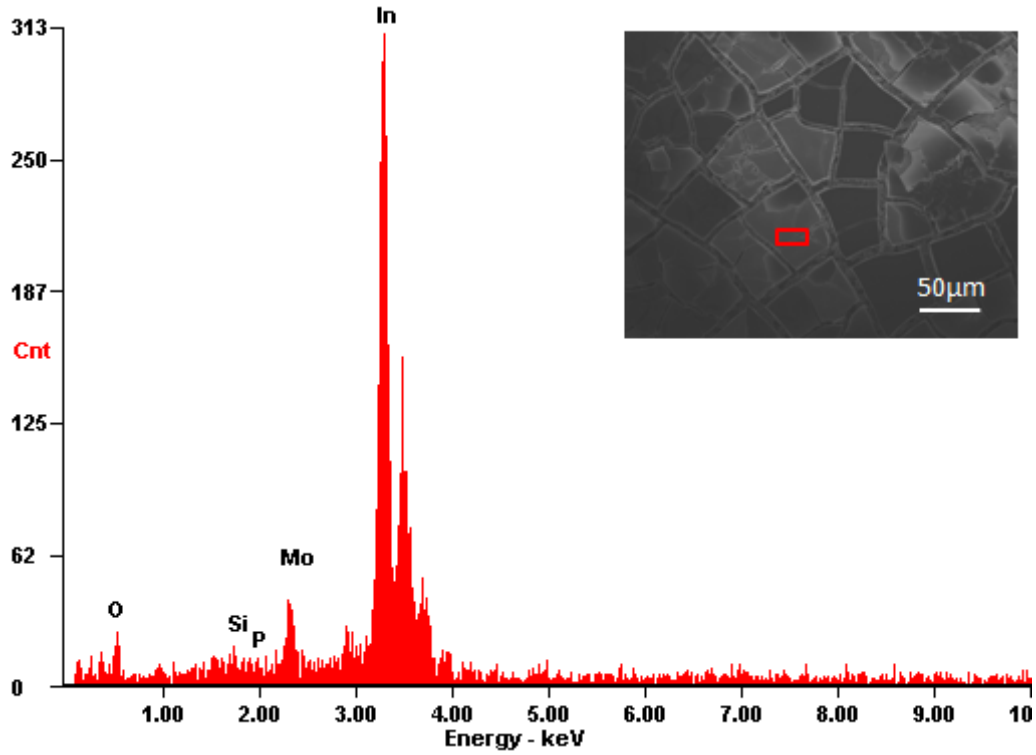

Figure 59: EDX spectrum for sample B90b after annealing and SEM image of the investigated area

For sample B90a results of a broad surface EDX analysis are reported in *Fig.60.*

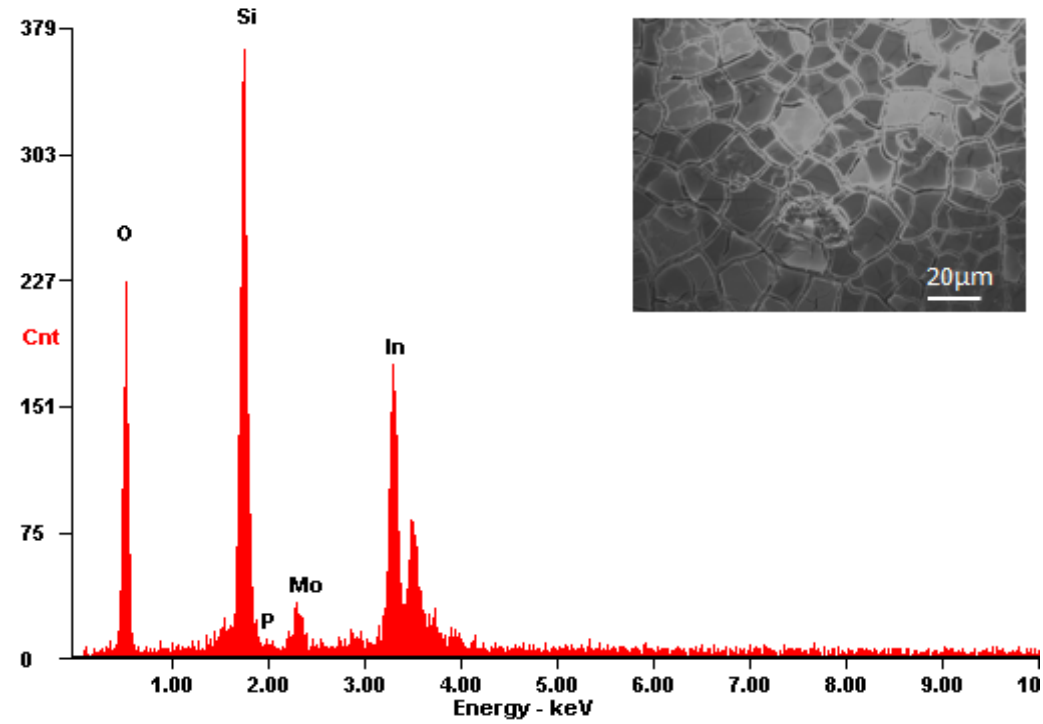

Figure 60: EDX for sample B90a after annealing and SEM image of the investigated area

EDX was performed also on small areas to determine locally the sample composition and structure, results are shown in *Fig.61* and *Fig.62*, red rectangles point out the portions analysed.

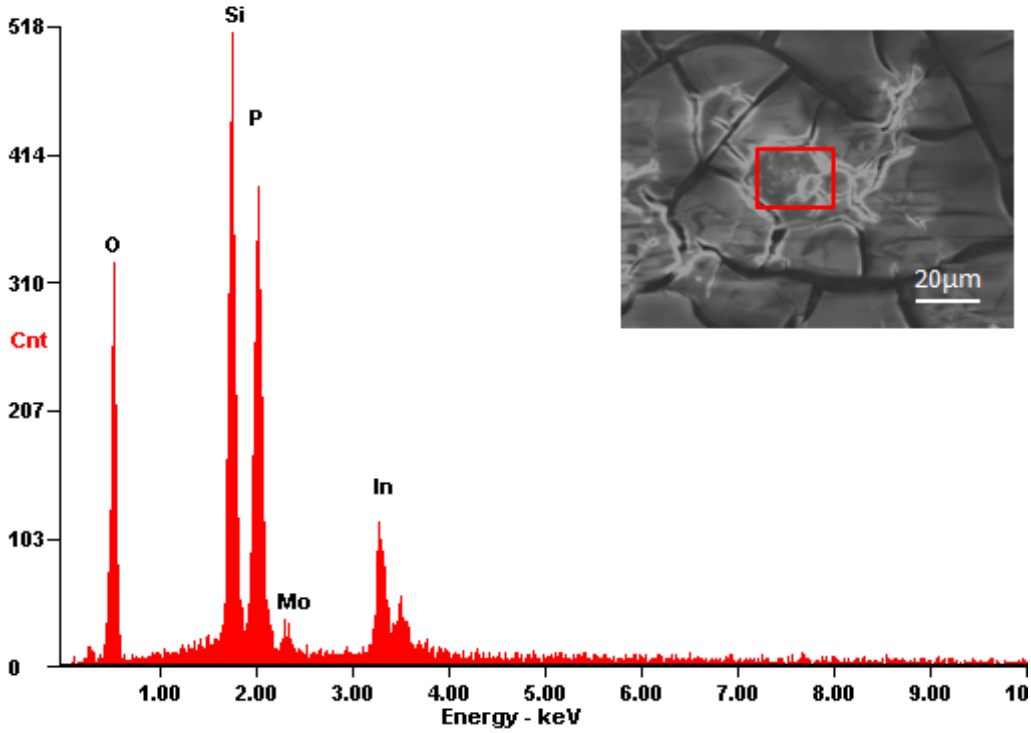

Figure 61: EDX for sample B90a after annealing and SEM image of the investigated area

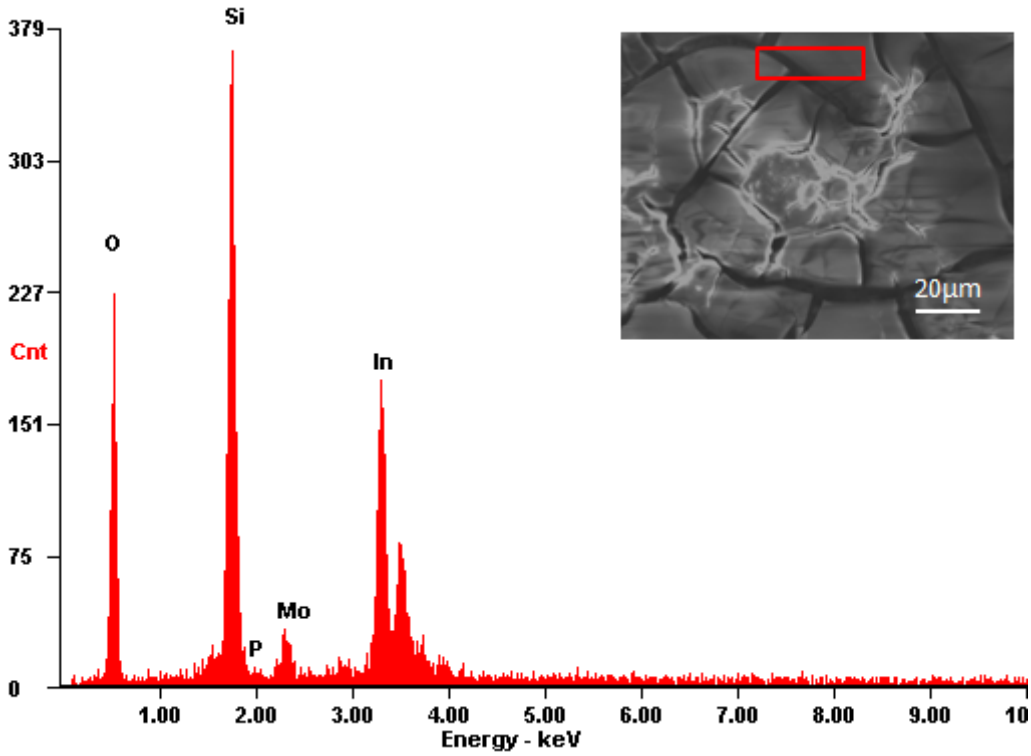

Figure 62: EDX spectrum for sample B90a after annealing and SEM image of the investigated area

3.3 PURE INDIUM PLATING AND SUBSEQUENT PHOSPHORUS INCORPORATION

This group of experiments is intrinsically divided into two different steps, the first part is relative to the pure indium plating and the second to the successive phosphorus incorporation. For this reason results are presented making a distinction between these two processes. At first just characterization about the pure indium layers is reported, then samples at the end of the production process are considered. This is necessary because not all the studies on pure indium plating led to samples suitable for phosphorus incorporation. Moreover some studies were performed exclusively to improve morphology of the pure indium layer.

3.3.1 Pure indium plating

Pure indium plating was performed both with DC and with pulsed current, results are divided depending on the type of current imposed during deposition. All the depositions were performed on commercial molybdenum foil.

3.3.1.1 DC deposition

DC deposition was the most investigated technique. Just some significant results are reported here, but several samples were produced in the same conditions to supply substrates for phosphorus incorporation.

Fig.63 shows EDX spectrum and SEM image for sample B58, this was produced in the following conditions:

- Solution: 100mM $In_2(SO_4)_3$;
- Deposition conditions: t= 15min, T= 25°C, i=-10mA/cm^2;

For most of the pure indium samples XRD analysis wasn't performed since composition was known, presence of detrimental impurities was therefore investigated using EDX elemental analysis associated with SEM imaging, in order to observe surface morphology.

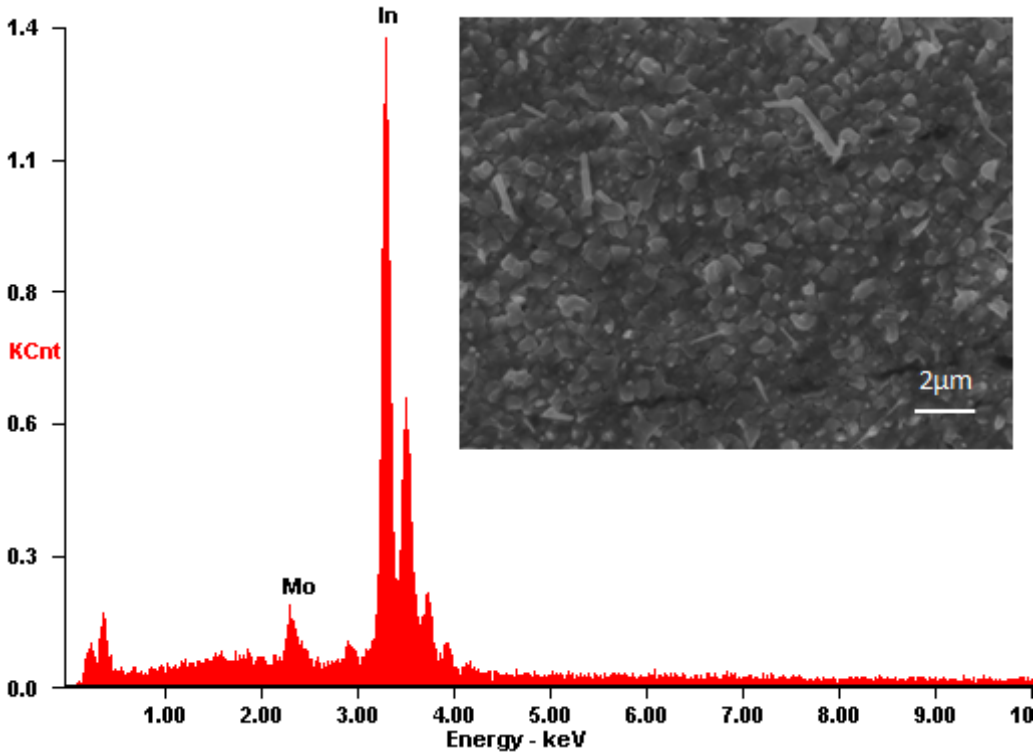

Figure 63: EDX spectrum for sample B58 and SEM image of the investigated area

Sample B60 was produced under the same conditions as B58 except for deposition time, that was increased to 1 hour, SEM image and EDX analysis are reported in *Fig.64.*

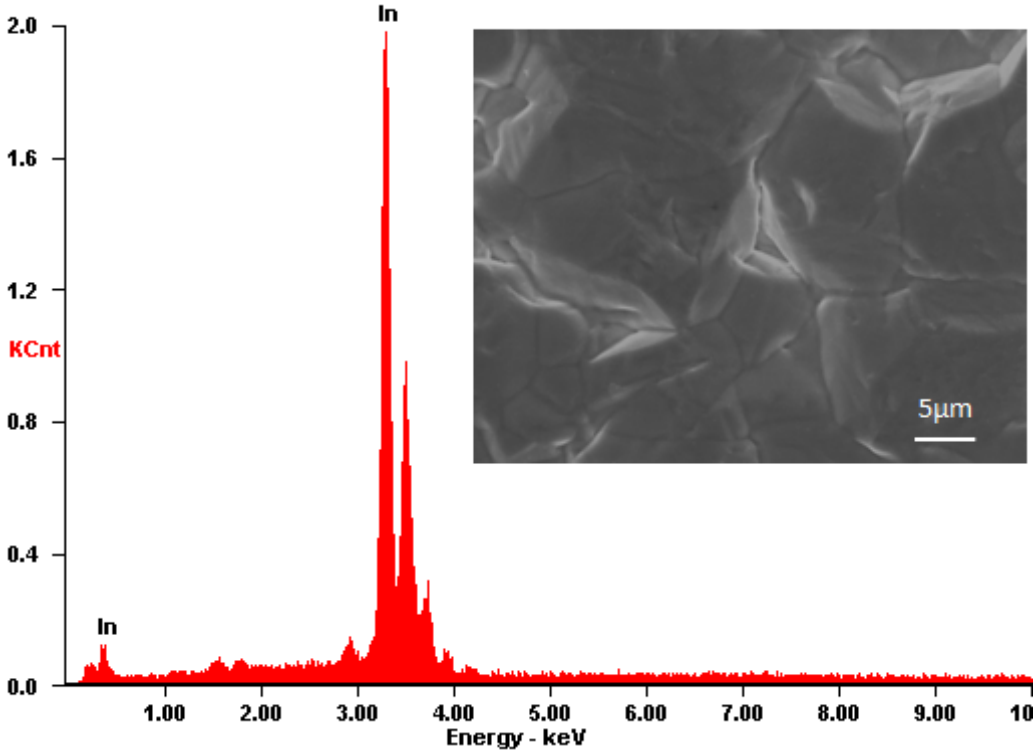

Figure 64: EDX spectrum for sample B60 and SEM image of the investigated area

Sample B69 (*Fig.65*) was produced in the following conditions:

- Solution: 25mM $In_2(SO_4)_3$;
- Deposition conditions: t= 30min, T= 65°C, i=-15mA/cm^2;

These conditions were used to produce a dozen of samples that underwent phosphorus incorporation processes.

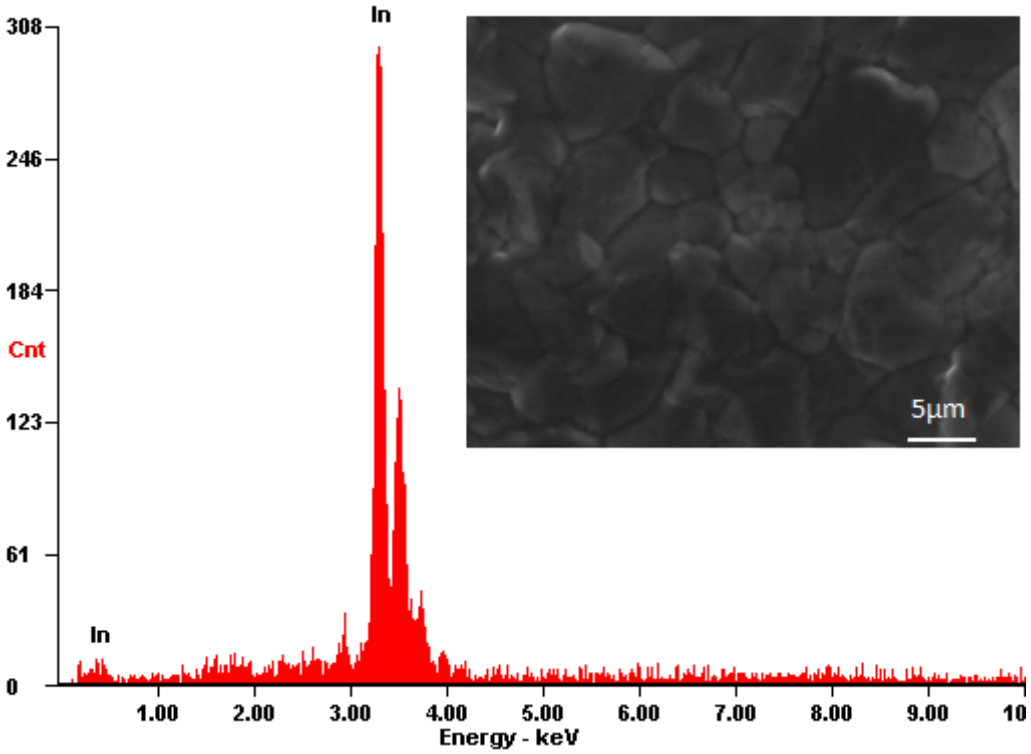

Figure 65: EDX spectrum for sample B69 and SEM image of the investigated area

To improve deposit morphology different solutions were employed, containing citrates. Several conditions were tested, here just significant examples are reported.

One of the first samples to be produced with this different solutions was B104, for this sample AFM imaging was performed to determine surface morphology, this is shown in *Fig.66.* Sample B104 was produced in the following conditions:

- Solution: 125mM $In_2(SO_4)_3$, 85mM $InCl_3$;
  150mM Citric acid, 350mM Na citrate;
- Deposition conditions: t= 5min, T= 25°C, i=-20mA/cm^2;

From AFM measure, data elaboration resulted in a R_a=392nm and a R_{ms}=513nm.

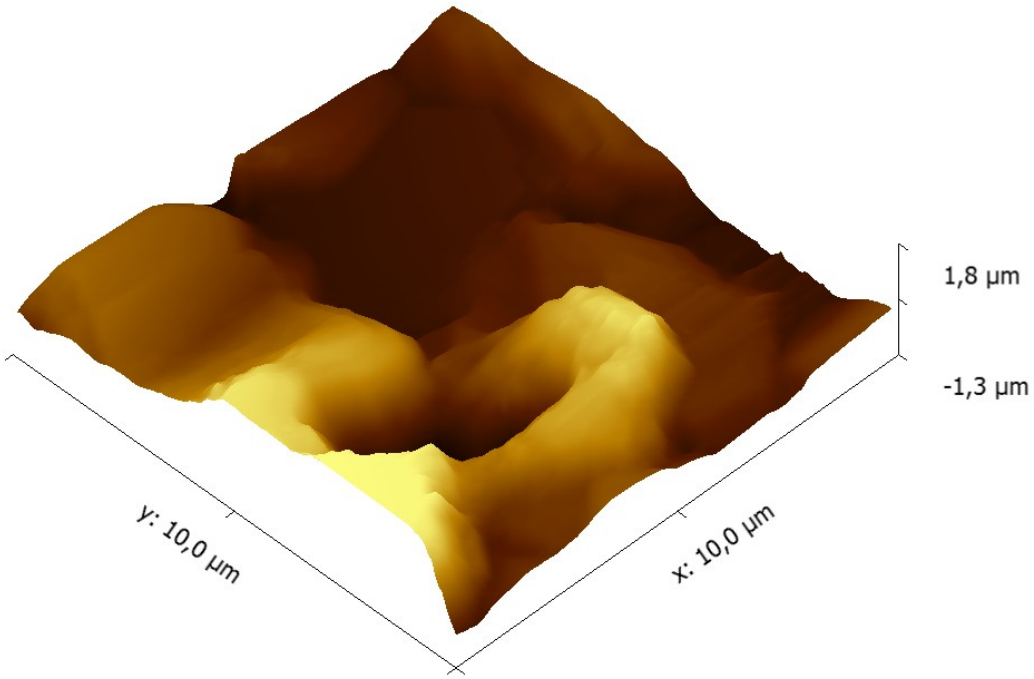

Figure 66: AFM image of sample B104

A new solution was used for successive experiments, optimizing the composition in order to reach pH=2 without addition of HCl (see chapter 2), an example of sample produced with this solution is sample B148, this was deposited in the following conditions:

- Solution: 50mM $In_2(SO_4)_3$, 100mM $InCl_3$;
  250mM Citric acid, 50mM Na citrate;
- Deposition conditions: t= 75s, T= 25°C, i=-35mA/cm^2;

AFM measure for this sample is reported in *Fig.67,* AFM data elaboration gave values

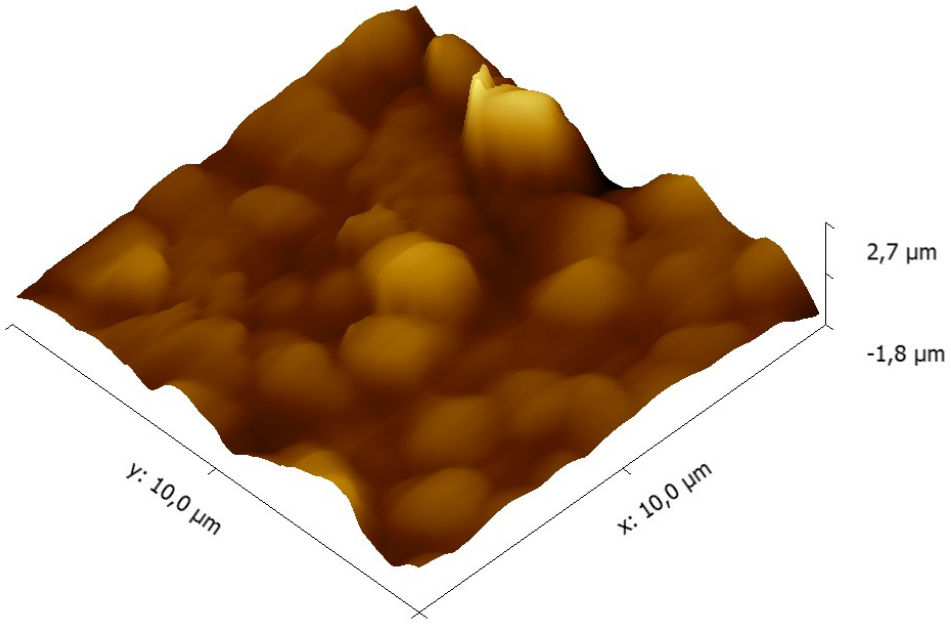

Figure 67: AFM image of sample B148

for roughness R_a=448nm and a R_{ms}=628nm. SEM imaging was performed without EDX analysis, the result is reported in *Fig.68.*

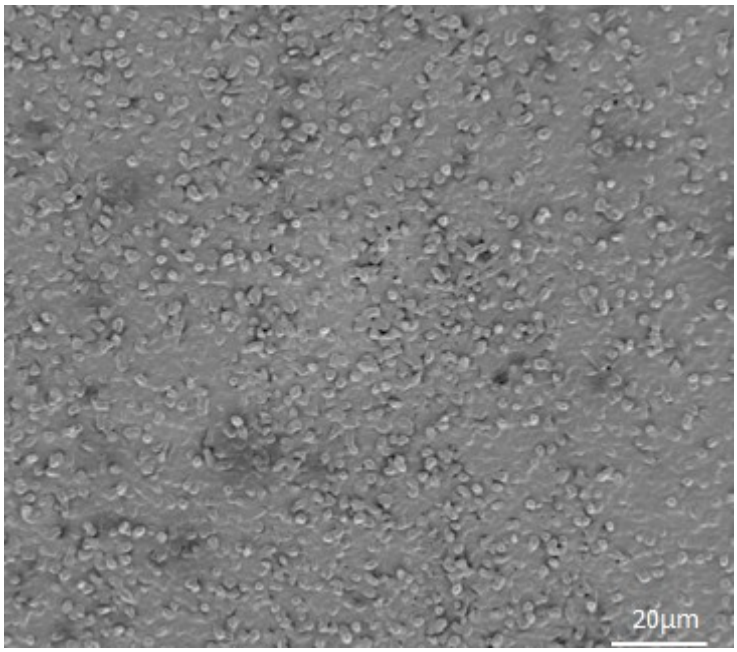

Figure 68: SEM image of sample B148

Sample B151 was produced in similar conditions, the only difference with respect to sample B148 is the deposition time was increased to 90s. Results for SEM imaging are shown in *Fig.69* and in *Fig.70* results on AFM imaging are presented.

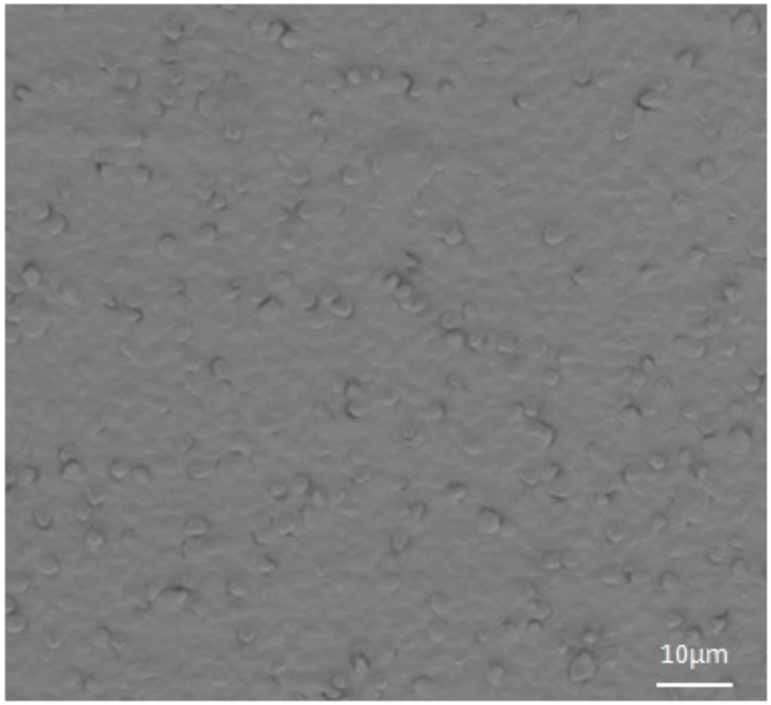

Figure 69: SEM image of sample B151

AFM data elaboration gave roughness parameters R_a=218nm and R_{ms}=293nm.

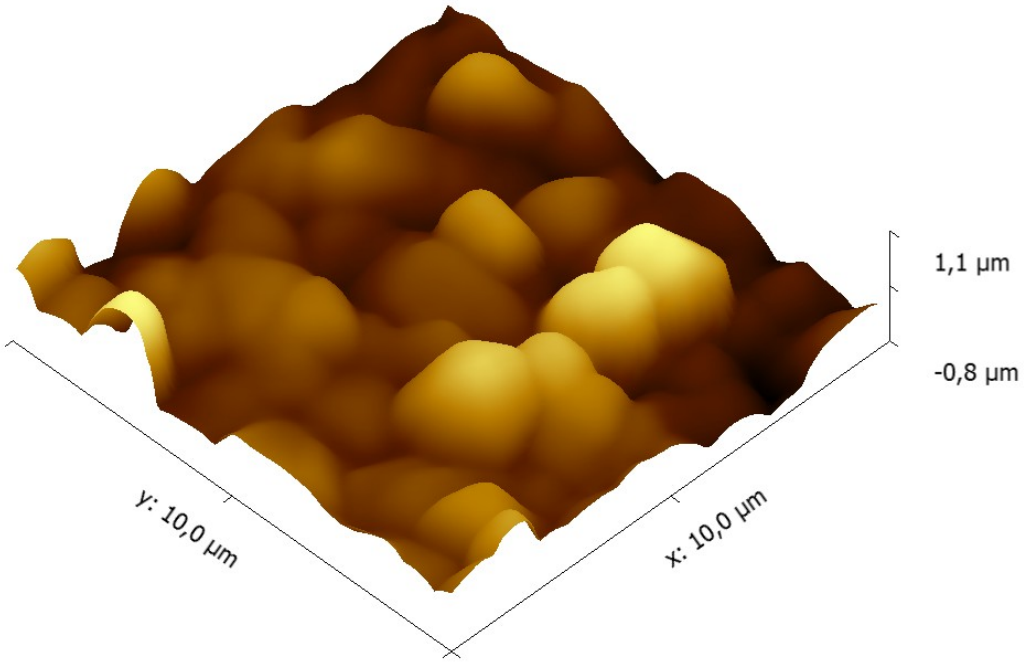

Figure 70: AFM image of sample B151

Just for comparison purposes a deposition was performed in the same experimental condition of sample B151 on a copper substrate, the resulting AFM measure is reported in *Fig.71*. Roughness resulted to be R_a=162nm and R_{ms}=210nm.

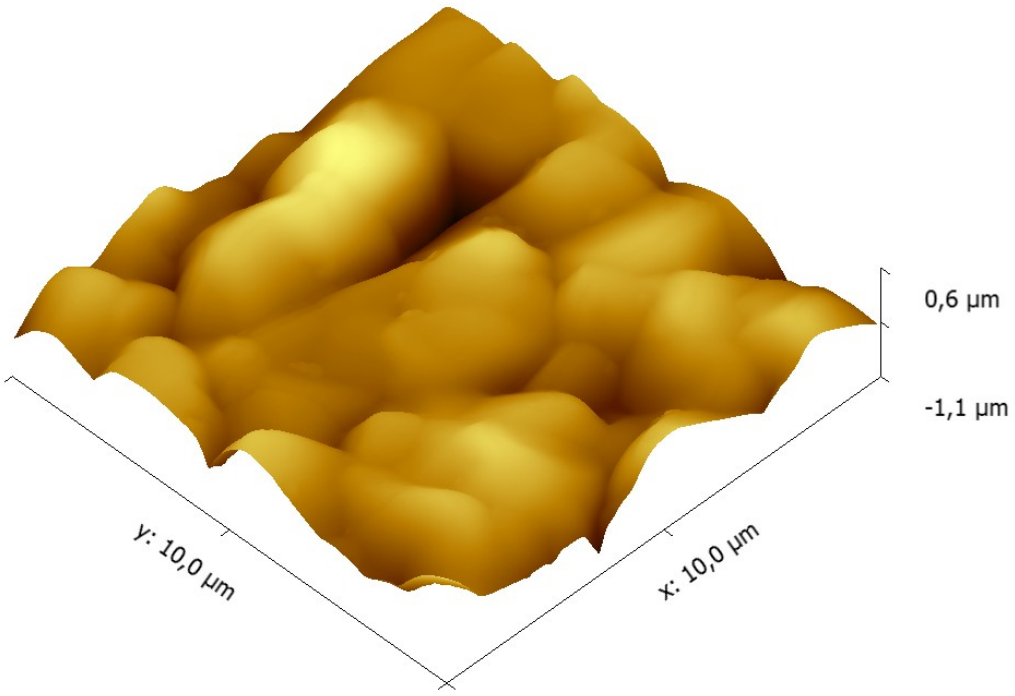

Figure 71: AFM image for In deposit on copper

3.3.1.2 pulsed current deposition

Pulsed deposition was performed using high current density and highly concentrated solutions. An example is sample B184, voltage profile during deposition is reported in *Fig.72.*

Sample B184 was produced in the conditions reported in *Table3.3*

Table 3.3

Sample	Solution	Duty	T	Period	Average *i*	Deposition t
B184	1M $InCl_3$	12.5%	25°C	2s	100mA/cm^2s	60s
B188	1M $InCl_3$	12.5%	25°C	2s	100mA/cm^2s	90s

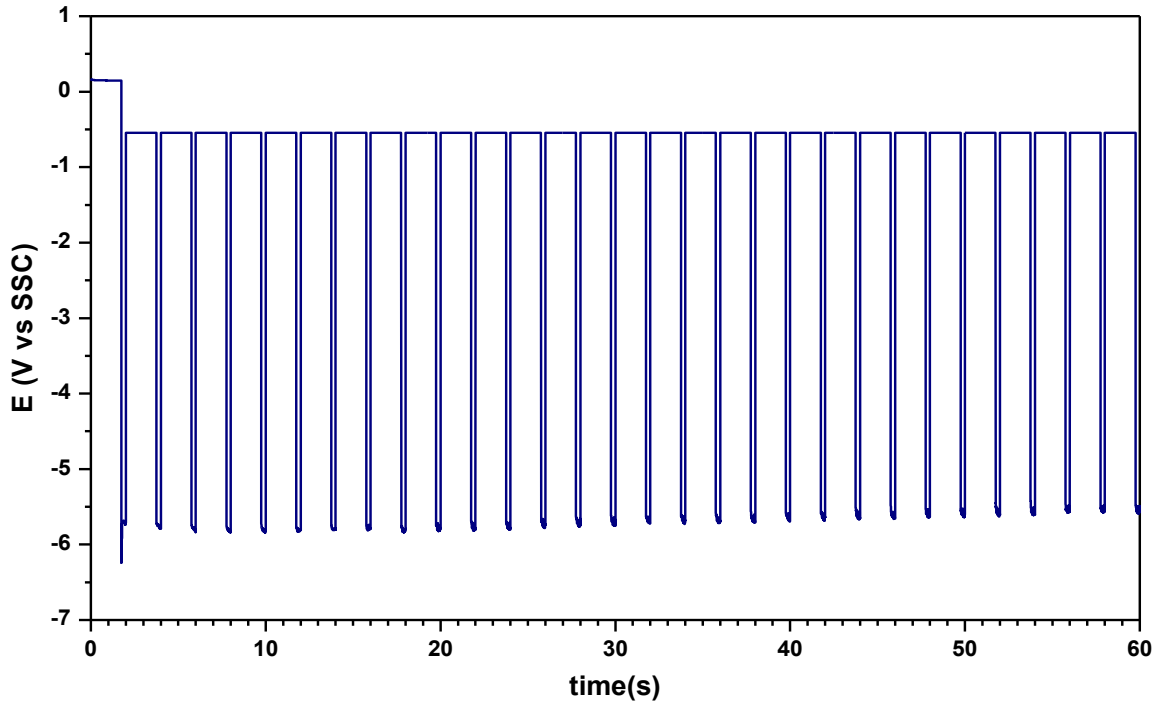

Figure 72: Voltage profile during pulsed deposition for sample B184

The resulting deposit is shown in *Fig.73*.

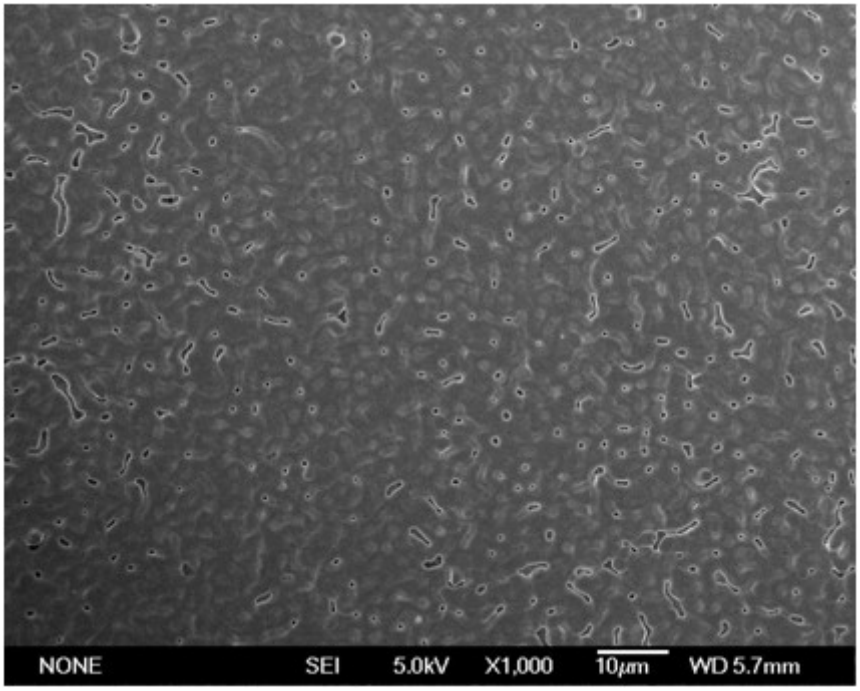

Figure 73: SEM image of the surface of B184

Sample B188 was produced in the same conditions increasing total deposition time (*Table 3.3*), the potential profile is reported in *Fig.74.*

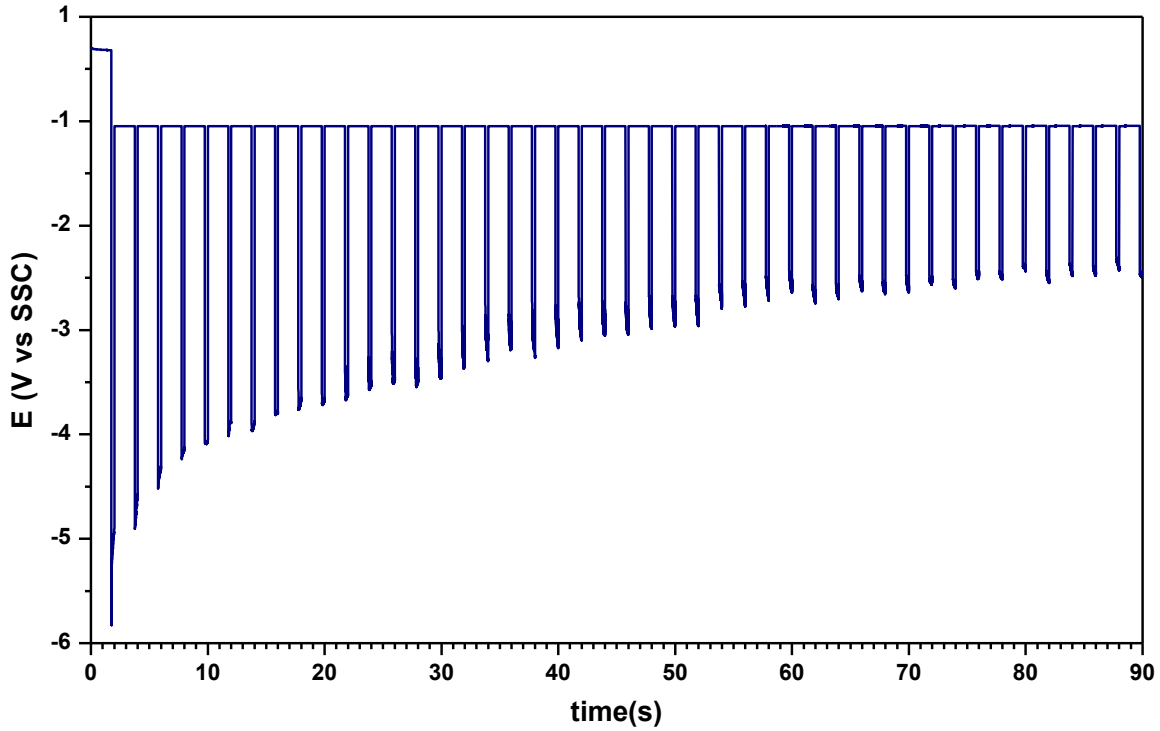

Figure 74: Voltage profile during pulsed deposition for sample B188

SEM imaging was performed on this sample to determine surface appearance and the result are shown in *Fig.75*

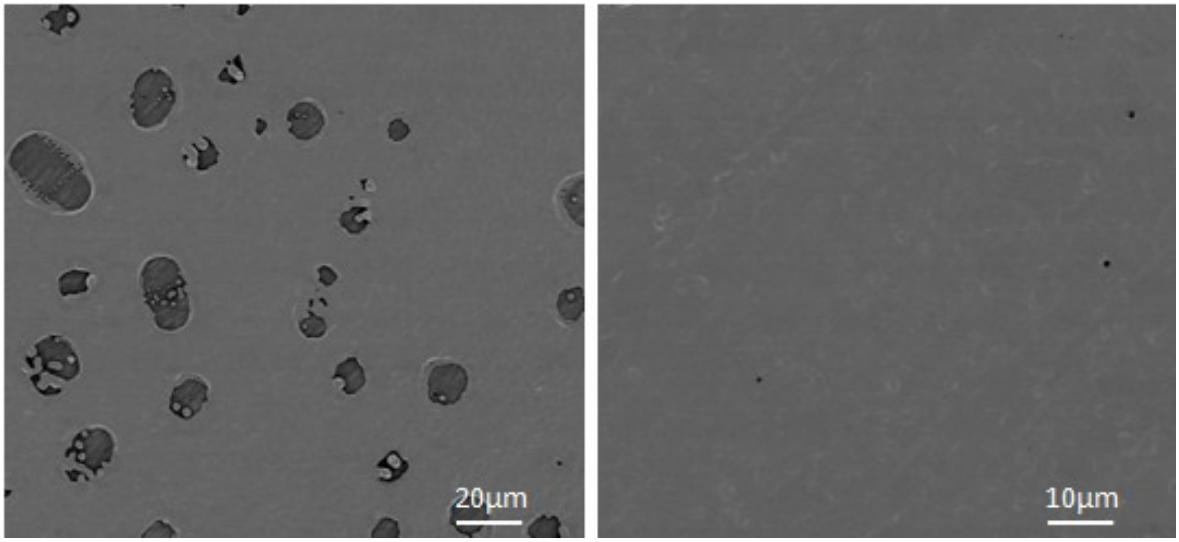

Figure 75: SEM images of the surface of B188

3.3.2 Phosphorus incorporation

Phosphorus incorporation in the pure indium film was performed either by phosphorization or by P_{red} dropcasting and annealing. For sake of simplicity results deriving from these two methods are reported in different paragraphs. Some of the samples cited below were already described previously when reporting results on pure indium.

3.3.2.1 Phosphorization

Pure indium samples were phosphorized in the conditions described in chapter 2, the first samples being phosphorized were produced using low purity (98% purity) indium sulfate. The SEM imagining with EDX analysis relative to sample ECD1 are reported in *Fig.76.* The indium layer of sample ECD1 was produced in the following conditions:

- Solution: 100mM $In_2(SO_4)_3$;
- Deposition conditions: t=60min, T=25°C, i=-10mA/cm^2;

From EDX analysis an In:P atomic ratio equal to 52:48 was found. Another sample (ECD2) was produced under the same experimental conditions but for shorter deposition time, that was reduced to 15min. Results from EDX are the same so are not shown here.

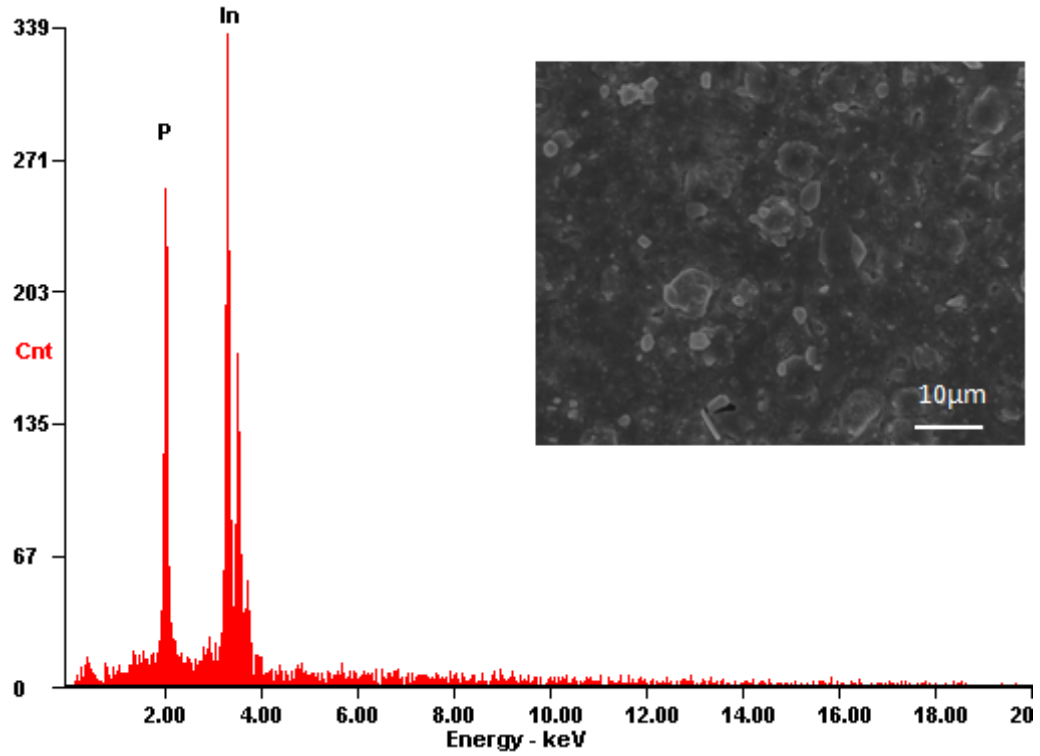

Figure 76: EDX analysis and SEM image of the analysed area for sample ECD1

After phosphorization PL and TRPL were performed on samples ECD1 and ECD2, results are reported in *Fig.77* and *Fig.78.*

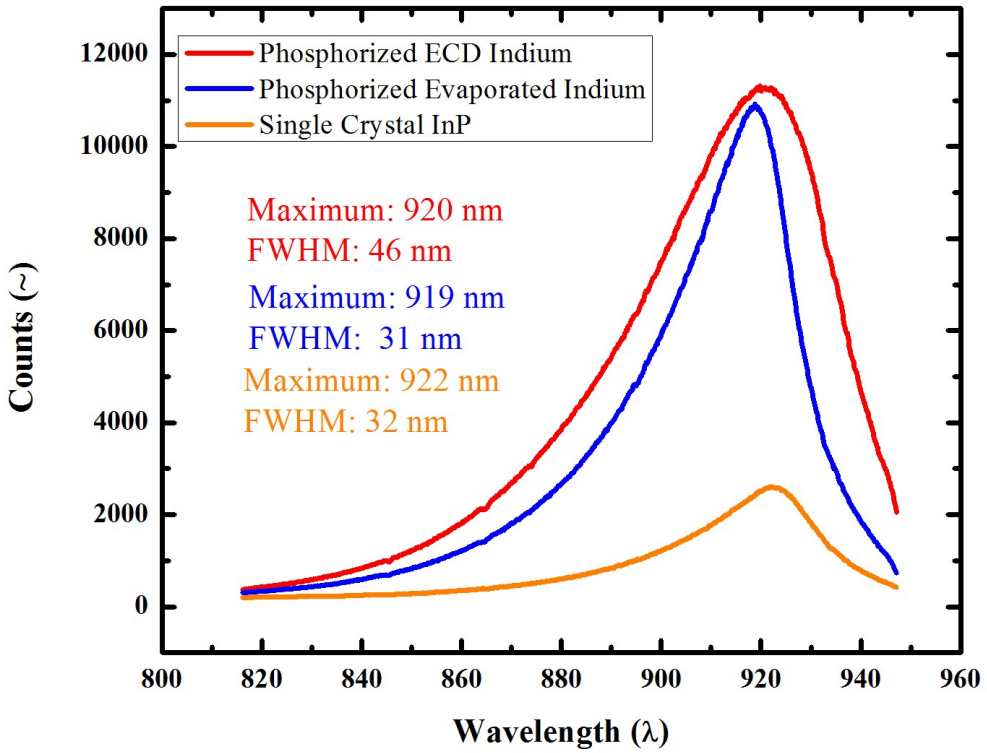

Figure 77: PL for sample ECD1 after phosphorization with comparison

TRPL results for ECD1 and ECD2 are compared with those of an InP layer obtained by In evaporation and subsequent phosphorization. Exciton lifetime was found to be 2.15ns for the evaporated sample, 0.12ns for sample ECD2 and 0.42ns for sample ECD1. Exciton lifetime is conventionally considered as the time where the relative intensity equals e^{-1}.

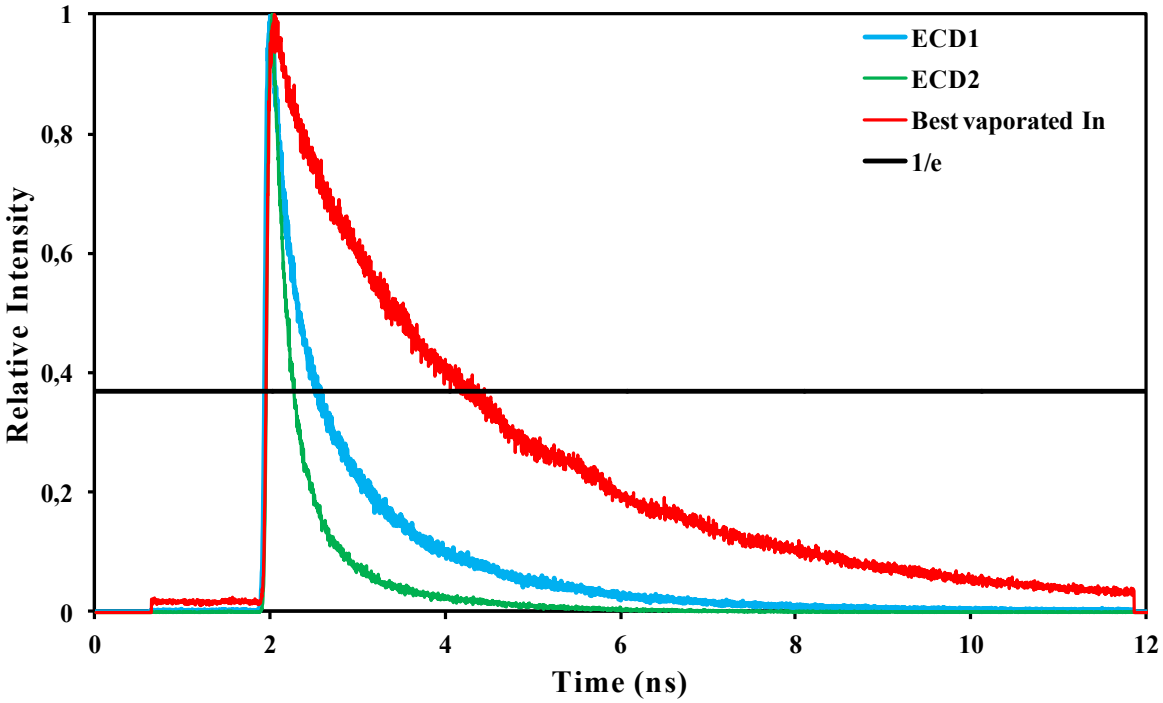

Figure 78: TRPL for ECD1 and ECD2 after phosphorization with comparison

Successively pure indium samples were produced using high purity indium sulfate. Sample B69 is an example, indium layer production was described previously while phosphorization process is the one described in chapter 2. After phosphorization SEM imaging with EDX elemental analysis was performed, results are shown in *Fig.79*. From EDX deposit after phosphorization has In:P=55:45.

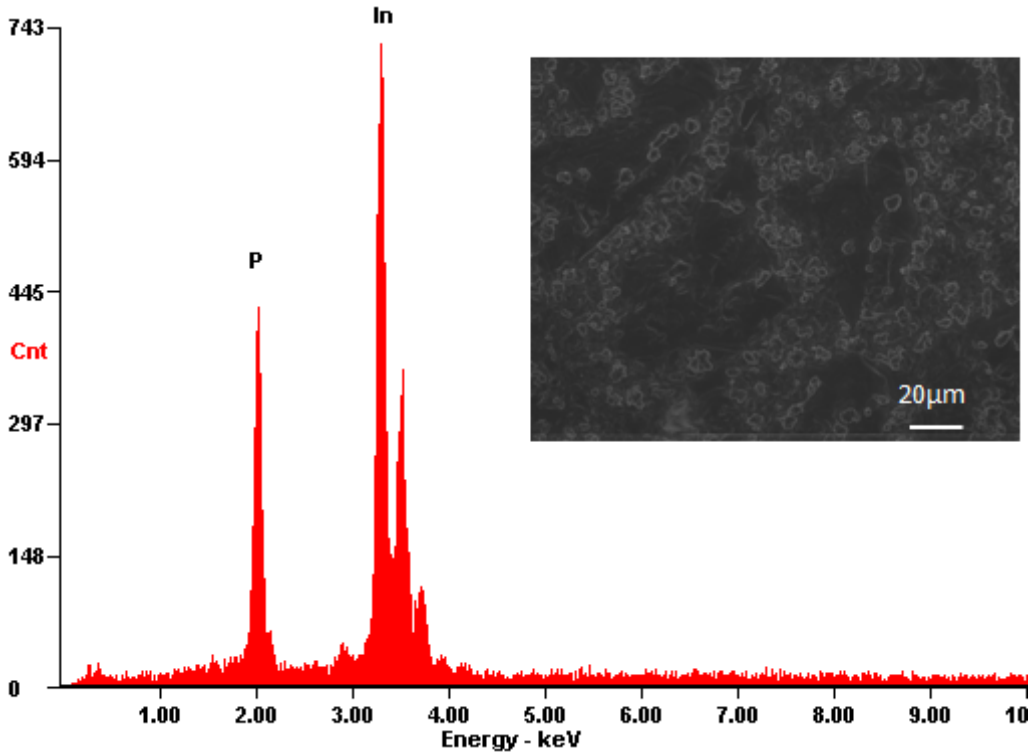

Figure 79: EDX analysis and SEM image of the analysed area for sample B69

XRD analysis was also performed on the sample after phosphorization, giving the results shown in *Fig.80.*

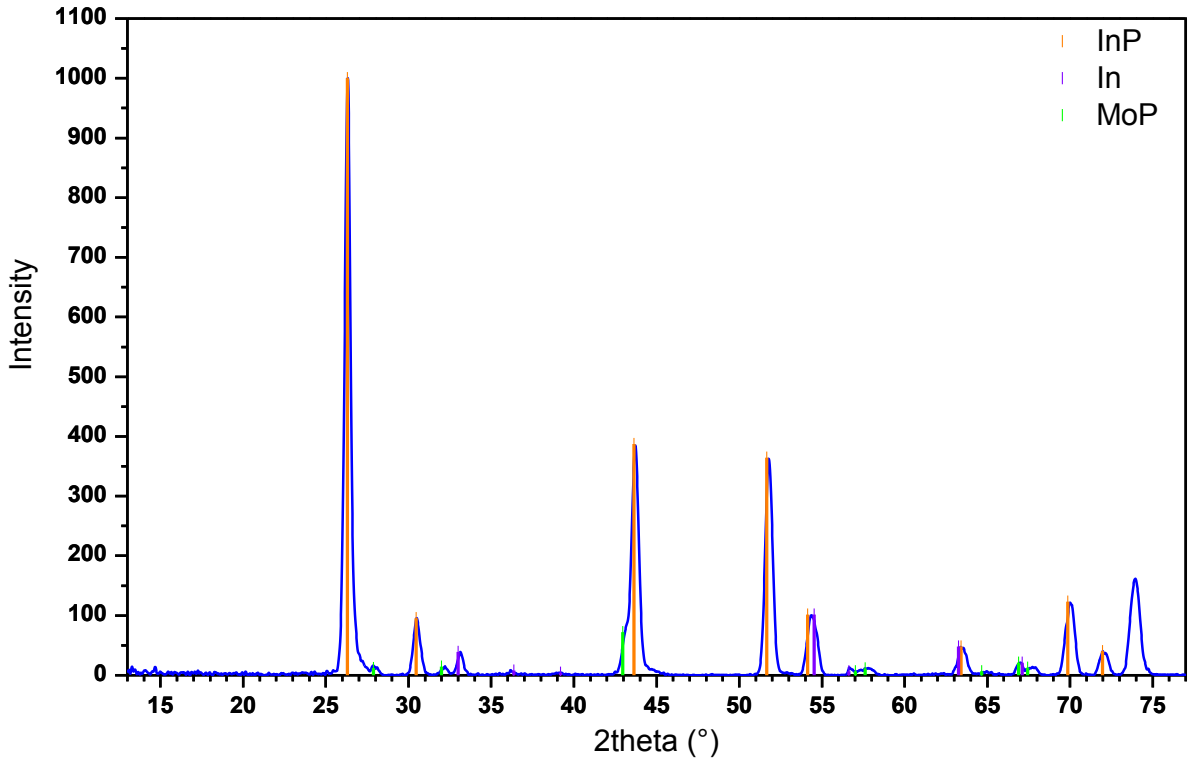

Figure 80: XRD spectrum for sample B69 after phosphorization

TRPL was performed and compared with an high quality sample obtained by In evaporation and phosphorization in the same conditions giving the results reported in *Fig.81*. Exciton lifetime resulted to be 2.2ns for the evaporated sample and 2.3ns for B69.

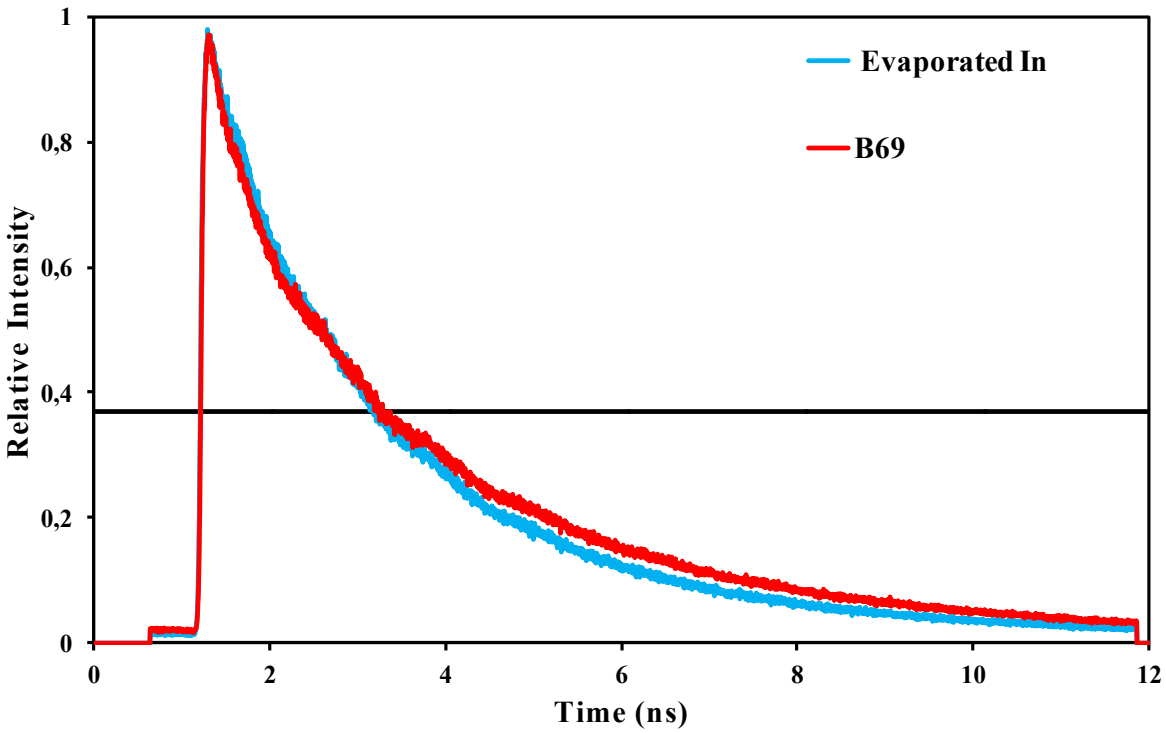

Figure 81: TRPL results for sample B69 with comparison

3.3.2.2 Red phosphorus dropcasting

Red phosphorus dropcasting was performed as described in chapter 2, results for one-step dropcasting are not reported since annealing without capping layer led to remarkable deposit degradation.

Moving to two-step dropcasting sample B87 is considered, deposition conditions are the same described before for sample B69. After dropcasting a 500nm SiO_2 cap was e-beam evaporated, finally annealing was performed. Annealing conditions for sample B87 are reported in *Table3.4*.

Table 3.4

Sample	Technique	Time (s)	Temperature (°C)	Environment	Pressure (torr)
B87	RTA	15	500	N_2	760
B92	RTA	15	500	N_2	760

After annealing characterization was carried out, *Fig.82* shows XRD spectrum for the sample.

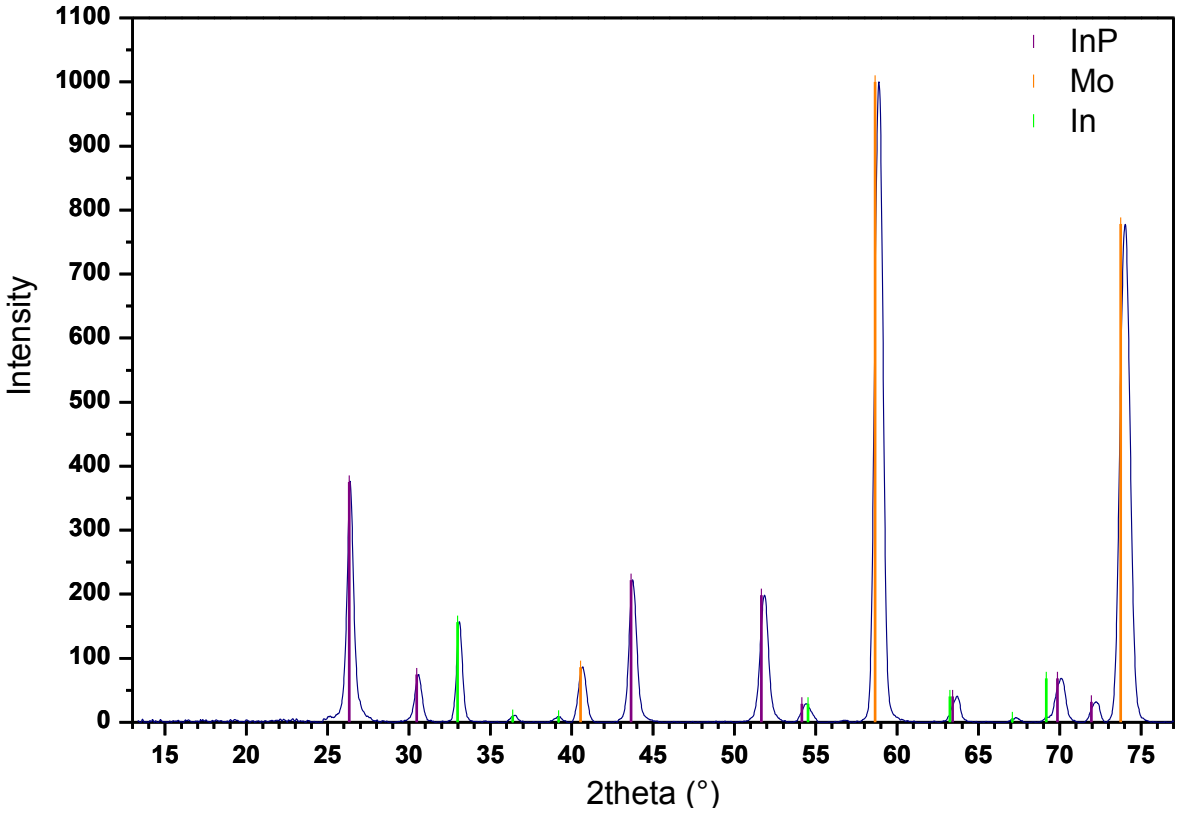

Figure 82: XRD spectrum for sample B87 after annealing

SEM imaging was performed together with EDX elemental analysis, results are shown in *Fig.83.* From EDX analysis the sample composition is found to have In:P=57:43.

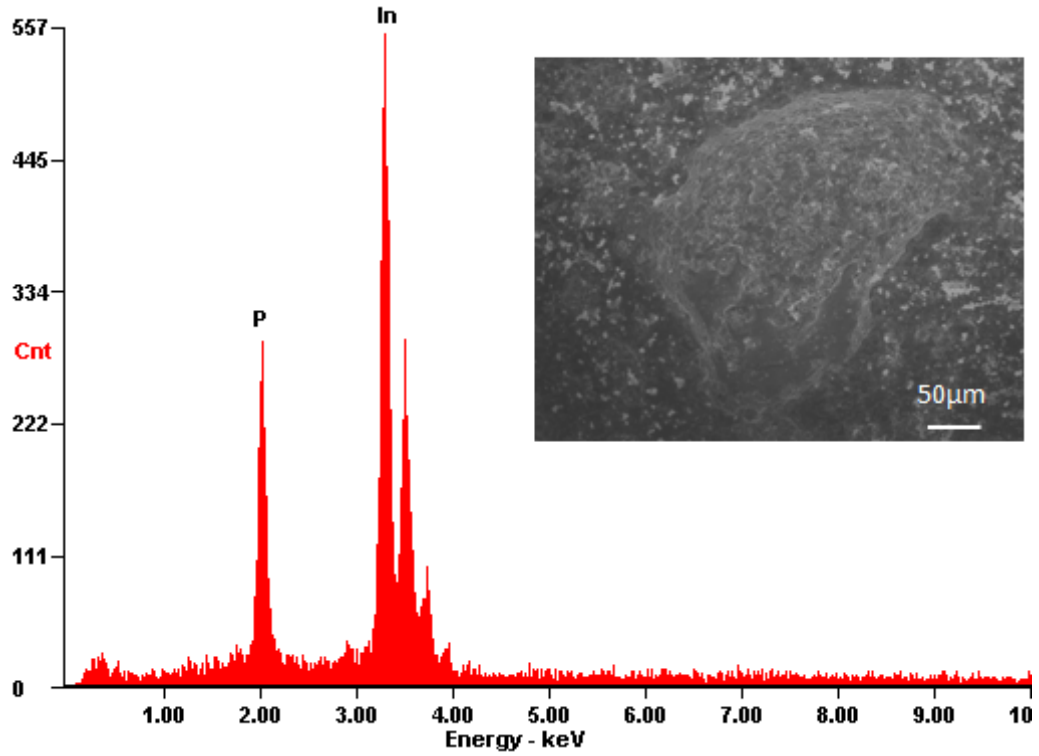

Figure 83: EDX spectrum with SEM image of the analysed area for sample B87

Sample B92 was produced in the same conditions as sample B87 (*Table3.4)* both considering In deposition process and phosphorization.

XRD characterization was performed after annealing, results are reported in *Fig.84.*

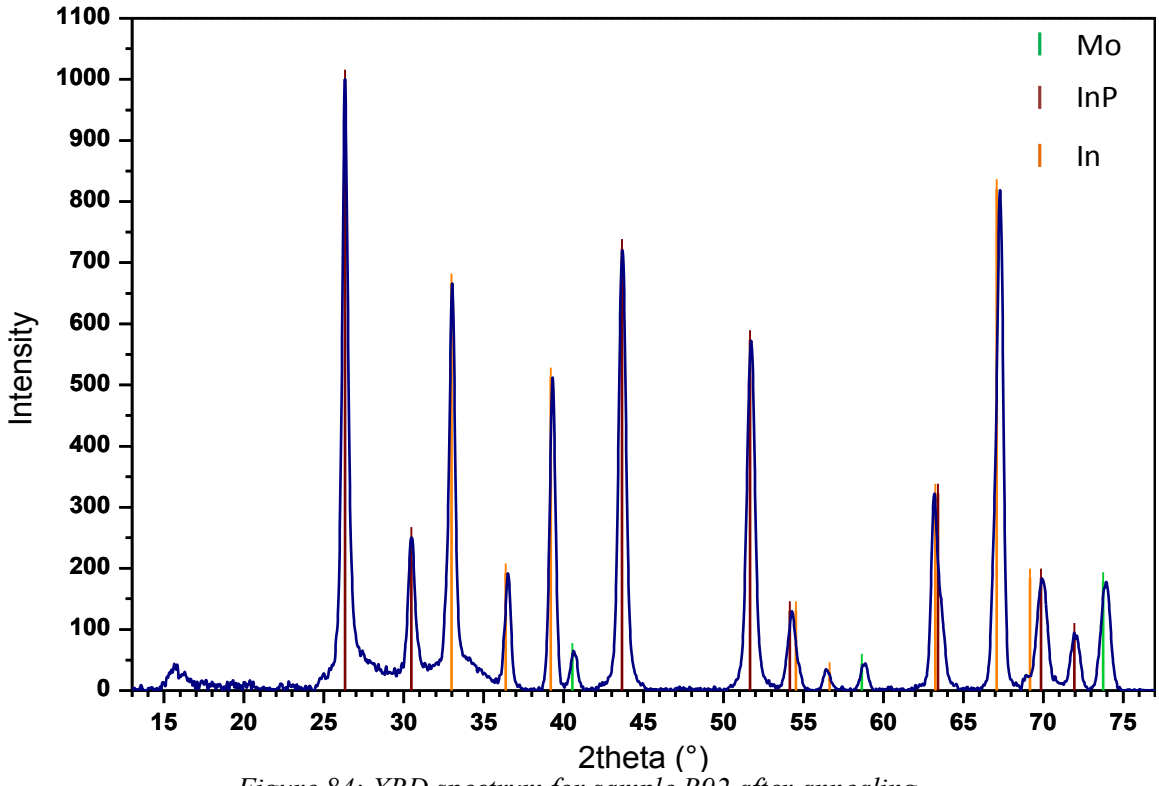

Figure 84: XRD spectrum for sample B92 after annealing

PL measure was performed both for sample B87 and B92, the results are shown in *Fig.85,* peak is located at 890nm for sample B87 and at 901nm for sample B92.

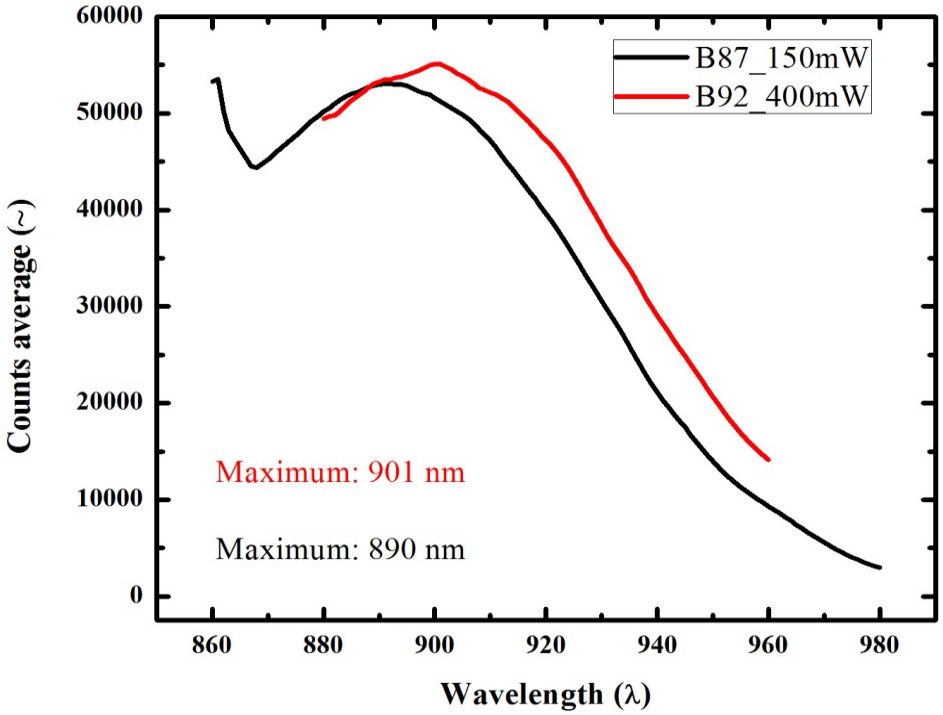

Figure 85: PL for sample B87 and B92 after phosphorization

TRPL measurements were performed on both the samples. Results are shown in *Fig.86*. Exciton lifetime was measured as 0.2ns for sample B87 and of 0.05ns for sample B92.

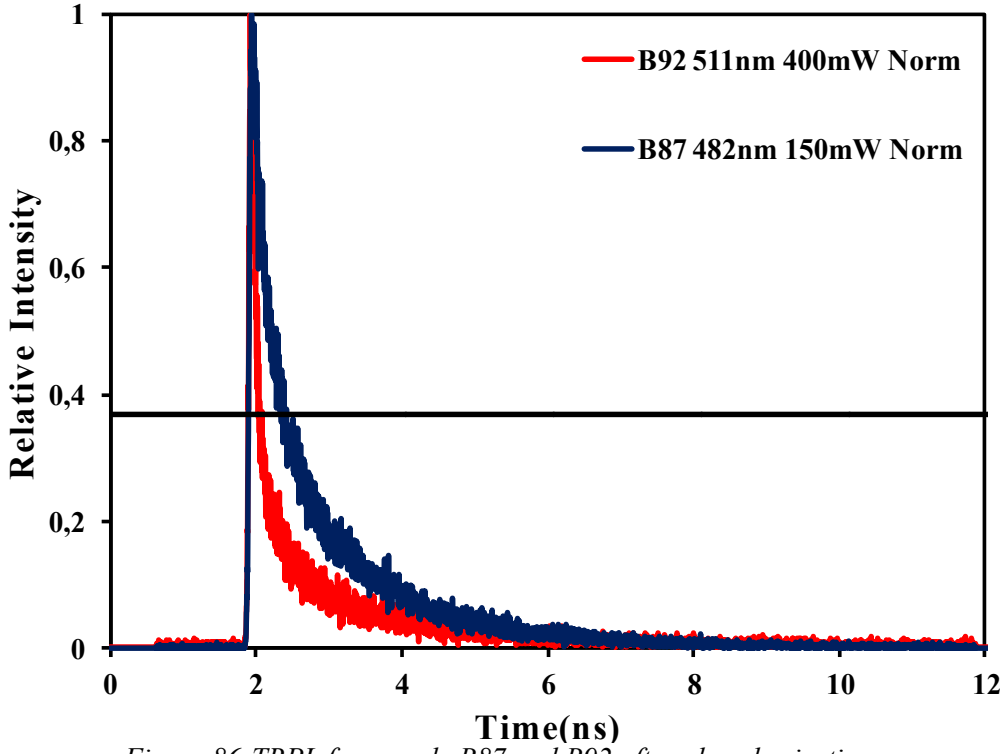

Figure 86:TRPL for sample B87 and B92 after phosphorization

Three-step dropcasting was employed to produce sample B106, the pure indium layer was produced in the following conditions:

- Solution: 25mM $In_2(SO_4)_3$;
- Deposition conditions: t=15min, T=65°C, i=-12mA/cm^2;

After In plating a 500nm silicon dioxide layer was e-beam evaporated on the sample, therefore dropcasting was performed in the usual conditions. Finally another 500nm silicon dioxide capping was e-beam evaporated on the red phosphorus dropcasted layer.

Annealing conditions are reported in *table 3.5*

Table 3.5

Sample	Technique	Time (s)	Bottom T (°C)	Top T (°C)	Environment	Pressure (torr)
B106	CSS	-	500	0	N_2	100

XRD was performed after annealing and results are reported in *Fig.87.*

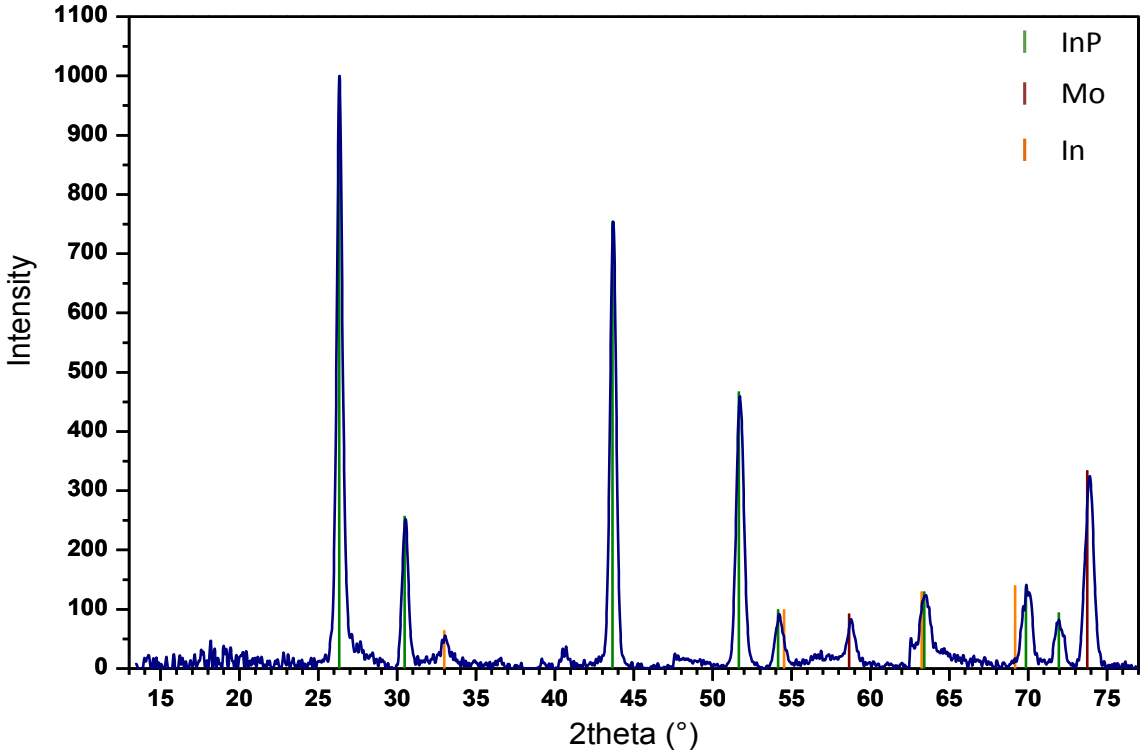

Figure 87: XRD spectrum for sample B106 after annealing

SEM imaging with EDX elemental analysis was performed after thermal treatment and results are reported in *Fig.88* and *Fig.89*.

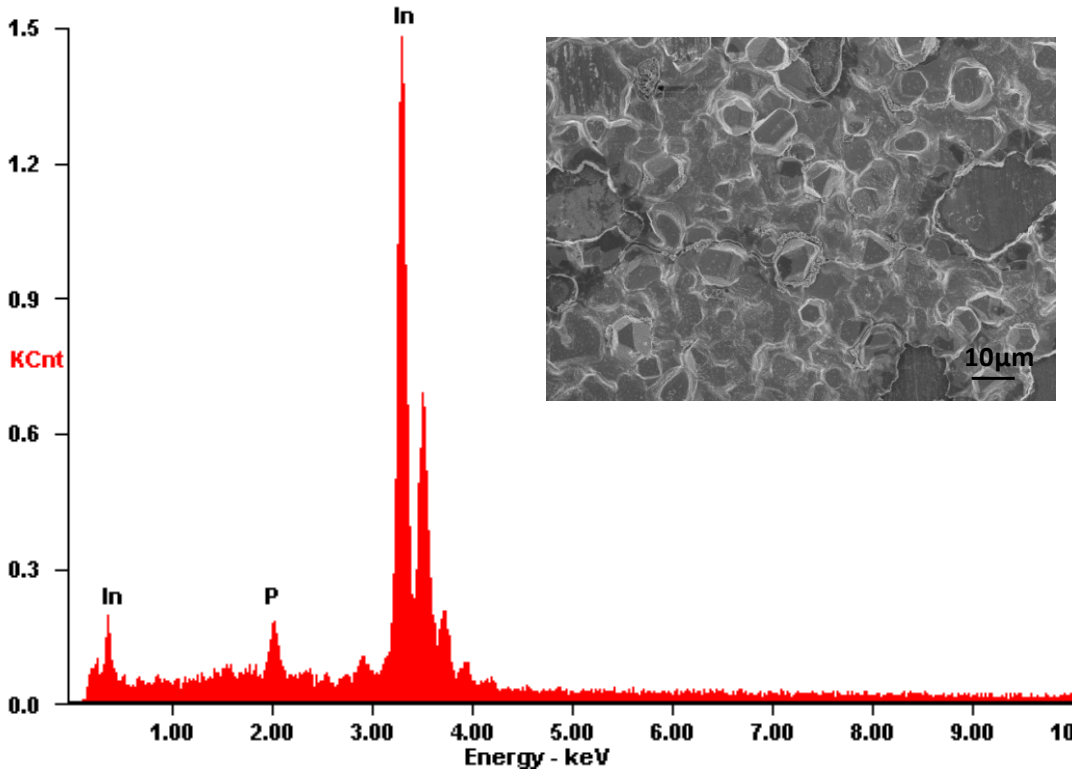

Figure 88: EDX analysis with SEM image of the investigated area for B106 after annealing

From elemental analysis a lack of phosphorus is noticed, In:P ratio is found to vary with the position and its average value is 6:1.

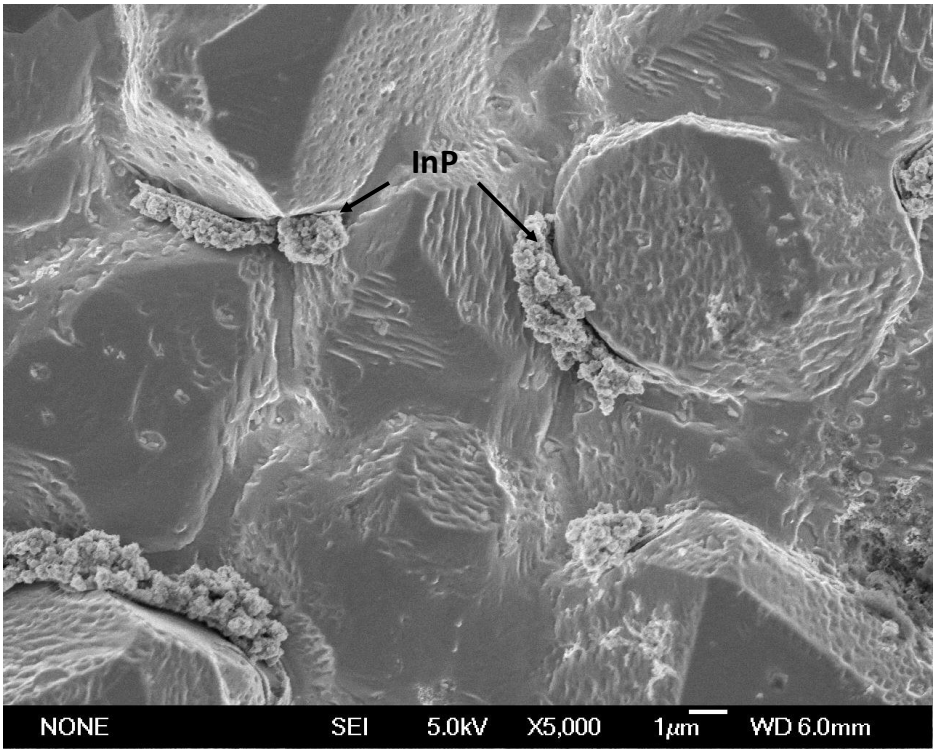

Figure 89: SEM image of B106 after annealing

3.4 ELECTROCHEMICAL CHARACTERIZATION

Electrochemical characterization was performed on solutions used during depositions to determine their behaviour and understand the reactions going on in the plating process. A general rule was followed for graphical representation of the obtained data: for solutions without In ions the graph plotted is relative to the first stabilized cycle (normally the 10^{th}), for solutions containing indium the first cycle is plotted, since In depositions occurs and successive cycles would represent solution activity on In and not on the original working electrode.

3.4.1 Direct InP deposition solutions

Cyclic voltammetry was performed on single reagents used and on combinations of them to understand their individual and cooperative behaviour during deposition. Most of the measurements were performed on the commercial Mo foil used for depositions, some tests were performed also on Ni foil. In *Fig.90* results are reported about a test on Mo foil in a solution of H_3PO_3 100mM.

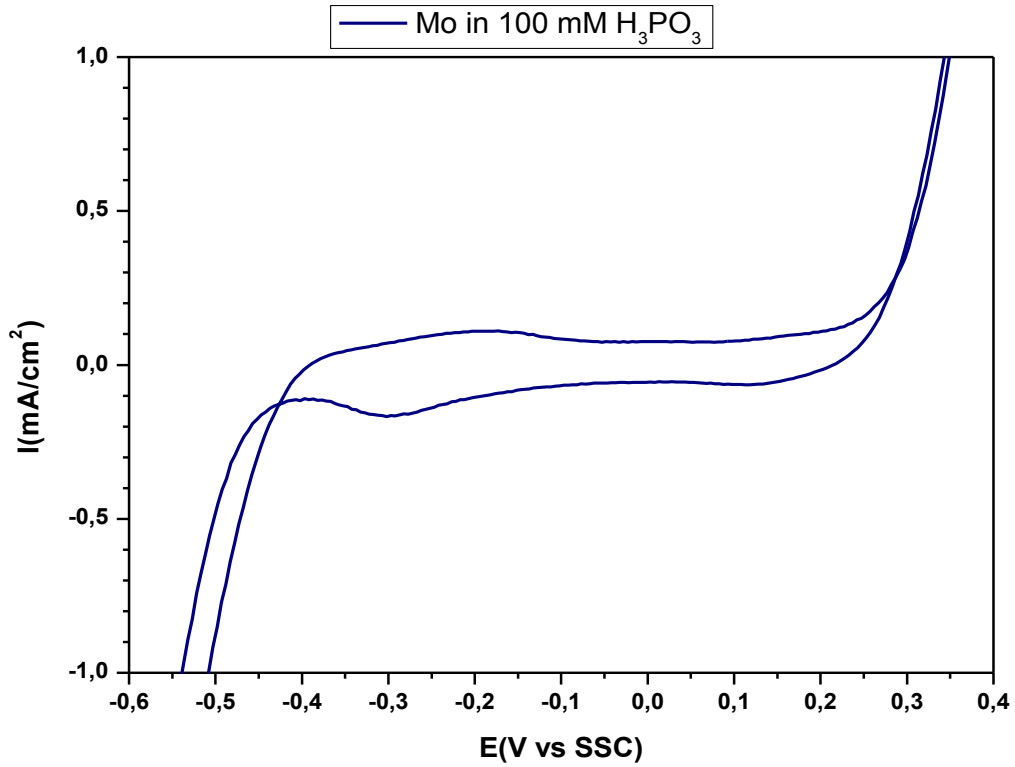

Figure 90: CV for Mo foil in H3PO3 100mM

In *Fig.91* CV is reported for Mo in a solution of H_3PO_4 100mM.

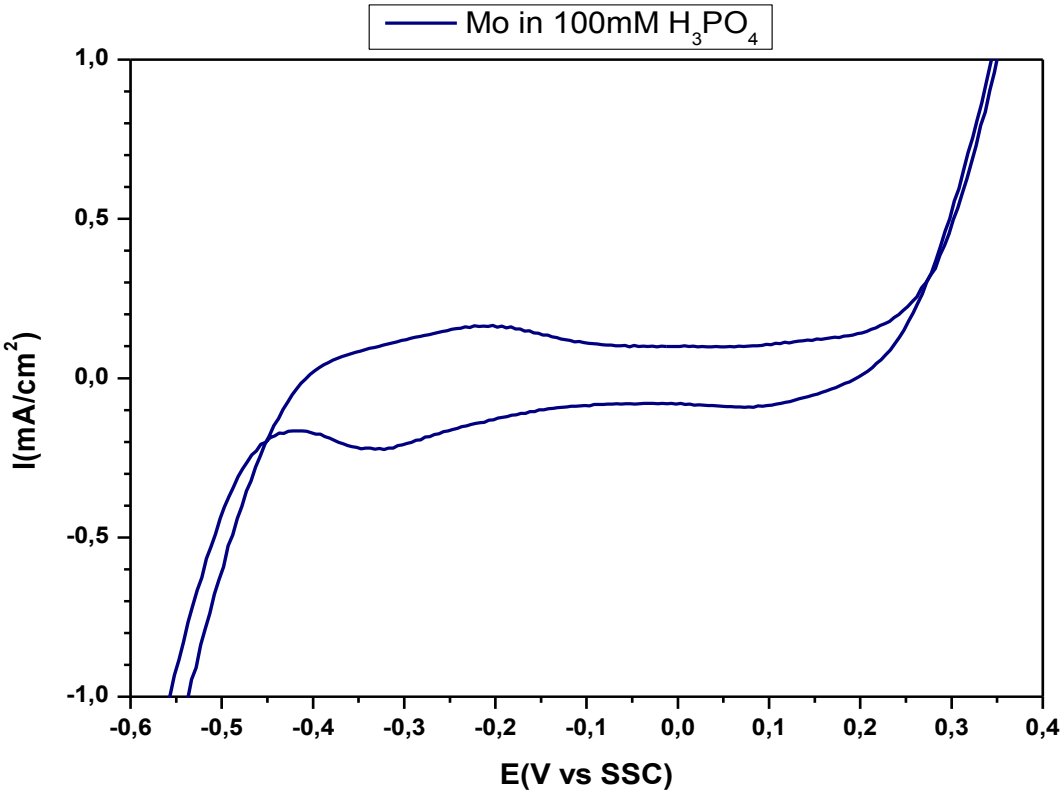

Figure 91: CV for Mo foil in H3PO4 100mM

The same measure was performed on Mo foil also for a solution containing 100mM NaH_2PO_2. Results are shown in *Fig.92.*

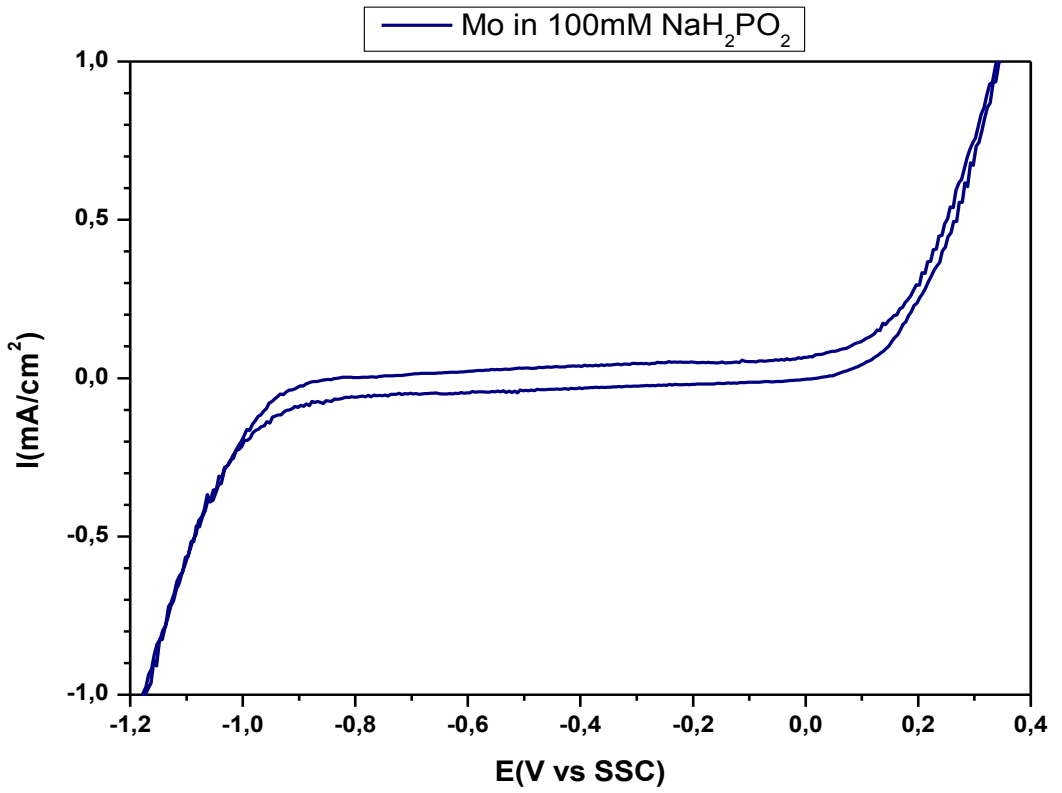

Figure 92: CV for Mo foil in NaH2PO2 100mM

A 100mM $InCl_3$ solution was finally characterized on Mo, results are shown in *Fig.93*

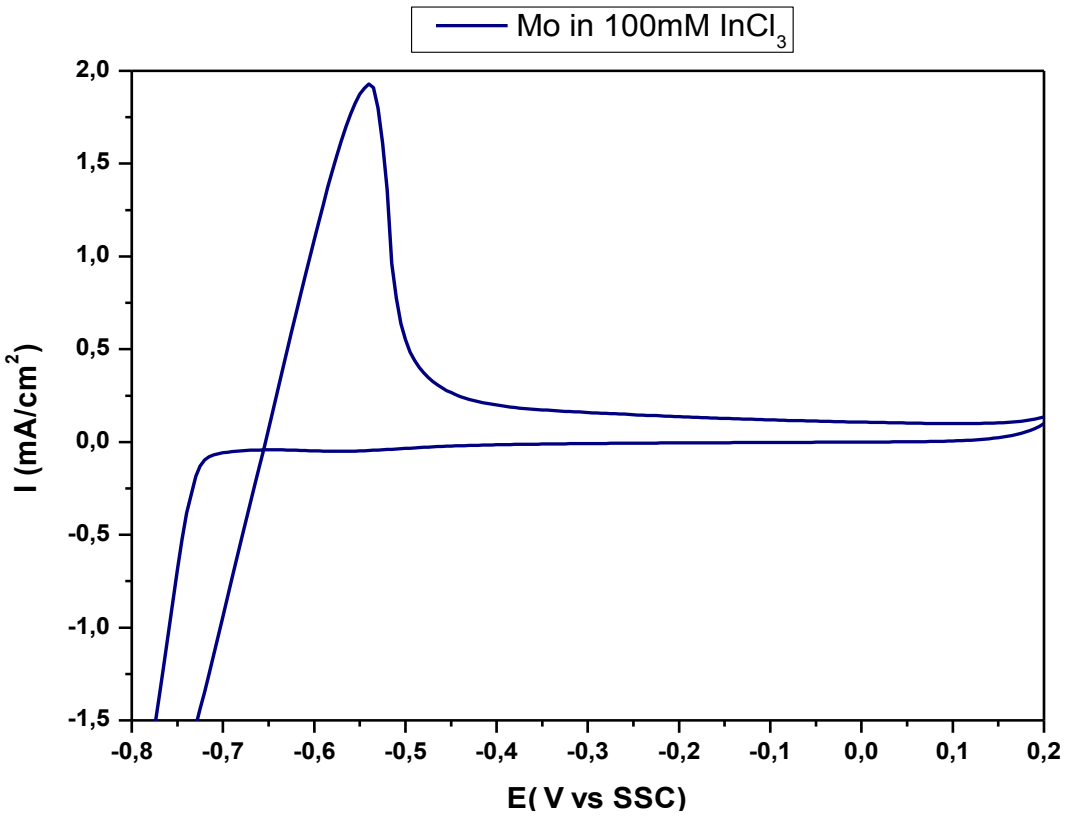

Figure 93: CV for Mo foil in InCl3 100mM

These three test shown above were all performed at room temperature, moreover combinations of phosphorus precursors together with In precursors were studied. Due to the similar results obtained for most of the combinations just some representative plots are reported here. In *Fig.94* a room temperature CV performed on Mo in a solution containing 12.5mM $InCl_3$ and 50mM NaH_2PO_2 is shown.

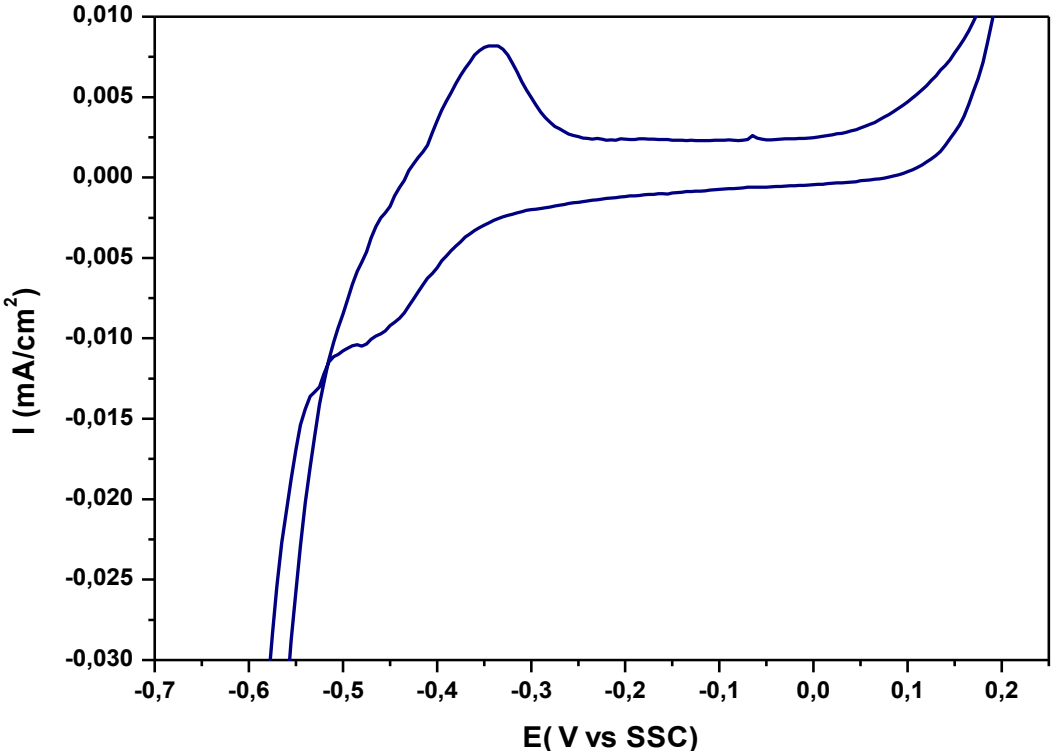

Figure 94: CV for Mo foil in InCl3 12.5mM and NaH2PO2 50mM

This measure was performed with the same solution composition but at 85°C, the resulting CV plot is represented in *Fig.95*.

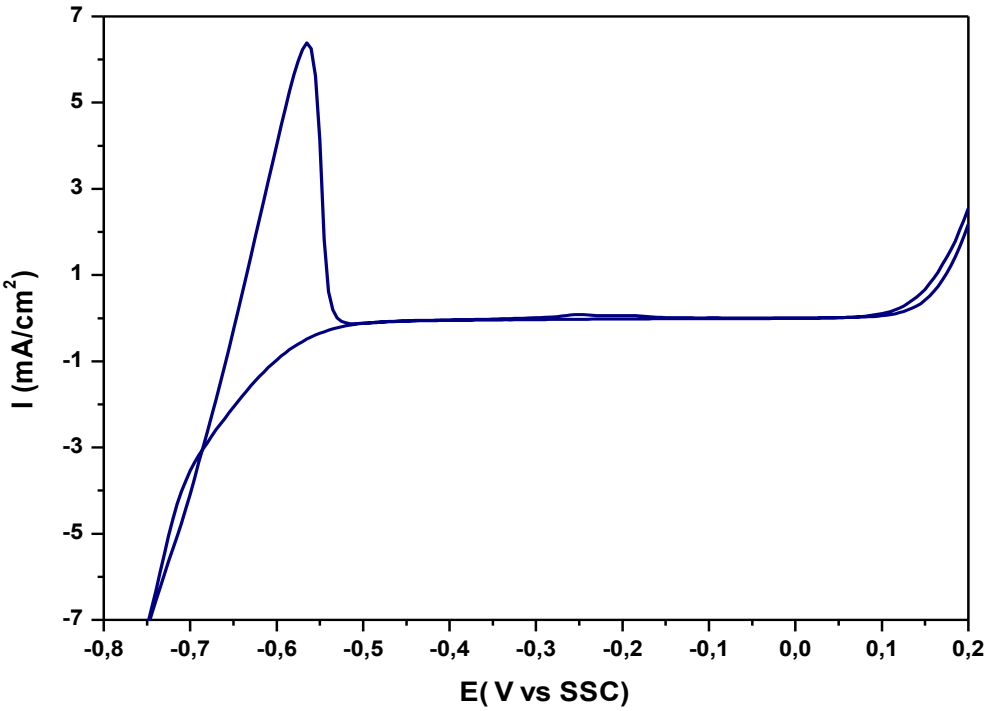

Figure 95: CV for Mo foil in InCl3 12.5mM and NaH2PO2 50mM at 85°C

Characterization was performed also for the phosphorus precursor used in Sahu's works, a solution containing 58.3mM NH_4PF_6 was tested on Mo at room temperature. The resulting plot is shown in *Fig.96*.

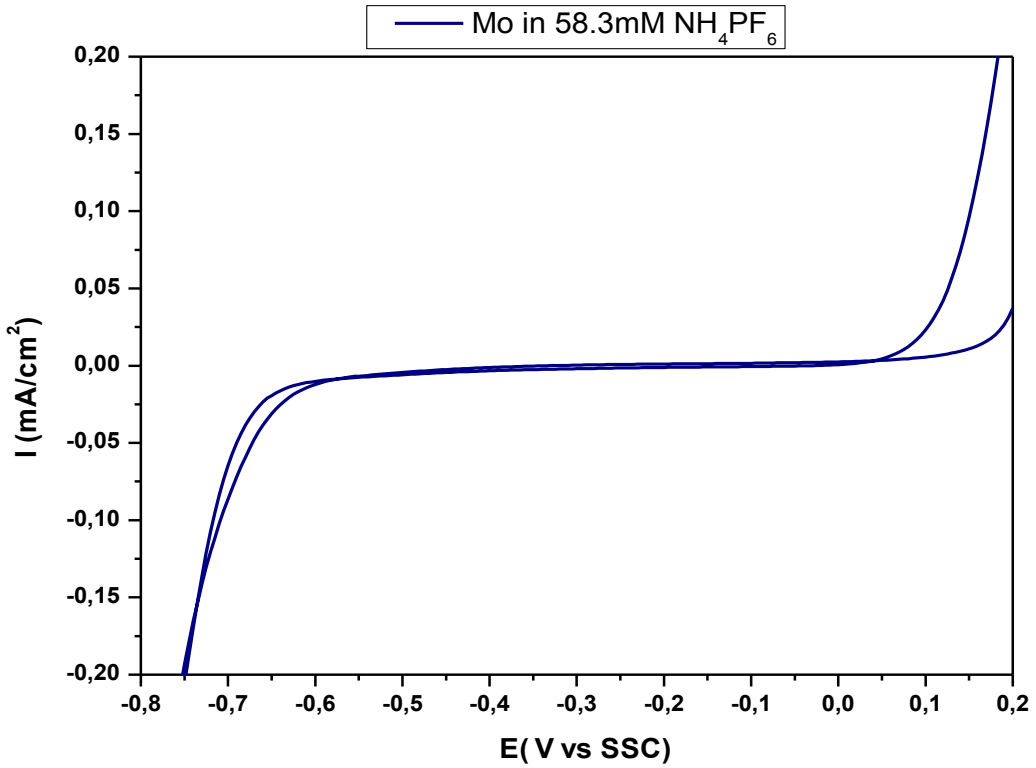

Figure 96: CV for Mo foil in NH4PF6 58.3mM at 85°C

Finally characterization was performed on the solution used for depositions, it was made up of $InCl_3$ 12.5mM and NH_4PF_6 583mM. Test was performed on Mo foil and results are shown in *Fig.97*.

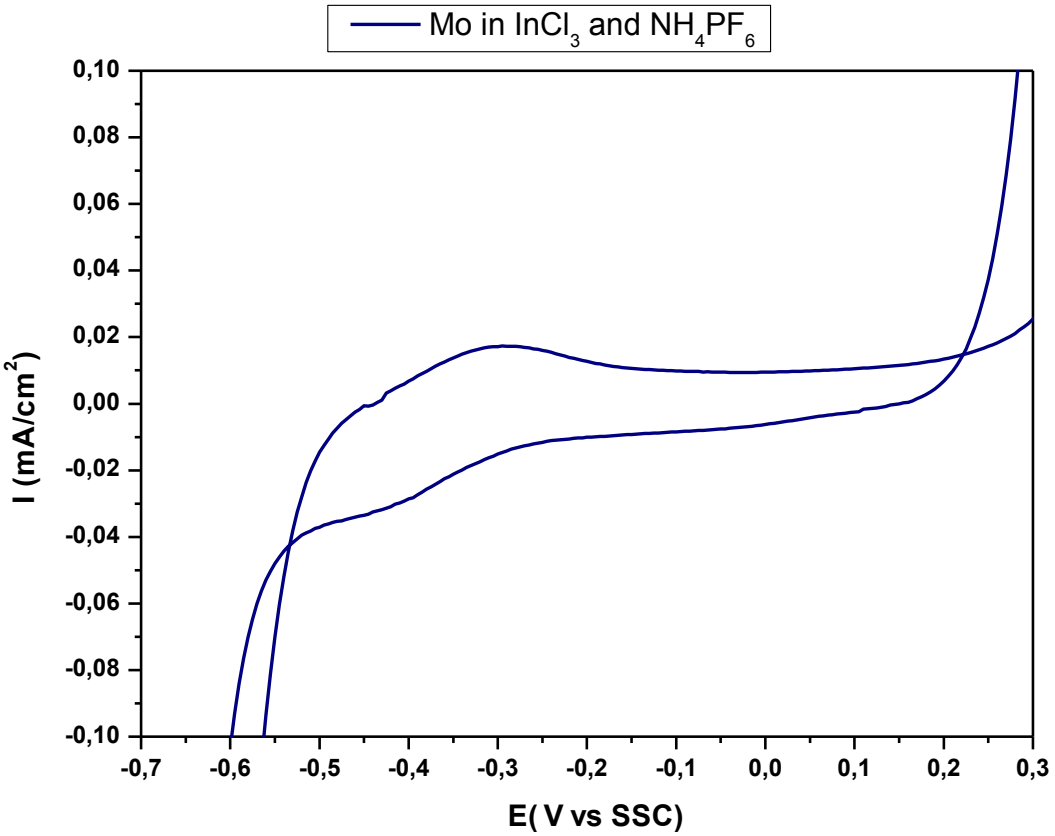

Figure 97: CV for Mo foil in 12.5mM InCl3 NH4PF6 583mM at 85°C

Some tests were performed also on Ni foil to determine the possible influence of the substrate on the activity of the reactants, in particular attention was focused on sodium hypophosphite. A series of CV test was performed with the utilization of KCl as supporting electrolyte and the gradual addition of sodium hypophosphite in the solution, the composition sequence is shown in *Table 3.6.*

Table 3.6

Solution #	**0**	**1**	**2**	**3**	**4**	**5**
KCl (mM)	100	100	100	100	100	100
NaH_2PO_2 (mM)	-	0.62	1.24	3.61	5.88	8.05

Here the superposition of all the measures is plotted, this is shown in *Fig.98*.

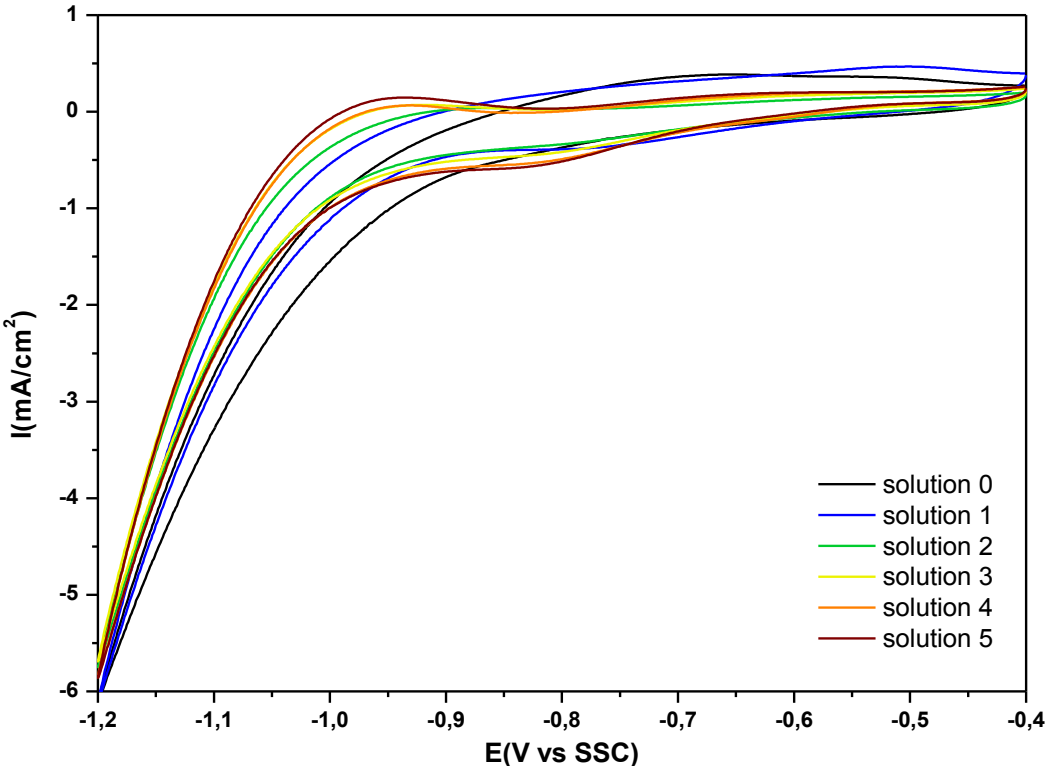

Figure 98: Overlay of CV for Ni foil in KCl with gradual addition of NaH2PO2

In *Fig.99* results are shown for a CV test performed on Ni in a solution containing 100mM NaH_2PO_2.

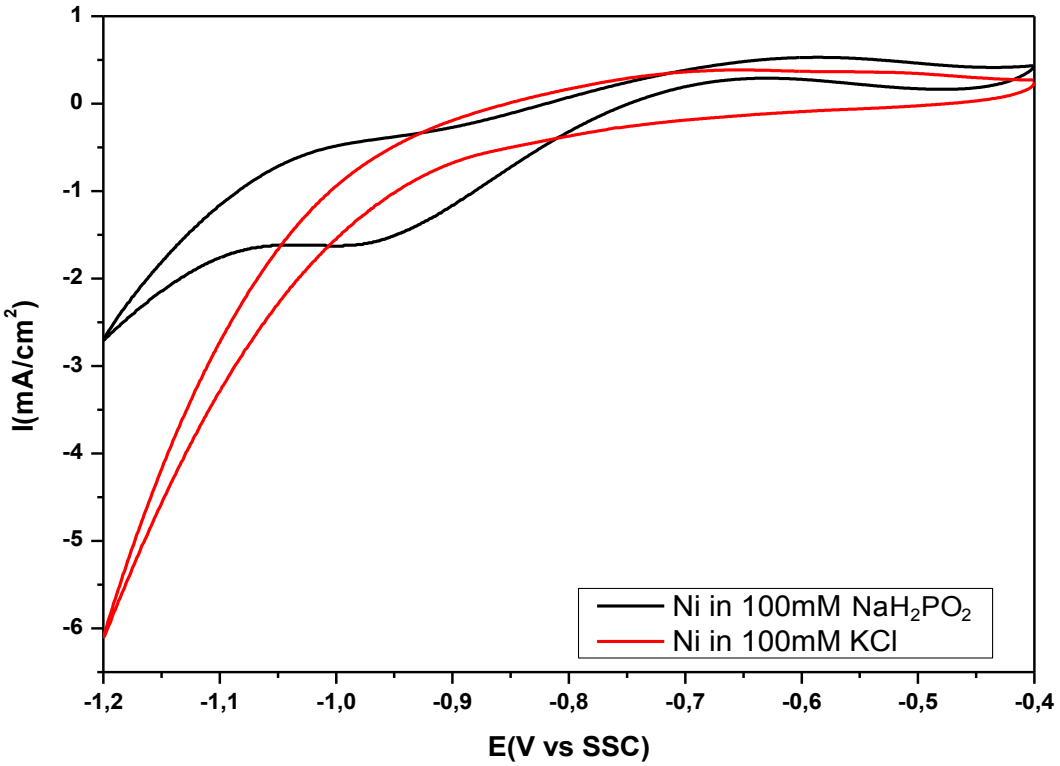

Figure 99: overlay of CV for Ni foil in 100mM KCl and in 100mM NaH2PO2

3.4.2 Pure indium deposition solutions

Testing was performed also on the solution used to deposit pure In layers with the presence of citrates as complexing agents. Testing was performed on commercial Mo foil at room temperature in a solution containing 150mM $InCl_3$, 50mM sodium citrate and 250mM citric acid. Results are shown in *Fig.100.*

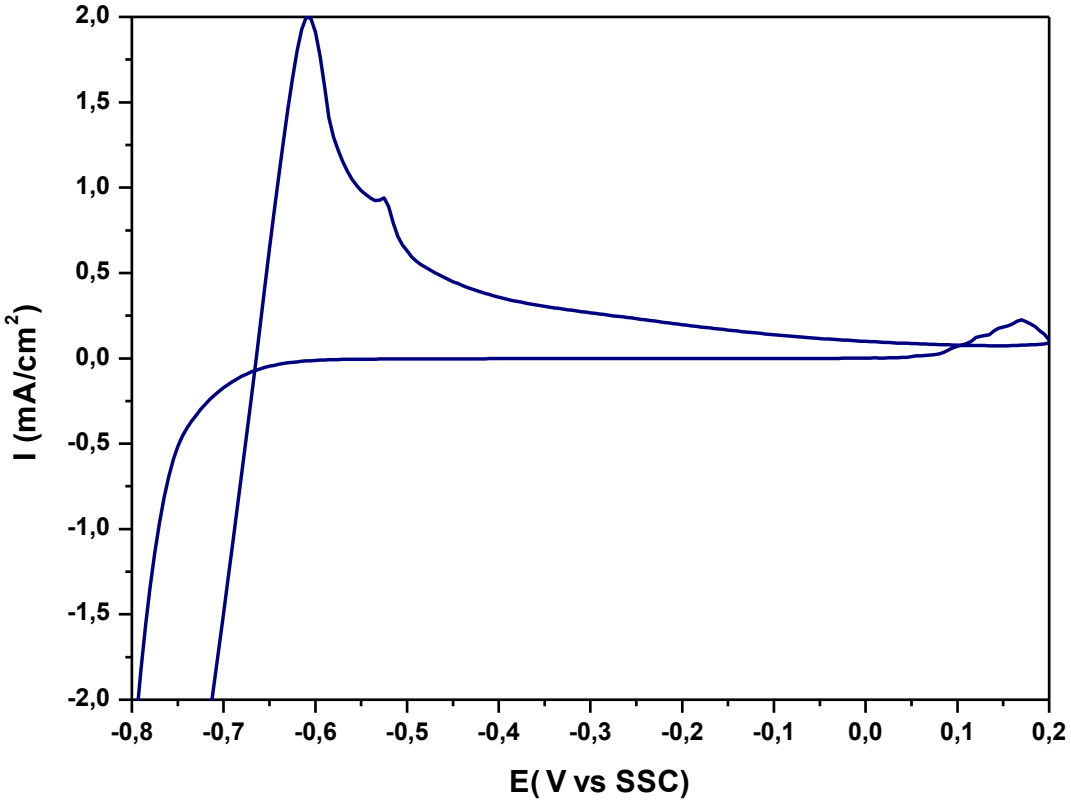

Figure 100: CV for Mo foil in 150mM InCl3 50mM Na citrate and 250mM citric acid

Chapter 4

Discussion

Results were shown in the previous chapter, here discussion is performed. The organization of chapter 3 is maintained also here.

4.1 DIRECT INDIUM PHOSPHIDE CODEPOSITION

Both for direct InP electrodeposition solutions and for pure indium deposition, electrochemical characterization was performed. Below just experimental results on the samples produced are discussed. Results from electrochemical characterization are discussed in a dedicated portion of this chapter.

4.1.1 Deposits based on Ni-P plating

Ni-P is produced both by electrodeposition and electroless deposition using mainly sodium hypophosphite as reducing agent (in electroless depositions) and source of P, sometimes coupled with acids of phosphorus. Fundamental in P codeposition is the interaction between the P precursors and the metal ions in solution. These solutions were considered with the idea that In ions could interact with phosphorus precursors in a similar way to Ni ions.

Considering the results reported in *Fig.32* it's possible to say that deposition conditions used for sample E19 didn't gave positive outcome, since from XRD analysis just In and the Fe signal from the stainless steel substrate were detected.

The sample chosen is just an example among a high number of test performed in different deposition conditions, E19 was chosen as significant for low temperature depositions. In the case of sample E19 the ratio between P precursors and In precursors in solution was equal to 50, other depositions were performed at room temperature ranging this parameter from 0.5 to 200 and varying deposition current from -5 to -30mA/cm^2. Results obtained were the same.

The same considerations can be done for results relative to sample E24, in *Fig.33* it's possible to notice that the XRD spectrum has peaks for In and iron signal from the steel substrate. This sample was reported as significant for tests performed at high temperature (85°C). The most interesting sample in this set of experiments is B9, in this case XRD

(*Fig.*34) spectrum gives signal just for indium, a small peak can be attributed to the Mo substrate. If the EDX analysis is considered (*Fig.35*) it appears clear that In isn't the only species that was deposited during plating of sample B9, signals are present for oxygen and phosphorus, the atomic P to In ratio is 0.8 and oxygen represent 60%at of the deposit. For this reason non fully reduced forms of phosphorus were thought to be deposited, for example phosphates. Elemental mapping was performed to determine the distribution on the sample surface of the different elements. As can be noted in *Fig.36* before annealing elements are not evenly distributed on the surface, oxygen is preferentially coupled with phosphorus while some chloride contamination is present together with indium, the surface looks composed by phosphorus rich and indium rich grains. After annealing oxygen, phosphorus and indium are homogeneously distributed on the sample surface. This is confirmed by XRD analysis presented in *Fig.37*, the spectrum is complex but good match is present for indium phosphate, indium oxide and phosphorus, some peaks could be attributed to InP.

We can thus say that annealing favours diffusion of species present in the deposit (at annealing temperature In is liquid so diffusion is much easier) and interaction between In and the partially oxidized phosphorous species to form $InPO_4$. Some of the oxygen present in the deposits reacts with the In to form oxides, In_2O_3.

These solutions are not a good candidate to directly deposit InP, in particular conditions deposition of In and oxidized phosphorus species is possible, but even with thermal treatments InP cannot be obtained. $InPO_4$ is obtained after annealing but full reduction of phosphorous species wasn't possible. This is confirmed by the PL measure that was performed on sample B9 (*Fig.38*), in fact no peak is present at 920nm that is the wavelength for InP.

4.1.2 Deposits produced with complexing agents

The idea of using complexing agents derived from the negative results obtained in the simpler solutions discussed above. The use of complexants was considered to increase solution stability varying the pH (indium salts are dissolved in water only for pH lower than about 2) but mainly to hinder In deposition and favour phosphorus precursor reactions.

The solutions used are similar to that inspired to Ni-P with the addition of complexing agents. Looking at the results for sample E41 (*Fig.39* and *fig.40*) it's possible to see that this sample was composed by almost pure indium as confirmed by both XRD pattern and

EDX analysis. The same considerations could be done for sample E45 considering its XRD and EDX spectra (*Fig.41* and *fig.42).* Conditions different from that reported in the results were tried for these solutions but didn't gave positive results. Stronger complexing was performed on indium but this didn't led to improvement. In reduction was sometimes completely hindered by complexants, but this didn't led to phosphorus deposition and all the applied current was consumed at the cathode by hydrogen evolution.
Even this class of solution doesn't appear as a possible candidate for InP direct electrodeposition since complexing of indium doesn't favour P reduction that appear to be strictly related to the interaction between its precursors and the metallic species in solution.

4.1.3 Deposits based on Sahu's work

Sahu's papers claiming the possibility of depositing InP directly by electrodeposition were the main reason that led to perform this research on thin film PV devices based on electrodeposited InP.
Depositions in the conditions described as optimal by Sahu in his papers were the first to be performed (experimental setup was discussed in chapter 2) but no successful results were obtained. In the conditions clamed in Sahu's papers no deposits were produced and Ti substrate degradation occurred.
For this reason different conditions were tested, it was believed that precursor concentration in solution was too low, especially $InCl_3$ concentration, and this didn't allowed significant deposition, considering also the possible corrosive effect of fluoride ions deriving from NH_4PF_6 dissolution. Sample A1 was produced increasing of one order of magnitude precursor concentration described by Sahu. In other test also deposition current density was increased to contrast the possible corrosive effect due to the presence of fluorides in solution. Looking at the XRD spectrum (*Fig.43*) it's possible to see two peaks that can be attributed to the deposit, those peaks are small with respect to the background noise and the one at 2θ=26° can be attributed to InP. SEM imaging was performed (*Fig.44*) and can be noticed that the deposit looks composed by a lower layer consisting in flat grains and an upper layer with crystalline dendritic structure. To understand if the nature of the two layer is different mechanical polishing was performed to remove the upper layer. After that, SEM imaging with EDX analysis was performed for the second time, the surface results almost free from the dendritic phase (*Fig.45),* the most important fact is that In:P ratio is nearly unchanged. The presence of F and O signals can be attributed to the substrate, Ti readily oxidizes in the atmosphere and F signal can be

attributed partly to the solution used for deposition and partly to the etching process performed on Ti before deposition with 5% HF, therefore some fluorides can have bound to the Ti surface before and during deposition. These peaks appear after mechanical polishing since the deposited layer is thinner and therefore EDX can "feel" some signal from the substrate.

Given the low deposit quality in terms of morphology and homogeneity PL characterization wasn't performed.

These solutions could give InP deposits but the low quality of the layer obtained doesn't allow the utilization of such films for photovoltaic applications.

4.1.4 Deposits with alcoholic solutions

As the solutions with complexing agents, also these were inspired to Ni-P plating with an addition, alcohols in this case. The idea of this set of experiments is that of stabilizing ionic indium hydroxides in solution. It is believed that a key step for P codeposition with Ni, starting from sodium hypophosphite, is the interaction between hypophosphite and nickel hydroxide ions [42]. Thus the interaction between In and Na hypophosphite could be favoured if $In(OH)^{n+}$ is present in solution instead of the hydrate ion.

Deposition revealed to be more complex than in aqueous solutions both for the different nature of the solvent and for the higher viscosity of the solution, especially when high amounts of alcohol were used.

Both for sample B76 and B80 the same considerations can be done, the XRD spectra respectively *Fig.47* and *Fig.49* show that the deposit consists in indium, this is confirmed also by EDX performed on sample B76 (*Fig.48*) that shows the complete absence of P in the deposit.

Also these solutions don't look a good candidate for direct InP electrodeposition. The stabilization of the $In(OH)^{n+}$ ions, that, according to the Pourbaix diagram should occur in the pH range used for these test, doesn't favour interactions between indium and sodium hypophosphite that could led to P codeposition.

4.2 INDIUM AND RED PHOSPHORUS COMPOSITE DEPOSITION

This set of depositions was inspired to some papers relative to Cu and red phosphorus powder composite deposition [44][43]. Since difficulties were met in direct electrodeposition of InP, this alternative allowed to deposit a composite, using solutions of indium salts with suspension of red phosphorus powder. With this process just In is

electrodeposited and P is included in the form of particles. Subsequently thermal treatments can allow interaction inside the composite to form InP.

Sample B72 was produced with the one-step deposition process, looking at the XRD spectrum in *Fig.50* it's possible to notice that the red P doesn't give any signal and then the spectrum has peaks just for indium. Sample B72 was then divided in four equivalent pieces that underwent different thermal treatments. Looking at the EDX spectra in *Fig.51* and following it's possible to notice that the amount of phosphorus incorporated is low with In:P ratios going from 4 to 10 before thermal treatments. Situation is unchanged for sample B72a and B72c after RTA, the In:P ratio is maintained but still too low. For sample B72d the situation is different, no P signal is present after annealing in the CVD chamber (*Fig.55*). This difference can be related to the longer times used for annealing in the CVD chamber that may have caused P sublimation. The SiO_2 cap was introduced to avoid P oxidation and sublimation at high temperature and to hinder In flow in the molten state during annealing at temperatures higher than its melting point. In some cases though, as for sample B72d, the SiO_2 cap wasn't able to avoid P losses during annealing. This is due in part to the permeability of silicon dioxide to P vapours, in part to the long annealing times used for this sample and in part to the high roughness of composite samples. The high roughness in fact doesn't allow the formation of a continuous and defectless layer of silicon dioxide.

Since the one-step deposition of the In-P_{red} composite showed some problems due to the insulating nature of phosphorus, also two-step deposition was performed in parallel. The presence of a thin seed layer of In makes composite deposition easier reducing deposition voltage. An example of sample produced in this way is B90, the XRD spectrum before annealing (*Fig.*56) shows peaks just for indium as happened for B72. This sample was then divided into two pieces and both underwent CSS annealing.

In sample B90b both upper and lower plate of the CSS chamber were heated, probably these conditions were too aggressive and led to sample degradation with the formation of In_2O_3, as shown in the XDR spectrum, *Fig.57.* Some phosphorous is still present in the deposit, due to the very short times involved in the process, but it's clear from *Fig.59* that the thermal treatment caused $Si0_2$ cap to flake off the substrate in some points leaving the composite exposed.

Annealing conditions for sample B90a involved heating just from the bottom plate were the sample was laying. In these conditions the capping layer wasn't damaged and protected the electrodeposited layer from massive oxidation occurred for sample B90b. *Fig.61* and

Fig.62 show the difference in local composition of sample B90b after annealing: in the first figure a high amount of phosphorus is detected by EDX analysis, but a few microns away the phosphorus content in the deposit is almost nil, as shown in the second EDX spectrum. This implies that during annealing no significant diffusion and interaction between the molten indium and the red phosphorus particles occurred.

Several factors led to abandon this process for production of InP, first of all the theoretical limitation that doesn't allow diffusion of P into the In melt. When considering In phosphorization with phosphine gas, it's believed that formation of an indium melt supersaturated in P is achieved, and consequently nucleation of InP start from this liquid. If we consider the In-P_{red} composite, the supersaturated layer is formed just in close proximity to the phosphorus particle where InP nucleation subsequently occurs. Once a continuous layer of this semiconductor is formed around the particle P diffusion and interaction with the In melt is not allowed leading to inhomogeneities in composition and impossibility of obtaining a sample fully composed of InP.

The second limitation of this process is P_{red} particle dimension available on the market: in principle the diffusion problem cited above could be solved using very fine phosphorus particles, but these are not available on the market. The average diameter of the particles used during deposition was about 100µm and it's not possible to find particles with average diameter below 75µm on the market. This is a problem not just in terms of reaction dynamics, even if such big particles could react to form uniform InP layers, film thickness should be at least equal to particle diameter, i.e. 100µm; a 100µm InP layer is not acceptable since a couple of microns of this material are enough for the proper functioning of the solar cell. The excess thickness would represent useless material and added costs for the final product.

One sample was produced with the three-step process but given the results from the previous structures it wasn't annealed and characterized. In fact for all the structures a lack of P was noticed from EDX analysis, consequently adding a final layer of In would further decrease the P:In ratio.

To conclude the production of InP starting from a In-P_{red} composite doesn't look promising unless some limitations are overcome. The amount of phosphorus powder must be increased in the composite and at the same time smaller particles should be used, this, basing on studies proposed in the aforementioned papers on Cu-P_{red}, would make particle incorporation harder. The P_{red} particle size should be smaller than 1µm both for

dimensional limits of the layer and to allow proper diffusion in the In melt. Particles with this dimension are not available on the market and this would imply *ad hoc* production.

4.3 PURE INDIUM PLATING AND SUBSEQUENT PHOSPHORUS INCORPORATION

As for the experimental results also the discussion is divided into two parts, the one relative to the pure indium plating and the one relative to phosphorus incorporation, this is necessary since studies were performed both on the quality of the final product and on the morphology of the pure indium layer before further treatments.

4.3.1 Pure indium plating

Pure indium deposition assisted both phosphorus incorporation techniques and is the base to obtain good quality final products, at least in terms of morphology. Plating was performed with two different techniques, direct current deposition in the two electrode setup and pulsed current deposition in the three electrode setup. Here results relative to this two processes are discussed individually.

4.3.1.1 DC deposition

The first pure indium samples were produced to assist the phosphorization process performed in Javey's laboratory in UC Berkeley, consequently, the possibility of producing InP from pure indium and successive P_{red} dropcasting, moved more and more our attention on this topic.

The first step to make these deposit suitable both for phosphorization and dropcasting was the production of high purity deposits, the initial samples plated didn't show enough control in impurity concentration and this wasn't acceptable to perform further treatments. The high purity was achieved with a better control both of the glassware and of the chemicals used. High purity (99.99%) chemicals were employed and glassware was cleaned in the order with acetone, IPA, concentrated nitric acid and DI water before utilization.

Samples reported in chapter 3 were already produced in these conditions, once the purity of the deposit was sufficient attention moved to the morphology. Going from sample B58 to B69 passing by sample B60 a marked change in morphology can be noticed (*Fig.63* to

Fig.65), the final target of these depositions was the production of In layers with flat grains.

Through modification of deposition conditions and solution composition it was possible to move from highly crystalline and small grained structure to flatter continuous grains. Sample B60 has flat continuous grains that are at the same time too big. Conditions of sample B69 were used to produce a high amount of sample for phosphorization and P_{red} dropcasting. This is choice was based both on the microstructure, that can be observed in the SEM images, and on the macrostructure that was observed with naked eye. The SEM imaging can't notice the presence of macroscopic flaws or defect in the film, those were mainly related to the low cathodic efficiency of the system. This caused the problematic hydrogen evolution.

The conditions relative to sample B69 were obtained performing studies on the effect of each parameter. Since the solution used consisted just in water and $In_2(SO_4)_3$ the pH could be varied just modifying In precursor concentration, given that hydrogen evolution is favoured by low pH and indium sulphate is acidic, its concentration was decreased from 100mM to 25mM.

At the same time low current density reduces hydrogen evolution but leads to a film composed by individual crystals at small times and too big continuous grains at long times (respectively *Fig.63* and *Fig.64*), higher current density favours the formation of continuous films with smaller grain size thanks to an higher nucleation rate in the first stages of deposition. As can be noted for sample B69 increasing temperature and current density helps in obtaining continuous films controlling the grain size, in fact higher temperature is known to favour hydrogen evolution, but in this case also made hydrogen bubbles smaller and less adherent to the surface reducing pitting problems.

These conditions were chosen since gave the best compromise between the macrostructure, related to hydrogen evolution, and the microstructure, related to nucleation and growth of the In layer.

Once these conditions were set a further improvement in the morphology of the indium layer was necessary. Films produced with indium sulfate solutions had problems of hydrogen evolution even in the conditions chosen as best compromise. Consequently thick layers of indium were necessary to avoid presence of pits reaching the Mo substrate. These films were from one to two order of magnitude thicker than necessary, thus a new solution was ideated to reduce bubbling issues and allow thinner deposits.

Starting from a patent [45], the idea of using citrates as complexing agents for indium was considered. This patent claims the possibility of depositing thin (less than 1μm) layers of indium on copper, with the purity necessary for photovoltaic applications.

The patent claims that a pH=2 is the preferred condition, citrates at this pH are dissociated in a small portion, this causes most of the indium in solution to be present as In^{3+}. Therefore the role of citrates is not properly that of complexing indium, but more that of stabilizing solution pH and reducing hydrogen evolution allowing an higher indium precursor concentration. The patent also proposes that citrates can consume part of the excess protons and also for this reason they can reduce hydrogen evolution.

First trials were performed using the conditions claimed in the patent, as sample B104, but results weren't satisfactory in terms of deposit homogeneity and hydrogen evolution. Most of all pH=2 couldn't be achieved respecting concentration limits proposed in the patent, and addition of acids, as HCl, showed detrimental effects. The composition described in chapter 3 for sample B148 was determined performing calculations of the dissociation constants of all the reactants in solution in order to obtain pH=2 without addition of external acids.

With this solution a high cathodic efficiency could be obtained even for current densities doubled with respect to those used for sample B69. With this solution the H_2 bubbling problem greatly reduced. Pitting problems became thus of secondary importance, another problem was now to be solved. Deposition didn't occur homogeneously on the molybdenum surface and even big portions of the substrate remained exposed at the end of the plating process. This problem wasn't considered before since deposition times were much longer and deposits ticker, thus there was enough time for the substrate to be completely covered.

Molybdenum is defined as a refractory metal, these metals have high melting temperature and generally stable passive oxides on the surface, that protect the metal beneath from oxidation.

The stability of this surface oxide was believed to be the cause of the inhomogeneous indium deposition, thus a more aggressive activation step was performed on the molybdenum substrate. The usual activation procedure described in chapter 2 based on 10% HCl immersion for 5 minutes was gradually modified to be more and more aggressive. The best conditions were found to consist in 20-30min of sonication in concentrated (37%) HCl. Using this activation treatment the deposit homogeneity was increased even for short deposition times.

With these modifications the macro scale morphology was improved even for short deposition times and low thicknesses.

The other parameter to improve was surface roughness, this should be decreased to improve the quality of the final product. Looking at the AFM image taken for sample B104 (*Fig.66*) and considering the roughness resulting from data elaboration, surface morphology is not adequate. Comparison was performed with the morphology relative to In samples produced by evaporation in Javey's lab, known to be suitable for phosphorization with excellent results. Roughness, for a standard indium layer evaporated on Molybdenum foil, was found to be R_a=167nm, R_{ms}=221nm by AFM measure. The target of this section of experimentation is the production of electrodeposited films having roughness as close as possible to this value. Sample B148 gave worse results in terms of roughness with respect to B104 but, as can be seen from the SEM image (*Fig.68*), grains are joined to form a quasi-continuous film, for this reason sample B151 was produced under the same conditions increasing deposition time to 90s. In this way film homogeneity was increased and roughness decreased as can be seen from *Fig.69* and *Fig.70*. The morphology obtained in these conditions is satisfactory even if film thickness is still higher than needed.

The deposition on commercial copper foil was performed for comparison reasons and to verify if the substrate nature plays a role in the film quality. No aggressive activation procedures were performed and film homogeneity was good since the first stages of deposition. Results from AFM measure reveal higher quality in terms of roughness that is comparable with that of the evaporated indium film. At the same time though deposition on copper is not possible since at the high temperature, necessary for thermal treatments, In and Cu can interdiffuse, causing contamination of the indium film.

4.3.1.2 Pulsed current deposition

Pulsed deposition was performed using highly concentrated solutions, together with high current densities this was performed to obtain high nucleation and therefore continuous films composed by fine grains. Despite the high current densities used for these depositions, bubbling was a minor problem thanks to the high indium availability in solution and the short pulse times. Several conditions were tested, continuous or quasi-continuous films were produced but the most promising conditions are the ones used for sample B184 and B188. The deposition conditions for these two samples are the same but plating time was increased from 60s to 90s going from B184 to B188. In fact SEM

imaging on the first sample (*Fig.73*) reveals presence of gaps between the grains leaving the substrate exposed. It's possible to notice in *Fig.75* that the film is more homogeneous and continuous in sample B188 but defects are present due to hydrogen evolution.
Depositions using pulsed current can give better results in terms of morphology but at the same time some deposits showed pits due to formation of small hydrogen bubbles on the surface that didn't detach in the rest time between pulses. The addition of citrates to this solutions could help to reduce hydrogen evolution problems. The effect of this modification was not investigated since pulsed current deposition was just in the initial stages of study, further studies will be performed in the future.

4.3.2 Phosphorus incorporation

As in the previous chapter also here phosphorization and P_{red} dropcasting followed by annealing are discussed separately. Studies on these two incorporation techniques were performed in parallel so the distinction is done to simplify the discussion.

4.3.2.1 Phosphorization

A fundamental passage before performing phosphorization of indium is the deposition of a capping layer of silicon nitride or silicon dioxide onto the electrodeposited film. The capping layer allows to maintain unaltered the morphology of the film after the high temperature process that causes indium to melt. Without the cap, indium in the molten state would ball up to reduce surface energy, because of low wettability of Mo foil.
Phosphorization was performed in the standard conditions used for the evaporated indium films, the first samples to be phosphorized gave good results in terms of composition and PL. The In:P ratio for sample ECD1 after phosphorization results to be almost stoichiometric from EDX analysis (*Fig.76*), formation of InP is confirmed also by PL results, that show peak in the theoretical position for the semiconductor, as can be noticed in the comparison performed in *Fig.77*.
Once composition and PL response were determined, carrier lifetime was measured by TRPL (time resolved photoluminescence). *Fig.78* shows a comparison between the results of the two electrodeposited and phosphorized samples and the high quality evaporated and phosphorized film. It's clear that the samples with the initial indium layer produced by electrodeposition are characterized by a much lower quality. In particular short exciton lifetime are mainly due to presence of contamination and imperfections in the semiconductor film.

B69 was produced using higher purity indium and glassware cleaned with nitric acid to reduce as much as possible the presence of contaminations in the initial In deposit. After capping and phosphorization EDX elemental analysis (*Fig.79)* was performed revealing a slight excess of indium (In:P=55:45), this was confirmed by XRD (*Fig.80)* that reveals presence of unreacted indium in the film. Presence of some residual indium could be due to the high deposit thickness with respect to the layers produced by evaporation. Despite the contamination from the residual indium, TRPL gave excellent results in terms of Exciton lifetime, that revealed to be slightly longer than that relative to the high quality reference sample produced from evaporated indium.

4.3.2.2 Red phosphorus dropcasting

The idea of performing P_{red} dropcasting on pure indium layers is an evolution of the composite deposition with phosphorus particles. Since results from composites were not satisfactory for the reasons cited above, the dropcasting was thought to allow better control both on the indium layer morphology and on the quantity of phosphorus incorporated during thermal treatments.

The different structures were ideated to face problems that manifested in during the production process. One-step dropcasting was immediately understood to be unsuccessful due to the lack of an capping layer necessary to avoid oxidation and viscous flow of indium in the molten state and sublimation of phosphorus.

Two-step dropcasting was used to produce sample B87, XRD analysis (*Fig.82)* reveals presence of both InP and In phases in the sample after phosphorization, this is confirmed by EDX analysis (*Fig.83)* that shows an excess of indium since the deposit results composed of 43%at P and 57%at In. This could be due both to lack of phosphorus, i.e. insufficient quantity of phosphorus dropcasted, and to not adequate annealing conditions.

The same considerations could be done for sample B92, also in this case a strong In signal is present in the XDR spectrum (*Fig.84)*

Due to incomplete reaction of In with red phosphorus powder the PL signal (*Fig.85)* is different from the theoretical one both for sample B87 and for sample B92. This is a signal that the quality of the samples produced is low.

Low quality is confirmed by TRPL results (*Fig.86*), exciton lifetime is indeed low, indicating that the sample has an high quantity of defects and purity is low, in this case In can be considered as an impurity for InP.

Three-step dropcasting was employed to produce sample B106, looking at the XRD results (*Fig.87*) it can be noticed that both InP and In are present in the film after annealing.
To determine sample composition EDX analysis was performed (*Fig.88)* resulting in a lack of phosphorus, incomplete reaction between In and P is observed also in this sample. At higher magnification (*Fig.89)* it is possible to observe that phosphorus reacted with indium to form InP preferentially at the grain boundaries. It is likely that reaction occurred in these zones because of defects in the silicon dioxide layer, that allowed increased phosphorus diffusion in the In layer.
The double silicon dioxide layer allows to increase remarkably In confinement avoiding flow of molten indium, but at the same time it limits phosphorus diffusion reducing InP formation. Further investigation should be performed for example decreasing the thickness of the SiO_2 layer dividing In and the dropcasted phosphorus in order to favour P diffusion.
This process looks promising to synthesise InP given that the correct annealing conditions are determined as well as the proper thickness for each of the capping layers is established. If the proper condition are found to obtain InP, dropcasting could be replaced by spin coating in order to reach an higher degree of dimensional control and homogeneity in the phosphorus layer.

4.4 ELECTROCHEMICAL CHARACTERIZATION

Electrochemical characterization was performed in parallel with electrodeposition experiments. Each group of solutions was studied by CV to determine the reactivity of the species used as precursors, or the effect of complexing agents on the reactivity of precursors themselves.
Here CV is discussed separately for clarity of discussion, but should be kept in mind that these studies were performed at the same time of plating experiments, moreover just some of the test performed were reported in chapter 3 and discussed here.
Electrochemical characterization wasn't the main focus of this research project and was performed as a consequence of difficulties met in obtaining InP, therefore results presented should be considered as preliminar and further studies should be performed to achieve an higher understanding of the phenomena.

4.4.1 Direct InP deposition solutions

The first solutions to be characterized were those inspired to Ni-P plating. CV was performed both on single reagents and on combinations of them, in *Fig.90* and *Fig.91* it's

possible to notice the similarity in the behaviour of phosphorous and phosphoric acid on Mo foil. Both the anodic oxidation peak (E_a=-0.2V vs SSC) and the cathodic reduction peak (E_c=-0.3/-3.5V vs SSC) are at similar values. The similarity in behaviour could be due to the fast oxidation of phosphorus acid to phosphoric acid in water, consequently the electrochemical behaviour of the two solution is similar since the solutions contain the same species. The peaks could be attributed to Mo itself, right after immersion in phosphoric/phosphorous acid Mo can dissolve forming Mo^{3+} ions in solution. The cathodic peak could be therefore attributed to reduction of these ions to metallic molybdenum and anodic peak to oxidation of metallic Mo to give trivalent ions.

Fig.92 reports CV test performed on a solution containing 100mM sodium hypophosphite using a Mo foil working electrode, scan rate was 10mV/s. It's possible to notice how this reagent doesn't show any activity in the stability window of water, no peaks are indeed present in the cyclic curve.

Fig.93 shows the cyclic polarization curve performed on Mo in a solution containing $InCl_3$ 100mM. It's possible to notice a marked anodic oxidation peak relative to In dissolution at E_a=-0.55V vs SSC, while the cathodic reduction peak is much less evident. It's likely that In reduction occurs even during hydrogen evolution since, after just one cycle, In was present on the Mo surface in the form of film.

In *Fig.94* and *Fig.95* CV test are reported for a solution containing both indium chloride and sodium hypophosphite on Mo. In this case hypophosphite seems to interact with In, in fact if comparing the CV performed either in pure indium chloride or in pure sodium hypophosphite, it's possible to notice that the anodic oxidation peak is shifted to less negative values with respect to *Fig.93*. Formation of compounds between indium and hypophosphite could be the reason for the modification in the electrochemical behaviour of the solution.

As occurred for sodium hypophosphite also ammonium hexafluorophosphate doesn't show any activity on Mo foil, this is confirmed by the CV test reported in *Fig.96.* At the same time with addition of indium chloride to the solution, *Fig.97*, a CV similar to that reported in *Fig.94* is obtained. This could confirm the possibility of interaction between indium and phosphorus precursors.

In *Fig.98* and *Fig.99* CV tests are shown for sodium hypophosphite on Ni foil. It's possible to notice in *Fig.98* that, increasing the hypophosphite concentration, the curve changes with modification of the knee at -0.95V vs SSC. This modification is gradual and increases increasing Na hypophosphite concentration. The shape of the black curve in *Fig.99*

confirms that Na hypophosphite shows some activity if compared to the red curve, relative to the supporting electrolyte (KCl), or to the curve relative to the same measure performed on Mo foil, *Fig.92*. The electrochemical process associated to this measure is not fully understood and doesn't bring to P reduction on the Ni surface. Ni foil was indeed analysed with XPS but no signal for P compounds was found. Therefore since the modification of the curve increases with concentration, the process involved could be adsorption/desorption of hypophosphite ions on the surface that doesn't consequently lead to P reduction. The mechanism of hypophosphite interaction with Ni and adsorption on the metallic surface was proposed by Cavallotti and Djoki [42]. A difference should be pointed out between the behaviour of Mo and Ni with sodium hypophosphite: while on Ni CV test shows activity of hypophosphite, probably due to adsorption on the metallic surface, on Mo hypophosphite is active only if present together with indium ions. Therefore it could be proposed that some interaction occurs between In and hypophosphite ions as it occurs between Ni and hypophosphite ions, but this interaction is not sufficient to lead to reduction of phosphorus on the electrode surface.

4.4.2 Pure indium deposition solutions

Results from electrochemical characterization for solutions devoted to pure indium deposition, are reported just relative to solutions containing citrates. CV test for the other solution used, containing just indium sulphate, is equivalent to that of $InCl_3$ shown in *Fig.93.* Looking at *Fig.100* instead it's possible to notice the presence of a double anodic oxidation peak, the reduction peak is also in this case "hidden" in the hydrogen evolution region. The presence of a double peak could confirm that citrates at the pH used for deposition are not fully dissociated, thus In is not completely complexed. If this is the case one peak could be relative to the oxidation of In to In^{3+} and the other could be related to complexed forms of indium.

Conclusions

The work performed represents the initial stage of a longer and articulated research program, sponsored by US government, on InP for thin film solar cells. Despite that, some consideration could be done on the results obtained in the first year of research.

First of all it's necessary to remember that In is a rare metal but more and more studies have been performed on the recovery of In from ITO used as transparent conductor layer in LCD panels. High recovery efficiencies, almost reaching 90%, have been achieved using relatively simple processes as described in several papers [1][2][3][4].

Results on direct InP electrodeposition are not encouraging, solutions claimed in Sahu's works are maybe suitable for electrodeposition of InP but the quality is low and for sure not high enough for photovoltaic applications. Solutions inspired to Ni-P resulted, in determined condition, in incorporation of P in the electrodeposited layer. The incorporated P though resulted not fully reduced and, after thermal annealing, it was only possible to obtain $InPO_4$ and not InP.

Results deriving from solutions with the addition of complexing agents or alcohols are not different. It is then possible to conclude that direct electrodeposition of InP from aqueous solutions is not possible, at least for the system studied in this work.

Some organic P precursors could be used given their much higher reactivity, that alternative would also imply more complex and safety concerning production processes.

Difficulty met in the direct electrodeposition process is one of the reasons that caused the study to move on In electrodeposition and successive phosphorus incorporation.

The first step in this direction was In-P_{red} composite plating: inspired by some papers on Cu-P_{red} composite deposition, this process seemed a good alternative to overcome the problem of P codeposition from the reduction of species in solution. Using a suspension of P_{red} powder in fact phosphorus can be incorporated, in its reduced form, simply because the powder is entrapped in the growing In layer. Then chemical interaction with indium is favoured by thermal treatments. In principle this process is promising but technological and theoretical limitations cause this process to be not adequate for production of good quality InP. The first limitation is the nature of interaction between In and P to form InP, the semiconductor nucleates from the In melt supersaturated with P. When considering annealing of the In-P_{red} composite, the supersaturated melt is formed in close proximity to

the P particles and therefore InP nucleates forming a barrier that avoids further P diffusion into the surrounding In. This causes incomplete reaction of In and P_{red} to form InP. In principle this theoretical limitation could be overcome using very fine (less than one micron in diameter) phosphorus particles, this leads to the other limitation of this process: particle dimension available on the market.

The finest particles found on the market had a 75µm average diameter, the one used during research had a 100µm average diameter. The big particle dimension is a problem both for the In-P interaction involved in the InP nucleation process and for the thickness of the final product. A couple of microns of InP are in fact sufficient to absorb 99% of the solar radiation that the bulk material would absorb. The use of particles having 100µm average diameter leads to the production of layers that in the best of the hypothesis are just some microns thicker than 100µm. This implies the presence of about 100µm of material that are actually useless.

It comes clear that this production route is not a good candidate, unless red phosphorus particles at least in the hundreds of nanometre range are employed. This would lead to other issues as stability of nanoparticles in suspension and control over the quantity of phosphorus incorporated in the film.

Limitations met in composite deposition process led to focus attention on another pathway to obtain InP, i.e. dropcasting of red phosphorus suspensions on pure In layers produced by electrodeposition, followed by annealing. The evolution of the three architectures led to improvements but also complications. Progressive introduction of silicon dioxide capping layers increases indium confinement in the molten state, allowing a high degree of conservation of the original microstructure, and avoids degradation phenomena, but at the same time reduces In-P interactions.

Since SiO_2, or an equivalent capping layer, is necessary to achieve good results in terms of morphology and homogeneity, more studies should be performed on this topic in order to allow complete reaction between the electrodeposited In and the dropcasted P layer and obtain InP, after phosphorization.

This process looks promising, given that the proper capping layer and the proper annealing conditions are found. Also dropcasting could be replaced by spin coating in order to achieve an higher control and an higher reproducibility in the formation of the P_{red} layer.

Phosphorization is the process that gave better results in terms of optical/semiconducting properties, but at the same time is the one that implies the minor innovation. This process is already used to phosphorize In layers obtained by evaporation. The only advantage

deriving from this study is the possibility of using electrodeposited In instead of evaporated In, with a slight reduction in process complexity and costs.

Finally studies performed on pure indium showed possibility of obtaining good quality indium layers in terms of morphology that could be compared, for determined deposition conditions, to that of evaporated indium. The utilization of solutions with citrates allowed to increase deposit quality even if Mo doesn't look the best substrate for electrodeposition of In both because of stable passive oxides on its surface and because the commercial foil used during experiments presented poor surface quality with evident marks deriving from the rolling process. This texture on Mo surface influenced nucleation of indium altering homogeneity in nuclei distribution on the surface.

From electrochemical studies Mo doesn't look to favour activity of sodium hypophosphite. Ni shows some activity but, at the same time depositions done on Ni didn't show any difference from that performed on Mo.

Bibliography

[1] K.-S. Park, W. Sato, G. Grause, T. Kameda, and T. Yoshioka, "Recovery of indium from In2O3 and liquid crystal display powder via a chloride volatilization process using polyvinyl chloride," *Thermochimica Acta*, vol. 493, no. 1–2, pp. 105–108, Sep. 2009.

[2] K. Takahashi, A. Sasaki, G. Dodbiba, J. Sadaki, N. Sato, and T. Fujita, "Recovering Indium from the Liquid Crystal Display of Discarded Cellular Phones by Means of Chloride-Induced Vaporization at Relatively Low Temperature," *Metallurgical and Materials Transactions A*, vol. 40, no. 4, pp. 891–900, Feb. 2009.

[3] C.-H. Lee, M.-K. Jeong, M. Fatih Kilicaslan, J.-H. Lee, H.-S. Hong, and S.-J. Hong, "Recovery of indium from used LCD panel by a time efficient and environmentally sound method assisted HEBM.," *Waste management (New York, N.Y.)*, vol. 33, no. 3, pp. 730–4, Mar. 2013.

[4] J. Li, S. Gao, H. Duan, and L. Liu, "Recovery of valuable materials from waste liquid crystal display panel.," *Waste management (New York, N.Y.)*, vol. 29, no. 7, pp. 2033–9, Jul. 2009.

[5] G. Kopp and J. L. Lean, "A new, lower value of total solar irradiance: Evidence and climate significance," *Geophysical Research Letters*, vol. 38, no. 1, p. L01706, Jan. 2011.

[6] BP, "BP Statistical Review of World Energy June 2012," 2012.

[7] M. Masi and S. Carrà, "Il ruolo del solare nel futuro panorama energetico," 2007.

[8] D. M. Chapin, C. S. Fuller, and G. L. Pearson, "A New Silicon p-n Junction Photocell for Converting Solar Radiation into Electrical Power," *Journal of Applied Physics*, vol. 25, no. 5, p. 676, 1954.

[9] C. Kittel, *Introduction To Solid State Physics - 7Th Edition*. John Wiley & Sons, Inc., 1996.

[10] Y. Revi, "Photovoltaic Effect in p-n Junctions," *Physical Review*, vol. 95, 1954.

[11] A. Slaoui and R. T. Collins, "Photovoltaics : Advanced Inorganic Materials," *Encyclopedia of Materials: Scienece and Technology*. 2008.

[12] R. W. Miles, K. M. Hynes, and I. Forbes, "Photovoltaic solar cells: An overview of state-of-the-art cell development and environmental issues," *Progress in Crystal Growth and Characterization of Materials*, vol. 51, no. 1–3, pp. 1–42, Jan. 2005.

[13] W. Shockley and H. J. Queisser, "Detailed Balance Limit of Efficiency of p-n Junction Solar Cells," *Journal of Applied Physics*, vol. 32, no. 3, p. 510, 1961.

[14] L. L. Kazmerski, “Solar photovoltaics R&D at the tipping point: A 2005 technology overview,” *Journal of Electron Spectroscopy and Related Phenomena*, vol. 150, no. 2–3, pp. 105–135, Feb. 2006.

[15] C. R. Wronski and D. E. Carlson, *Clean Electricity from Photovoltaics*. London: Imperial College Press, 2001, pp. 199–236.

[16] T. Mishima, M. Taguchi, H. Sakata, and E. Maruyama, “Development status of high-efficiency HIT solar cells,” *Solar Energy Materials and Solar Cells*, vol. 95, no. 1, pp. 18–21, Jan. 2011.

[17] I.Weinberg, C. K. Swartz, and R. E. J. Hart, “Proceedings of the 18th IEEE Photovoltaics Specialists Conference,” 1985, pp. 5344–5349.

[18] Y. Ohmachi, T. Oh, Y. Kadota, and S. Matsuda, “GaAs-on-Si solar cells for space use,” 2000, pp. 1012–1015.

[19] R. Tatavarti, G. Hillier, A. Dzankovic, G. Martin, F. Tuminello, R. Navaratnarajah, G. Du, D. P. Vu, and N. Pan, “Lightweight, low cost GaAs Solar Cells on 4'' epitaxial liftoff (ELO) wafers,” 2008, pp. 1–4.

[20] K. Lee, J. D. Zimmerman, Y. Zhang, and S. R. Forrest, “Epitaxial lift-off of GaAs thin-film solar cells followed by substrate reuse,” 2011, pp. 1698–1700.

[21] M. Tseng, R. Horng, Y. Tsai, D. Wuu, and H. Yu, “Fabrication and Characterization of GaAs Solar Cells on Copper Substrates,” *IEEE Electron Device Letters*, vol. 30, no. 9, pp. 940–942, Sep. 2009.

[22] A. Yamamoto, M. Yamaguchi, and C. Uemura, “High conversion efficiency and high radiation resistance InP homojunction solar cells,” *Applied Physics Letters*, vol. 44, no. 6, p. 611, 1984.

[23] A. Yamamoto, M. Yamaguchi, and C. Uemura, “High efficiency homojunction InP solar cells,” *Applied Physics Letters*, vol. 47, no. 9, p. 975, 1985.

[24] M. Sugo, A. Yamamoto, and M. Yamaguchi, “n+ p p + Structure InP Solar Cells Grown by Organometallic Vapor-phase Epitaxy,” *IEEE transaction on electronic devices*, vol. 34, no. 4, pp. 772–777, 1987.

[25] R. Hoffman, D. A. Scheiman, S. A. Ringel, W. Davis, V. G. Weizer, D. M. Wilt, and D. J. Brinker, “Development of High Efficiency p+/n InP Solar Cells for Hetero-epitaxial Applications,” 1996, pp. 171–174.

[26] M. K. Lee, D. S. Wuu, and R. H. Horng, “p+/n/n+ InP solar cells directly on Si substrates,” *Applied Physics Letters*, vol. 62, no. 10, p. 1140, 1993.

[27] K.-T. Shiu, J. Zimmerman, H. Wang, and S. R. Forrest, “Ultrathin film, high specific power InP solar cells on flexible plastic substrates,” *Applied Physics Letters*, vol. 95, no. 22, p. 223503, 2009.

[28] K. Lee, K.-T. Shiu, J. D. Zimmerman, C. K. Renshaw, and S. R. Forrest, "Multiple growths of epitaxial lift-off solar cells from a single InP substrate," *Applied Physics Letters*, vol. 97, no. 10, p. 101107, 2010.

[29] M. Zheng, Z. Yu, T. Joon Seok, Y.-Z. Chen, R. Kapadia, K. Takei, S. Aloni, J. W. Ager, M. Wu, Y.-L. Chueh, and A. Javey, "High optical quality polycrystalline indium phosphide grown on metal substrates by metalorganic chemical vapor deposition," *Journal of Applied Physics*, vol. 111, no. 12, p. 123112, 2012.

[30] J. J. Cuomo and R. J. Gambino, "The Synthesis and Epitaxial Growth of GaP by Fused Salt Electrolysis," *journal of electochemical society*, vol. 115, no. 7, pp. 755–759, 1968.

[31] D. Elwell, R. S. Feigelson, and M. M. Simkins, "Electrodeposition of indium phosphide," *Journal of Crystal Growth*, vol. 51, no. 2, pp. 171–177, 1981.

[32] S. N. Sahu, "Aqueous electrodeposition of InP semiconductor films," *Journal of Materials Science Letters*, vol. 8, no. 5, pp. 533–534, May 1989.

[33] S. N. Sahu, "structural optical and electrical properties of first aqueous electrodeposited InP semiconductor films," *Solar Energy Materials*, vol. 20, no. 5–6, pp. 349–358, 1990.

[34] S. N. Sahu, "Some properties of the first non-aqueous electro-codeposited InP , In and P thin films," *Journal of Materials Science: Materials in Electronics*, vol. 3, pp. 102–106, 1992.

[35] J. M. Olsen, S. R. Kurtz, and A. E. Kibbler, "Proceedings of the 20th IEEE Photovoltaics Specialists Conference," 1988, p. 777.

[36] Y. D. Gamburg and G. Zangari, *Theory and Practice of Metal Electrodeposition*. Springer, 2011.

[37] W. Simka, D. Puszczyk, and G. Nawrat, "Electrodeposition of metals from non-aqueous solutions," *Electrochimica Acta*, vol. 54, no. 23, pp. 5307–5319, Sep. 2009.

[38] F. Endres, "Ionic liquids: solvents for the electrodeposition of metals and semiconductors.," *Chemphyschem : a European journal of chemical physics and physical chemistry*, vol. 3, no. 2, pp. 145–54, Feb. 2002.

[39] L. M. Abrantesa and J. P. Correiab, "On the Mechanism of Electroless Ni- P Plating," *journal of electochemical society*, vol. 141, no. 9, pp. 2356–2360, 1994.

[40] P. Peeters, G. v. d. Hoorn, T. Daenen, a. Kurowski, and G. Staikov, "Properties of electroless and electroplated Ni–P and its application in microgalvanics," *Electrochimica Acta*, vol. 47, no. 1–2, pp. 161–169, Sep. 2001.

[41] J. L. Carbajal, "Electrochemical Production and Corrosion Testing of Amorphous Ni-P," *Journal of The Electrochemical Society*, vol. 135, no. 12, p. 2952, 1988.

[42] S. S. Djoki and P. L. Cavallotti, *Electrodeposition*, vol. 48. New York, NY: Springer New York, 2010, pp. 251–289.

[43] D. W. Kirk, "The Electrolytic Codeposition of Copper and Phosphorus," *Journal of The Electrochemical Society*, vol. 136, no. 11, p. 3545, 1989.

[44] J. W. Graydon, "Suspension Electrodeposition of Phosphorus and Copper," *Journal of The Electrochemical Society*, vol. 137, no. 7, p. 2061, 1990.

[45] W. Jiaxiong, A. Serdar, and B. M. Basol, "Indium Electroplating Baths for Thin Layer Deposition," 2009.

[46] W. K. Metzger, R. K. Ahrenkiel, P. Dippo, J. Geisz, M. W. Wanlass, and S. Kurtz, "Time-Resolved Photoluminescence and Photovoltaics," no. January, 2005.